Electrochemical Kinetics of Thin Film Vanadium Pentoxide Cathodes for Lithium Batteries

by

Simon C. Mui

S.M. Technology & Policy
Massachusetts of Institute of Technology, 2002

B.S. Materials Science & Engineering
B.S. Peace & Conflict Studies
University of California, Berkeley, 1999

Submitted To The Department of Materials Science & Engineering
In Partial Fulfillment of the Requirements for the Degree of

Doctor of Philosophy in Materials Science & Engineering
at the
Massachusetts Institute of Technology

September, 2005

© 2005 Massachusetts Institute of Technology.
All rights reserved.

Signature of Author: _____
Department of Materials Science & Engineering
July 14, 2005

Certified by: _____
Donald R. Sadoway
John F. Elliott Professor of Materials Chemistry
Thesis Supervisor

Accepted by: _____
Gerbrand Ceder
R. P. Simmons Professor of Materials Science and Engineering
Chair, Departmental Committee on Graduate Students

MASSACHUSETTS INSTITUTE OF TECHNOLOGY
SEP 2 9 2005
LIBRARIES

ARCHIVES

Electrochemical Kinetics of Thin Film Vanadium Pentoxide Cathodes for Lithium Batteries

by

Simon C. Mui

Submitted to the Department of Materials Science & Engineering
on July 14, 2005 in Partial Fulfillment of the
Requirements for the Degree of Doctor of Philosophy in
Materials Science & Engineering

ABSTRACT

Electrochemical experiments were performed to investigate the processing-property-performance relations of thin film vanadium pentoxide cathodes used in lithium batteries. Variations in microstructures were achieved via sputtering and anneal treatments, resulting in films with different morphologies, grain size distributions, and orientations. Key findings included (1) grain size distributions largely did not affect the current rate performance of the cathodes. Rather, the film orientation and the ability to undergo rapid phase transformation were more vital to improving performance; (2) interfacial resistance and ohmic polarization were also dominant at the high current rates used (> 600 $\mu A/cm^2$) in addition to solid diffusion; and (3) optimization of thin film batteries requires that film thickness be < 500 nm to avoid diminishing returns in power and energy densities. Kinetic parameters including the transfer coefficient ($\alpha = 0.90 \pm 0.05$) and standard rate constant ($k^0 \sim 2 \times 10^{-6}$ cm/s) for vanadium pentoxide films were quantified using slow scan DC cyclic voltammetry and AC cyclic voltammetry. The reaction rate was found to be potentially limiting at moderate to high current rates (> 200 $\mu A/cm^2$). An analysis of the wide variation in current-rate performance for different V_2O_5 architectures (including composite, nanofiber, and thin film) shows a convergence in results when the area of active material has been factored into the metric. This convergence suggests that either the reaction rate or interfacial resistance is limiting in V_2O_5 as opposed to diffusion.

Thesis Supervisor: Donald R. Sadoway
Title: John F. Elliott Professor of Materials Chemistry

Table of Contents

List of Figures

List of Tables

Acknowledgments

A little learning is a dangerous thing; Drink deep, or taste not the Pierian spring.
Alexander Pope (1688-1744)

It's always wise to raise questions about the most obvious and simple assumptions.
C. West Churchman (1913-2004)

First and foremost, I would like to acknowledge my mentor, West Churchman. Sadly, he passed away at the ripe old age of 90 last year in Bolinas, California. I spent many of my formidable years at U.C. Berkeley as his student. If anyone has contributed most to my ability to lead an ethical path in life and to think in terms of a systems approach, it has been West. I will always cherish our friendship over the years.

My development as a researcher would not have been possible without the guidance of Professor Sadoway. I have always appreciated his efforts to tackle problems with tremendous environmental import and to conduct research that is both purposeful and unique. He has encouraged and entrusted me to think independently in my research. Most important, he has allowed me freedom to make mistakes without penalty. I have grown tremendously through this process, and I thank him for his support.

To friends and fellow group members: I could not have made it to this point without the laughter, the mutual support, and the fun extracurricular activities along the way. Their help in the lab and outside has made my experience that much better. I will always value the friendships I have made over the years. My doors and schedule will always be open for them.

To my family and particularly to my wife: I know it has been a roller-coaster ride at times, but this journey has now born fruit. The support from family can be humbling, and the bonds are often stronger than we scientists can explain. I know I am a better person for their support and sacrifices. Thank you for all the love you have shown.

Chapter 1: Introduction

The dual need to meet growing energy demands while mitigating environmental damage will require innovations in such diverse areas as energy generation and storage, transportation and mobility, and remote sensing. Portable power sources may serve as critical enabling technologies in these key areas affecting sustainability.* In particular, electrochemical energy storage devices may allow for further advances to be made in distributed energy generation and storage, hybrid electric vehicles, and in embedded environmental sensors and computing technologies incorporating microelectromechanical (MEMS) systems.†

Efforts to integrate and commercialize portable power systems face several hurdles however, including the need for:

- Greater power and energy densities
- smaller sizes and lower weights
- lower-cost and easier production
- greater reliability and safety
- long life and reuse, recyclability, and little or no maintenance.

Some of these technologies are compared in Figure 1 which compares the energy and power density for different categories of devices. It is observed that both fuel cells and batteries have among the highest energy densities.

---

* See Clay Christenson's *The Innovator's Dilemma: When New Technologies Cause Great Firms to Fail*, Harvard Business School Press, (1997) for a discussion of disruptive and enabling technologies. Also see http://www.cymbet.com/about.php for a start-up's view on the future of thin film batteries.

† These are among a few of the technical goals proposed by the federal government. See for instance, Advanced Technology Program, National Institute of Standards and Technology, "ATP Focused Program: Premium Power: Supplemental Information for Focused Program Competition 98-03," http://www.atp.nist.gov/atp/97wp-ppr.htm, last viewed (6/23/05).

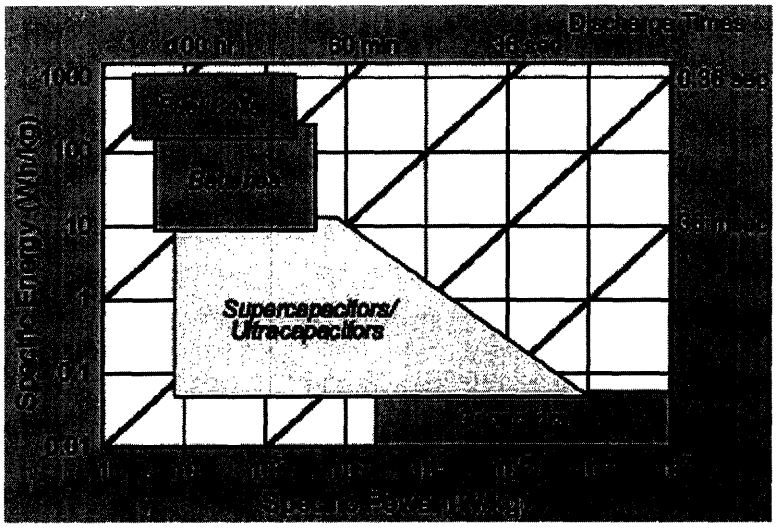

Figure 1: Ragone Plot showing energy vs. power relationship for four categories of devices. Reproduced from Thomas and Qidwai (2005).[1]

Fuel cell systems, however, pose difficult challenges for many portable devices because of the lack of hydrogen infrastructure. The development of direct fuel cells, which do not require reforming hydrocarbon fuels, remains a difficult proposition for many applications when one considers the difficulty with integrating liquid fuel storage for miniaturized devices, possible emissions and safety concerns, and reuse or maintenance issues. Miniaturization of fuel cells remains an on-going area of research and is promising in the mid-term future (5-10 years).

Rechargeable batteries may remain a dominant, commercialized technology to meet portable power needs for the near term and mid-term future, particularly for powering micro-scale applications. New applications for portable power sources of micro and nano-scale dimensions have prompted integration of thin film and semiconductor processing techniques to fabricate electrochemical storage devices.[2-4] Some of the most common material systems used for both primary (one use) and secondary (rechargeable) batteries are compared in Figure 2 and in Table 1. Lithium based systems have the highest power and energy densities compared to other secondary battery systems and are the focus of this dissertation. The next section discusses the workings of a lithium ion cell.

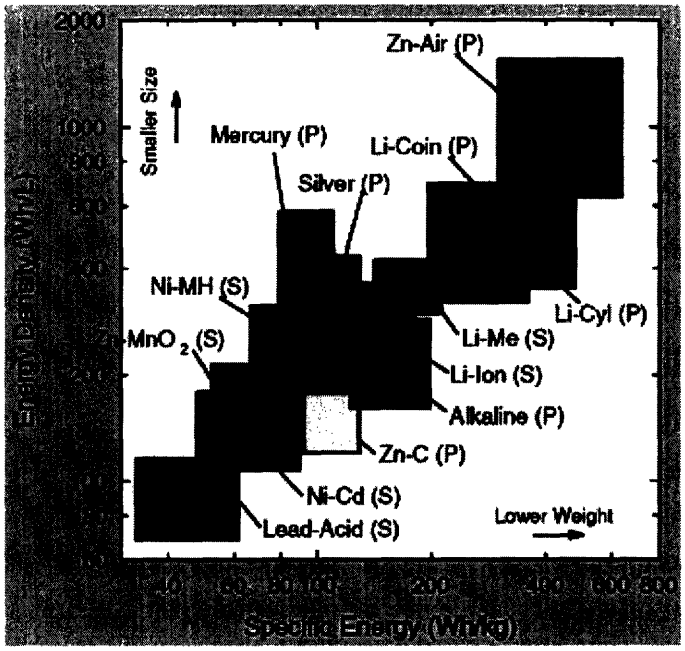

Figure 2: Plot of volumetric versus gravimetric energy density. P = Primary batteries (single use), S = secondary batteries (rechargeable). Reproduced from Thomas and Qidwai (2005).[1]

Table 1: Comparison of battery systems. Note specific power and energy values. Reproduced from Shukla et al. (1999).[5]

Cell Type	Nominal (V)	Specific Energy (Wh/kg)	Energy density (Wh/l)	Specific power (W/kg)	Power density (W/l)	Self discharge life (%/month)	Cycle	
Lead-acid	2.0	35	70	<200	<400	4-8	250-500	*Least-cost technology*
Lithium-ion	3.6	115	260	200-250	400-450	5-10	500-1000	*Intrinsically safe; contains no metallic lithium*
Lithium-polymer	3.0	100-200	150-350	~ 200	~ 350	<1	200-1000	*Not yet available commercially; contains metallic lithium*
Nickel-cadmium	1.2	40-60	60-100	140-220	220-350	10-20	300-700	*Exhibits memory effect and contains toxic cadmium*
Nickel-metal hydride	1.2	60	220	130	475	30	300-500	*No memory effect; cadmium free*
Zinc-air	1.2	146	204	150	190	<5	<200	*Requires air management*
Na-$NiCl_2$	*2.6*	*100*	*160*	*150*	*250*	*~ 1*	*~ 1000*	*High-temperature*

Workings of a Battery

The lithium ion battery works via a gradient in chemical potential between the cathode and anode (or positive and negative electrode respectively).[‡] In today's commercially available lithium-based systems, the cathode is a powder composite consisting of metal oxide, polymeric binder, and electronically conducting carbon additives as displayed in Figure 3. Only the oxide is electrochemically active with lithium under the typical voltage regime (4.2-2.2 Volts). In commercial cells, the anode usually consists of a composite mixture of graphite and binder. By contrast, thin film batteries have cathodes that consist solely of the active oxide material and anodes comprised solely of lithium metal, a lithium alloy, or a transition metal oxide. Upon discharge of the cell, a topotactic reaction occurs between lithium ions and the transition metal oxide. Electrons simultaneously travel through the external circuit and perform work, before eventually compensating the charge introduced by the lithium ions. This discharge process is shown in Figure 3 below. During the charge process, energy is supplied to reverse this process.

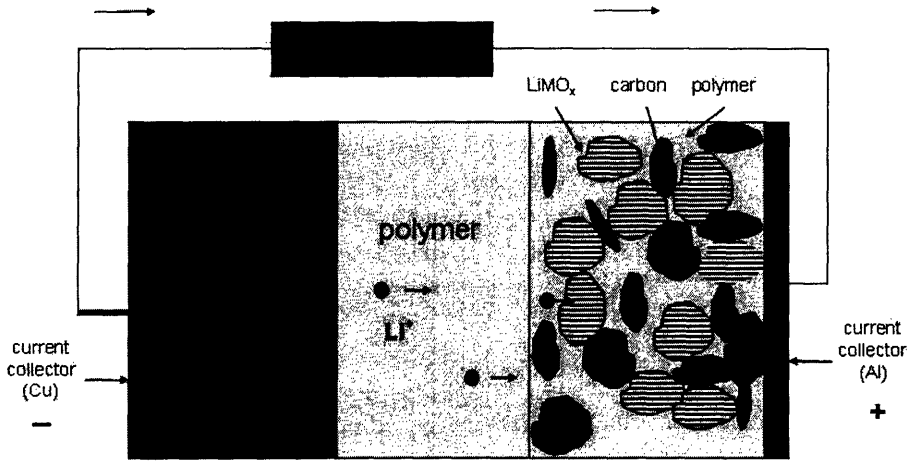

Figure 3: Discharge process in a composite lithium-ion battery

The most desirable performance attributes of a battery typically are (1) high gravimetric and volumetric energy and power densities, (2) resistance to capacity fade, translating into a long

[‡] The term 'positive electrode' will be used interchangeably with the term 'cathode,' having become convention in lithium battery literature (and analogously for 'anode' and 'negative electrode'). Strictly speaking, the cathode refers to the electrode at which reduction is occurring (or the positive electrode during discharge).

cycling life, (3) stability during overcharge conditions, translating to higher safety (4) low self-discharge, (5) a wide temperature range of operation, (6) low cost, (7) recyclable, and (8) low toxicity. Achieving high energy and power densities requires choosing a positive electrode with a large accessible capacity (as opposed to theoretical) within the voltage range of interest. The battery architecture should be such that it limits the amount of inactive material used, which include the electrolyte, electron-conductive additives, binder, current collectors, packaging, and wires. Attributes (2) through (5) are a function of a number of intrinsic material parameters and cell-design properties, while cost, recyclability, and toxicity are functions of the materials system and their inherent ease in processing and manufacturing.

This body of work focuses on the cathode, which often remains the limiting factor for systems in terms of energy and power density.

Purpose

New applications for power sources of micro and nano-scale dimensions have prompted integration of thin film and semiconductor processing techniques to fabricate electrochemical storage devices.[2-4] While rechargeable lithium batteries have been available for some time now, their potential use has been limited by weight considerations, insufficient energy density, safety issues, and relatively high costs.[6] Several lithium thin film battery architectures with small footprints have been proposed for powering electronic devices such as remote sensors, implantable biomedical devices, Smartcards, MEMS devices, and CMOS memory.[3, 7-10] The overall performance of miniaturized power sources is constrained by their architecture (i.e. cell design) and material properties (e.g. microstructure, composition, orientation). Both improvements in material systems and innovations in battery architectures will be necessary for meeting demand for increased battery performance, including the need for higher energy and power densities at lower costs. In thin film batteries, the cathode and interfacial properties often dictate the kinetic limitations of the cell, making investigation into these areas germane.[11-15]

Several groups have reported on the significance of the cathode film microstructure and orientation on the electrochemical performance of thin films.[16-20] Film morphology, including grain size and distribution, shape, orientation, and crystallinity, can vary as a function of the deposition method, deposition parameters, choice of substrate, and post-deposition heat treatment.[21-23] For instance, favorable orientations can enhance the electrochemical kinetics in layered compounds (e.g. $LiCoO_2$, V_2O_5, and $LiNiO_2$) as a result of diffusion being anisotropic in

these systems.[19, 20, 24] Molecular dynamics simulations have also been used to show that both intergranular regions and grain orientation affect Li ion transport.[25-27] Cocciantelli et al. reported lowered current rate performance with larger, less favorably oriented V_2O_5 grains.[28] Their work suggests that slow diffusion kinetics can lead to partial phase transformation and the persistence of lithium-poor phases. Other groups have also shown or suggested that grain size, grain boundaries, and film stress can affect the diffusion kinetics of the electronic and ionic conduction properties in ceramics.[29, 30] While much of the literature has studied the favorable effects of nanoscale dimensions in composite-based electrodes,[16, 31-37] nearly dense thin films can pose different structural challenges at the nanoscale.

This dissertation examines the question of how the cathode can be designed to improve electrochemical performance. Specifically, the work examines the question of how the microstructure of vanadium pentoxide (V_2O_5) can be designed to improve the current rate performance of thin film batteries. V_2O_5, a layered compound, provides a model system from which to investigate questions of microstructure design applicable to other cathode systems. Some of the questions this dissertation addresses include:

1. How can the microstructure be controlled in thin film V_2O_5 cathodes?
2. What are the effects of phase transformation kinetics on performance?
3. What are the effects of microstructure on kinetics?
4. How can the cathode be optimized to improve energy and power density?
5. What are the limiting kinetic parameters of V_2O_5 systems?

Chapter 2 provides a review of relevant antecedent research in materials for batteries. Chapter 3 briefly discusses the experimental methods used in this body of work. Chapter 4 investigates the thin film microstructure and film properties. Chapter 5 presents a study focusing on the phase transformation aspects of V_2O_5 and the resulting electrochemical performance. Chapter 6 looks at both grain boundary effects and film thickness effects on the current rate performance of V_2O_5 thin film systems. Chapter 7 presents work to characterize the kinetic parameters of the V_2O_5 system, followed by a conclusion and suggested directions in chapter 8.

Chapter 2: Literature Review

This chapter reviews relevant studies on thin film batteries, with specific attention on the relationship between cathode microstructure and cell performance. Next, a review is provided of efforts to model the transport phenomena in the cathode and accompanying experimental work. The chapter is concluded by review of work evaluating interfacial properties between the electrode and solid polymer electrolytes.

Thin film Batteries

Thin films oxides have been fabricated for many years by the semiconductor industry for electronic and optical devices using techniques such as sputtering, evaporation, chemical vapor deposition (CVD), pulsed laser deposition (PLD), and molecular beam epitaxy (MBE). [38-42] The first applications of thin film electrodes for secondary batteries date back to the early 1980s when Kanehori et. al. reported the fabrication of a cell composed of $TiS_2/Li_{3.6}Si_{0.6}P_{0.4}O_4/Li$. [4] Levasseur and Creus followed by reporting on lithium-based, thin film rechargeable batteries incorporating glass electrolytes, including $Li/Li_2S\text{-}SiS_2\text{-}P_2S_5\text{-}LiI/GeSe_{5.5}$ and $Li/Li_2S\text{-}SiS_2\text{-}P_2S_5$ $LiI/LiI/B_2O_3\text{-}V_2O_5$ systems.[44, 45] Over the course of the1990s, Dudney et al. (Oak Ridge National Lab) and Jones et al. (Eveready Battery Co) led the field by improving upon thin film battery design concepts. [14, 46-50] Their work led to a number of changes on the thin film concept, including the use of ceramic nitride-based electrolytes, inclusion of protective coatings between the lithium metal and electrolyte, and development of "lithium-free" microbatteries. Dudney tested a range of cathode and anode systems, including V_2O_5, $LiCoO_2$, $LiMn_2O_4$ as cathodes and lithium metal, silicon-tin oxynitrides, Sn_3N_4 and Zn_3N_2, and Cu metal films as anodes.[8, 15, 19, 47, 51-55] These thin film systems incorporated a glassy electrolyte, lithium phosphorus oxynitride ('LiPON''). In contrast, Jones and Akridge incorporated glassy sulfide electrolytes and TiS_2 and $LiMn_2O_4$ as electrodes. Figure 4 demonstrates one typical "on-board" chip design. Despite significant research effort, thin film batteries had limited commercialization over the 1990s despite the ability to manufacture these devices into complex or unique shapes. Mainly, this was due to a lengthy production process.[56] Over the past several years, however, companies have

been moving beyond the prototype stage to the commercialization stage. Numerous start-ups[4] are now vying to market "flexible" thin film batteries due to increasing opportunities to integrate thin film batteries onto chips, RFID tags, smart cards, implantables, solar cells, and even micro-satellites.

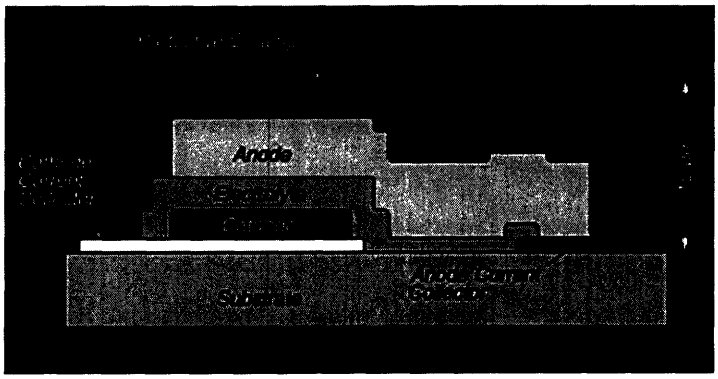

Figure 4: Schematic of Thin film Battery Developed at Oak Ridge National Labs

Vanadium Oxide Films

Interest in thin film, vanadium oxides began with work by Baudry (1991) who performed diffusion studies, followed with studies by Bates (1994), Bae (1996), Julien (1995) and McGraw et. al.(1999) [14, 57-60]. It is noteworthy to mention that much of the basic science was investigated in work during the 1960s on bulk vanadium oxides, intended for electrochromic display devices and cathodes. Later studies on the nature of single-crystal, vanadium oxide surfaces were also performed in the 1990s by Oshio (1992) and Smith (1995).[61, 62] Smith et. al. (1996) later complemented scanning probe microscopy studies with plots of partial and total surface electron-densities to reveal the surface structure of V_2O_5 and V_6O_{13}. This work formed the basis for further studies to understand the interface reaction properties between the surface, lithium ions, and the electrolyte.[63, 64]

Several groups studying thin film Li/V_2O_5 systems have reported cycleability for over 10,000 cycles with little change in performance (<2% capacity fade).[49, 65] In comparison, bulk-sized systems (> 200 nm powder, or > 5 μm films) typically cycle only several hundred cycles, while gel-electrolyte based lithium ion cells (e.g. Sony Corporation, using a $LiCoO_2$ as the cathode material) are rated for approximately 1000 cycles. [66] Bates (1994) attributed this order

[4] Some of these start-ups include: Oak Ridge Micro Energy, Inc.; Solicore, Inc.; Cymbet Corp; PowerPaper, Ltd, Front Edge Technologies; Qualion; Excellatron; Bolder Technologies Corporation; Lithium Power Technologies. Notably, there is little product differentiation between many of these companies.

of magnitude enhancement in performance to the rigidity of interfaces between the electrodes and ceramic electrolyte (i.e. lithium phosphorus oxynitride, LiPON).[14]

Microstructure, Orientation, and Morphology

The major influences of sputtering process parameters on microstructure have been studied in depth.[67] In addition to the choice of materials system, other factors can influence film morphology (including grain size and distribution, shape, orientation, and crystallinity), such as the deposition method, deposition parameters, choice of substrate, and post-deposition heat treatment.[21-23] Ground-breaking work which related thin film microstructures to processing conditions was presented by Movchan and Demchishin (1969), who presented the Structure Zone Model.[23] The model described the relationship between pressure and temperature on the thin film microstructure of metals and metal oxides, as shown in
Figure **5**. Three microstructural zones are evident in the figure: (1) tapered grains with regions of porous material ($T < 0.3\ T_{melting}$), (2) columnar-type grains with distinct boundaries ($0.3T_{melting} < T < 0.5T_{melting}$), and (3) equiaxed grains also with distinct boundaries ($T > 0.5\ T_m$). More recent work has focused on Monte Carlo and molecular dynamics simulations to describe the processing-structure relationship in depth.[68-74]

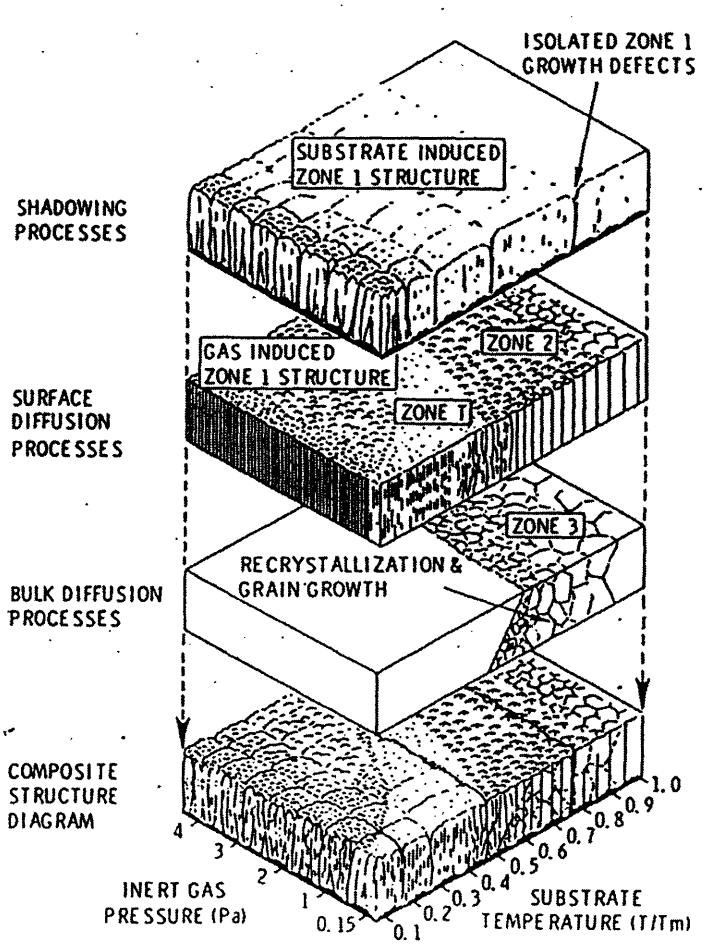

Figure 5: Structure Zone Model, based on work by Movchan and Demchishin (1969),[23] followed by Thornton (1974).[75] The diagram shows the effects on microstructure from shadowing, surface diffusion, and bulk diffusion across Argon pressure and temperature. The superposition of these effects result in the composite structure diagram (bottom), representing the actual microstructure.

The advantages of sputtering as a method for depositing thin films are well known and documented in general processing-oriented literature. These advantages include control over stoichiometry and the ability to fabricate ternary and quaternary compounds through reactive, RF, and co-sputtering. In general, the higher energies involved in sputtering typically result in better adhesion and packing densities than other methods. Control over the processing parameters makes depositions more repeatable, automation-friendly, and uniform.

Several groups have reported on the significance of thin film microstructure and orientation on the electrochemical performance.[16-20] For instance, favorable orientations can enhance the electrochemical kinetics in layered compounds (e.g. $LiCoO_2$, V_2O_5, and $LiNiO_2$) as a result of diffusion being anisotropic in these systems.[19, 20, 24] Bates et al. suggested that increasing the fraction of favorably-oriented grains in $LiCoO_2$ films can improve the obtained energy at higher discharge rates, although experimental verification was not possible due to high interfacial resistances.[19] Bouwman et al. demonstrated that orientation of thin film $LiCoO_2$ affected the intercalation rate and obtained capacity.[20, 24] Molecular dynamics simulations have also been used to show that both integranular films and grain orientation affect the Li ion transport.[25, 27] Cocciantelli et al. reported differences in performance with grain size and morphology of V_2O_5 powders.[28] Other groups have either shown or suggested that grain size, grain boundaries, and film stress can also affect the diffusion kinetics of the electronic and ionic conduction properties in ceramics materials.[29, 30]

Cell Modeling and Kinetics

A large body of work modeling and characterizing intrinsic material parameters of the electrochemical cell is available. A recent review by Subramanian et. al. (2000) summarizes some of the previous work and also discusses the main governing equations for porous electrodes.[11] Many studies have been limited to determining the kinetic parameters for one particular aspect (e.g. diffusion coefficients in the cathode). However, determination of the overall rate limiting steps in a cell is non-trivial, due to the multitude of processes involved, including electron transfer at the substrate-film interface, ionic transport in the film itself, mass transport in the electrolyte (migration, diffusion), charge transfer or extraction at the film-electrolyte interface, double-layer charging and passive layer formation, and heterogeneous reactions at the interfaces. [12, 13] Examples of models attempting to characterize these processes include one describing double-layer capacitance in a lithium ion cell by Ong and Newman (1999), a concentration-dependent diffusion study by Lantelme et. al. (2000), and a mass transport in electrolytes model by Verbrugge et. al. (2000).[76-78] In particular, work by Newman and Doyle (1997) provided simulated results of capacity-rate behavior in a porous electrode based on analytical models.[79] The showed the expected performance behavior for three

situations, namely a (1) transport-limited liquid electrolyte, (2) diffusion-limited electrode, and (3) transport-limited solid polymer electrolyte.

Experimental work to determine the materials parameters have included (but are not limited to) use of techniques such as AC impedance, impedance spectroscopy, and intermittent titration techniques.[80-82] The latter two approaches allow for evaluation of the lithium diffusion coefficient based on analytical models incorporating Fick's Law. Because the classical analysis assumes diffusion only in a single phase system, experimental work using this analysis has limited (if any) applicability to two phase regions in the cathode. Unfortunately, most of a cathode material's capacity is obtained during phase transformation. Additionally, classical analysis assumes a constant diffusion coefficient, an assumption seldom found in Li-insertion compounds. For instance, Lantelme et. al. have used digital simulation of transport equations to show that a concentration-dependent diffusion coefficient is necessary in considering $Li_xV_2O_5$.[77, 83] The use of phase-field models to investigate Li diffusion in V_2O_5 by Han and Ceder (2004) also has shown that the gradient energy term may not significantly influence experimental results.[84]

The topotactic insertion reactions occurring in the cathode lead to structural changes induced by growth of a second phase. Phase boundary motion needs to be also considered in evaluation of the transport kinetics. However, the mechanism and kinetics of phase transformation are poorly understood. Iriyama et al. (2000) examined the insertion of Li into α-MoO_3 using TEM analysis. It was shown that lithium ions insert randomly into some preferred crystallites at the surface while other crystallites remain unchanged. Even at higher lithium insertion levels, some layers were found to be unreacted or containing defects. Phase boundaries between phases were not observed, suggesting that phase boundaries may not simply be modeled as a single planar front moving through the film. Rather, the results suggest the phase boundary may consist of multiple boundaries forming randomly at the surface. Mathematical models are only beginning to accurately reflect the complexity in two phase systems, such as the use of a two phase shrinking core model recently introduced by Srinivasan and Newman (2004).[85]

Grain Boundary Theory

A review of work on grain boundary theory relevant to thin film batteries is present here. This review is intended to provide background to the experiments described particularly in chapter 6. It is important to note that most work on grain boundaries (GBs) have focused on metal systems as opposed to ceramic systems. Nanocrystalline structures, as commonly found in thin film cathodes, are only recently being investigated with respect to the effect of GBs on transport properties. GB diffusion research is still scarce and full of controversy.[86]

Classical boundary diffusion theory has been built on metallic systems.[86] Experimental studies have concentrated largely on bulk single crystals or polycrystalline, coarse grained metals.[30] GB diffusion in ceramic systems differ from metals in two key areas. First, metal oxide systems are ionic solids involving charged species which influence the microchemistry. Second, in electrochemical energy storage devices the diffusing species are ions as opposed to neutral species found in metallic systems. Charged species would be expected to have additional interactions with an ionic compound at the surface and within the bulk.

GB effects may be expected to affect thin film battery performance in several ways. First, GB diffusion may be enhanced (or hindered), leading to changes in the current rate performance. Alternatively, phase transformation may be affected by the presence of GBs as in the case of phase boundary motion being impinged at the interface due to differences in the chemical environment and structure. GB diffusion may also allow phase transformation to begin at *different locations* and/or proceed at *different rates* than might otherwise occur in a single crystal.

In metallic systems, GB diffusion is known to provide fast, short-circuit pathways for diffusion. [87] This GB diffusion process is influenced by several properties, including the type of defect and concentration along GBs, the segregation of diffusing species to GBs, the structure of GBs, and the composition of the GB. The Fisher model has been used as a foundation for GB theory and is described elsewhere (Fisher 1951).[88] It is based on a simple, single GB of width δ, separating two slabs and perpendicular to the surface. A diffusion coefficient, D_b, can be distinguished from D_v, the volume diffusion coefficient as can a different concentration c_b and c_v of the diffusing species.

Harrison (1961) first identified models for different diffusion regimes occurring with temperature, in which D_b or D_v will dominate.[89] These regimes, A, B, and C, are based on

temperature ranges relative to T_m. For instance, for bulk samples regime C dominates when $T < 0.3T_m$, and it may be possible to separate D_v and D_b because the near-surface concentration will be D_v controlled while any presence of a long penetration tail will be due to D_b. However, for thin films, the finite diffusion lengths of the sample pose difficult problems in modeling. For cathode thin film samples, the complexity of the analysis is also caused by sensitivity to the back surface (substrate),the presence of *interphase* boundary and surface diffusion, large surface to volume ratios and small grain sizes, defect densities, film stress, and the presence of concentration and electrochemical potential gradients.[90]

It is interesting to compare the GB volume in a sample to the bulk grain volume. GBs are typically described as amorphous and treated as intergranular films of 0.5-1 nm in width. Hence, even in fully crystalline films, an effective amorphous GB volume exists. From an electrochemical standpoint, the theoretical capacity for this amorphous region will be different than for the crystalline bulk volume. The lithium insertion process will also tend to occur at different potentials, giving an effective mixed potential system. The resulting potential curve might be expected to be a combination of the capacity from both the GB volume and crystalline volume, weighted by the fraction of GB to bulk material. Garofalini et al. has predicted that Li ion transport in amorphous vanadia to be similar to the fast <010> in crystalline V_2O_5, suggesting amorphous grain boundary regions may be pathways for fast diffusion.[25, 26] Unlike short-circuit diffusion in electronics, which is highly undesirable, in microbatteries it is very desirable from a fast kinetics standpoint. This thesis will begin to explore experimentally the effects of grain boundaries on the current rate performance.

Chapter 3: Processing and Characterization Techniques

The first portion of this chapter discusses the deposition process by which the V_2O_5 films are formed. Portion two of the chapter covers the electrochemical analysis techniques performed on the cathode and solid polymer electrolyte (SPE) materials, followed by a section on additional characterization techniques.

Thin film Deposition:

In the work throughout the thesis, the main deposition processes used was reactive RF-sputtering using a Kurt Lesker CMS-18 Deposition System incorporating 1 RF gun and 2 DC guns (Kurt J. Lesker, Clairton, PA). Unless otherwise noted, thin film VO_x cathode materials were prepared via RF sputtering of V_2O_5 targets onto aluminum foil (40 μm thick, 99% purity, annealed, Goodfellow Corp., Devon, PA). Other substrates used included ITO (~10 Ω/cm), glass slides, and Si <100>. A 7.6 cm (3″) diameter V_2O_5 target was prepared in-house by pressing and sintering of V_2O_5 powder in air at 640°C. The target was subsequently bonded to a Cu backing plate using silver-loaded epoxy. Other V_2O_5 targets were purchased through both SCI Materials, Inc. and Kurt J Lesker, Inc.

Sputtering conditions generally ranged between 250-350 Watts using the RF gun and V_2O_5 targets. Argon was used as the sputtering gas along with 0 - 10 vol. % oxygen as the reactive gas. A mass flow controller was used to limit the flow of both argon (35-40 sccm) and the reactive oxygen gas (99.97% purity Ar:O_2 mixture, 60:40 by vol%, 1.5-10 sccm). The latter was released via a gas ring surrounding the substrate. Partial pressures for the argon were generally between 8-10 mTorr, with the oxygen:argon flow adding 1-2 mTorr. Chamber pressures before sputtering were allowed to fall below $5x10^{-6}$ torr and targets were pre-sputtered (with shutters closed) for 10-30 minutes depending on the material. Typical sputtering rates were between 0.6 – 0.7 nm/min for V_2O_5, particularly low because of the large substrate-target distance in the system (28 cm) and low relative power used (5.5-7.7 Watts/cm^2). Absolute DC bias values typically ranged between 600-800 volts.

DC and RF reactive sputtering of vanadium metal targets also were used to produce V_2O_5 films. In general, the technique is highly sensitive to oxygen concentration and requires some substrate heating to improve oxygen incorporation into the film. The sputtering system used

incorporates quartz lamps as both bake-out heaters and substrate heaters. Setpoint temperatures were generally between room temperature to 650°C. The substrate temperatures followed a relationship, $T_{substrate} = 0.59T_{substrate} - 31.363$ (°C). Even if no external heating applied during the sputtering, substrate heating inevitably occurred as a result of the sputtering process. Based on thermocouples near the substrate and previous temperature calibrations, the sample surface heating remained below 150°C over the course of sputtering, well below the crystallization temperature for vanadium pentoxide.

Samples that were post-annealed were heated in air using Linberg-Blue tube furnaces. Heating rates generally ranged from 0.5 to 70°C/min. The temperature used was between 200-500°C, held for 1.5 - 24 hours. Subsequent cooling down to room temperature was allowed to proceed at rates ≤10°C/min. Film thicknesses were confirmed using an *in situ* quartz crystal, surface profilometry (Tencor P-10), and/or cross-sectional SEM (JEOL 6320 FEGSEM).

Electrochemical Analysis

Test Cell Fabrication

Cell fabrication consisted of the V_2O_5 serving as the working electrode (WE) and lithium metal serving as the counter (CE) and reference (RE) electrode. Thin film cathodes materials were 8 to 12 mm diameter depending on the experiment. The lithium CE generally was 18 mm in diameter and 2 mm thick. Cell materials were fabricated within an argon-filled glove box (< 2 ppm moisture levels). Two electrode cells consisted of stainless steel plugs serving as current collectors, which were placed into a teflon sleeve and sealed with brass end caps. The cells were then wrapped with ParaFilm to prevent moisture from entering into the system and housed in a sealed, glass bottle with leads attached. The liquid electrolyte used throughout the study consisted of 1 M $LiPF_6$ in ethylene carbonate: dimethyl carbonate (50:50 wt%), (Merck Industries). Three electrode cells consisted of sealed glass containers with lead wires attached to both stainless steel and copper clips, which were subsequently attached to the electrodes. Lithium metal was used separately for both the counter and reference electrodes.

All electrochemical analysis was performed using a Solatrtron 1286 or 1287 potentiostat, or a Maccor 4000 Series 32 Channel System. All impedance measurements and AC voltammetry measurements were performed on Solatrtron 1260 Impedance/Gain-Phase Analzyer, a Solartron 1255B or 1250 Frequency Response Analyzer (FRA) depending on the test needs. Solartron

potentiostats and FRAs were run in a coupled-mode when impedance measurements were performed at held potentials.

Galvanostatic Techniques

Galvanostatic techniques generally involves application of a constant current source across the cell and measurement of the potential response. A constant current is applied acting between the working and counter electrodes. Upon application of discharge current, reduction occurs in the working electrode (e.g. V_2O_5 cathode) vis-à-vis reactions involving a lithium ion insertion, a corresponding valence shift in vanadium (e.g. $V^{5+} \rightarrow V^{4+}$), and a compensating electron to maintain charge neutrality. As the constant flux of lithium proceeds, the film concentration progresses across the Li-V_2O_5 phase diagram. As the discharge process proceeds, the α-$Li_xV_2O_5$ ($0<x<0.1$) transforms into ε-$Li_xV_2O_5$ ($0.4<x<0.6$), and subsequently δ-$Li_xV_2O_5$ ($0.85<x<0.95$).

When all α-$Li_xV_2O_5$ concentration at the surface is transformed to ε-$Li_xV_2O_5$, the potential will be rapidly driven to lower potentials until the next reduction process can start. This second reduction process involves the transformation of the ε phase to the δ phase. An example of a potential curve vs. lithiation into V_2O_5 appears in Figure 6 for both crystalline and amorphous materials. The phase boundaries are also shown.

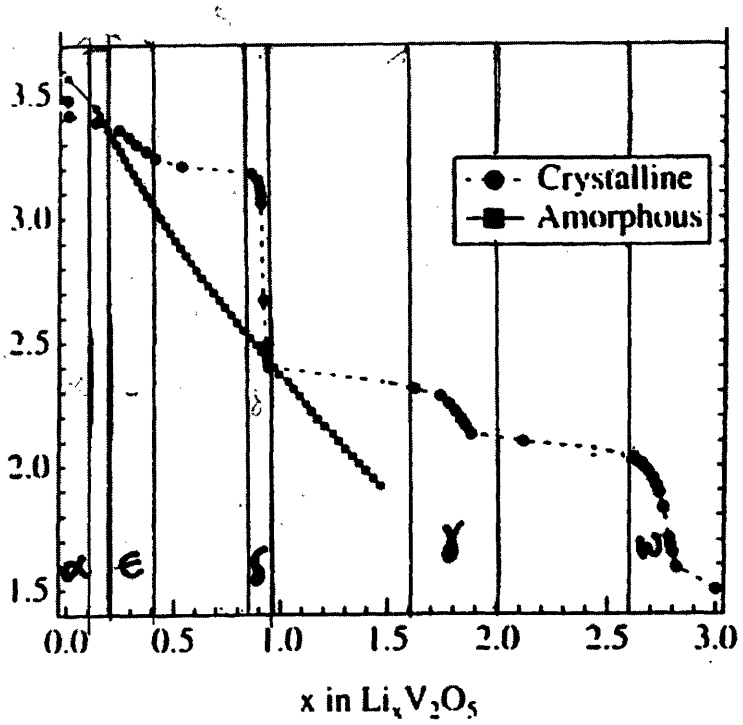

Figure 6: V_2O_5 Potential Curve with Lithiation. Vertical lines denote phase boundaries. Amorphous and crystalline V_2O_5 shown. Image from McGraw (1999).[60]

In general:

$$yLi^+ + Li_xV_2O_5 + ye^- \rightarrow Li_{x+y}V_2O_5 \qquad (1)$$

Applied to the α → ε transformation, equation (1) becomes:

$$Li^+ + 2.5Li_{0.1}V_2O_5\ (\alpha) + e^- \rightarrow 2.5Li_{0.5}V_2O_5\ (\varepsilon) \qquad (2)$$

(Note that 2.5 moles of $Li_{0.1}V_2O_5$ is needed to balance the equation for each lithium ion involved). With each Li^+ ion incorporated, the valence state of one vanadium is lowered by one. In terms of the generalized vanadium valences, eqn (1) can be written as:

$$yLi^+ + Li_x[(2-x)V^{5+}, xV^{4+}]O_5 + ye^- \rightarrow Li_{x+y}[(2-x-y)V^{5+}, (x+y)V^{4+}]O_5 \qquad (3)$$

which for the α → ε transformation becomes

$$Li^+ + 2.5Li_{0.1}[1.9V^{5+}, 0.1V^{4+}]O_5\ (\alpha)\ + e^- \rightarrow 2.5Li_{0.5}[1.5V^{5+}, 0.5V^{4+}]O_5\ (\varepsilon) \quad (4)$$

The potential of the working electrode is driven to the value characteristic of the above reaction in which α-$Li_xV_2O_5$ is transformed to ε-$Li_xV_2O_5$. Note that in non-equilibrium conditions, this potential reflects the surface potential and does not necessarily reflect the potential of the inner electrode material.

For "rechargeable" systems whereby the reaction can proceed in the reverse direction, a constant current can be driven so that oxidation occurs at the working electrode (i.e. V_2O_5). This is commonly known as the "charge" step. If all the reactions are reversible (i.e. battery is rechargeable), the potential curve during charge virtually mirrors the curve obtained during discharge, offset slightly to take into account *iR* from the cell, diffusion limitations, or activation.

Some general performance measures of the electrochemical cell can be ascertained through the potential-time curves. The following metrics may be determined:

$$C = I \bullet t \quad (5)$$

$$E = I \bullet t \bullet V(t) \sim I \bullet t \bullet \overline{V} \quad (6)$$

$$P = \frac{dE}{dt} = I \bullet V(t) \approx I \bullet \overline{V} \quad (7)$$

Here, C is the capacity, E is energy, P is the power, V is potential, I is the current, and t is the discharge time. In *capacity-rate* testing, the obtained capacity is measured as a function of current density. This allows for the obtainable power and energy to be compared, commonly known as a *Ragone* plot.

Experimental:

For the capacity-rate experiments, cells were first discharged and charged three times, generally at 10 $\mu A/cm^2$ between 3.9 to 2.5 volts in order to "pretreat" the cell before capacity-rate testing. This pretreatment was conducted for all capacity-rate experiments and is generally known to allow for formation of the SEI on the lithium and for losses attributed to irreversible loss during the first discharge to be accounted.[91] Subsequently, cells were discharged from the highest current rate to the lowest current rate. Depending on the rate capability of the cathode

material and overall cell, the current densities ranged from > 5000 $\mu A/cm^2$ (i.e. 5 mA/cm^2) to as low as 1 $\mu A/cm^2$. All charge currents were kept equal or below the discharge current rate. A potentiostatic hold at 3.9V with a $5x10^{-7}$ ampere cutoff was applied after charging to ensure the oxides were fully delithiated. A 3 hour hold at this potential was generally found to be sufficient to fully charge films – hence a time limit was also set to cutoff the potential hold. For each cell, a partial second scan through the current rates was applied after the first scan to ensure repeatability and that capacity fade did not affect the results. Alternatively, the capacity obtained at the lowest current rate was checked against the theoretical capacity. If the obtained capacity matched well with the theoretical capacity, the presence of significant capacity fade affecting the results was also discounted.

Potential Sweep Methods

Linear DC sweep voltammetry and cyclic voltammetry was performed on systems to acquire current response curves of V_2O_5 cathode materials. The approach entails scanning the potential at varying rates to obtain thermodynamic and kinetic information of the reaction processes occurring. In a reversible system (i.e. fast charge-transfer kinetics, slow diffusion), the peak current is proportional to the square root of the potential scan speed, v.

$$I_p = (2.69\times10^5)n^{3/2}AD_o^{1/2}v^{1/2}C_o^* \qquad (8)$$

where I_p is the peak current, n is the number of electrons involves in the reaction, A is the surface area of the electrode, D_o is the diffusion coefficient of the lithium, and C_o is the bulk concentration of lithium ions in the solution.

Another variant on this technique involves slow-scan cyclic voltammetry (SSCV) in which the scan rate is slow enough that mass transfer is not limited. In this case, the system can be treated as irreversible whereby the reaction kinetics can be accessed. Levi and Aurbach (1997) use the derivation provided by Bard and Faulkner (1980) for thin-layer electrochemistry to describe the above condition. [92, 93] At the slower rates, the peak current for a "thin-layer" (i.e. relatively fast mass transfer) \ becomes directly proportional to the potential scan speed, v.

$$I_p = \frac{n^2F^2vVC_o^*}{4RT} \qquad (9)$$

Experimental:

These methods were applied to V_2O_5 thin films to understand the transition between reversible and irreversible kinetics. SSCV scan rates between 0.025 mV/s to 100 mV/s were applied using thin film systems. In general, the potential ranges used were between 2.1 to 3.9V with the cell assembly similar to that already described above. Current peak magnitudes and potential peak locations were evaluated and compared against the scan speeds, *v*.

Intermittent Titration Techniques

Weppner and Huggins (1977) first proposed using an intermittent titration technique to determine several material properties, including the chemical diffusion coefficient, the component diffusion coefficient, the chemical enhancement factor, and the partial conductivity.[82] Galvanostatic intermittent titration technique (GITT) has been widely used to calculate the diffusion constant of lithium insertion electrodes. The technique is widely used because it allows for a straightforward, experimentally obtainable procedure for calculation of the constant over a range of lithium concentrations. Among the most difficult questions regarding the technique, and other approaches using assumptions of Fickian diffusion, is its significance over two phase regimes. It is clear that the case involving Fick's law assumes a single phase region. It remains uncertain what information (if any) GITT measurements generate in cases where non-Fickian diffusion may dominate.

Most techniques rely on analytical solutions for solving the diffusion coefficient. In these cases, evaluation normally restricts the case to where the diffusion coefficient is constant over the experiment. In GITT, for example, the current pulse is applied over a limited timeframe such that the diffusion coefficient is considered independent of the concentration. It is known however that the diffusion coefficient depends in fact on composition so that in cases where the potential change is large, D(c) is required.

A second factor involved in the diffusion measurements include non-ideality conditions whereby calculating the activity (as opposed to concentration) is necessary. Incorporation of additional terms by introducing D(c) into analytical models lowers the usefulness of these models while making it experimentally difficult to verify.

A third factor for consideration is shown in Darken's analysis,[94, 95] which evaluates the case where the gradient in the chemical potential of a moving species is important, such that

$$\tilde{D} = -D\left(1 + c\frac{\partial \ln(\gamma c)}{\partial \ln c}\right) = -D\left(1 + c\frac{\partial \ln \gamma}{\partial \ln c}\right) = D\omega \qquad (10)$$

where $\tilde{D}$ is the chemical diffusion coefficient, D is the component diffusion coefficient of the active species, γ is the activity coefficient, and ω represents the thermodynamic enhancement factor, the term in parenthesis.[5] The term represents the effects of charged species interacting to enhance diffusion in addition to chemical potential gradients. Its effect is to substantially increase th chemical diffusion coefficient in regions in which the system moves away from ideality.

Testing procedure:

The Galvanostatic Intermittent Titration Technique (GITT) was used to calculate the diffusion coefficient as a function of lithiation following the approach set forward by Weppner and Huggins.[82] The general current pulse and expected potential response is represented in Figure 7.

[5] The thermodynamic enhancement factor, ω, is also known as Wagner's symbol

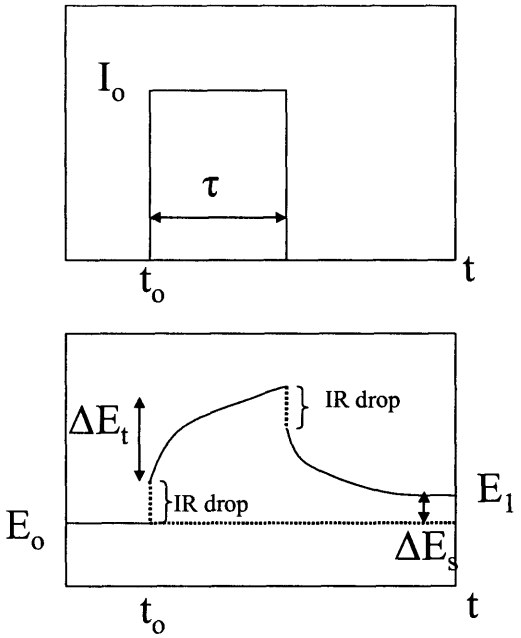

Figure 7: Diagram displaying the intermittent titration technique. The top diagram shows the applied current, the bottom graph shows the potential response.

A 2.5 μA pulse for τ = 12 min was applied, followed by a relaxation until the potential change was less than 5 mV over 1000 s. Under diffusion-controlled conditions, if $\tau << L^2 / \widetilde{D}_{GITT}$, where L is approximated as the thickness of the film, then equation (1) shown below can be used to calculate $\widetilde{D}_{GITT}$, which represents the chemical diffusion coefficient:

$$\widetilde{D}_{GITT} = \frac{4}{\pi}\left(\frac{V_M}{SFz_i}\right)^2\left[\frac{I_o\left(\frac{dE_o}{d\delta}\right)}{\left(\frac{dE_p}{d\sqrt{t}}\right)}\right]^2 \qquad (11)$$

where V_M is the molar volume, S is the effective area, F is Faraday's constant, z_i is the moles of lithium involves in the reaction, I_o is the current pulse magnitude, $dE_o/d\delta$ is the slope of the steady-state voltage curve with lithium concentration, and $dE_p / d\sqrt{t}$ is the slope of the transient voltage curve with the square root of time.[82] Ensuring that semi-infinite diffusion conditions hold for a thin film requires that current pulse time, τ, is much smaller than the time required to diffuse through the total thickness. In some cases, the current was raised to 10 μA pulses or the

time-span shortened in-order to check that these requirements were fulfilled and the obtained results similar.

AC Impedance Spectroscopy

Impedance techniques allow for small perturbations on the working electrode to be made. If the perturbation is small enough, the current-potential behavior can be linearized allowing for simplification in the treatment of kinetic and mass transport.[92] Compared to DC perturbation measurements, AC methods have the advantage of (1) higher-precision (due to the ability to average numerous measurements over a short-time span) and of (2) more precise targeting of specific physical processes which occur within specific frequency ranges. In general, a suite of conditions can be imposed on the working electrode to more readily assess different kinetic and diffusion parameters compared to DC techniques. For instance, in impedance spectroscopy measurements the DC potential is fixed with the frequency range is scanned, allowing for the impedances from the full range of physical processes to be examined. Alternatively, in AC polagraphy or voltammetry, a fixed AC signal is applied upon a scan of the DC potential, allowing such kinetic information as the reaction transfer coefficients to be obtained. Additionally, in some cases higher harmonic responses can be detected, allowing for further quantitative evaluation of kinetic parameters.

The basic AC circuits involve application of a sinusoidal voltage:

$$e = E \sin \omega t \tag{12}$$

where E is the amplitude and the frequency of rotation ω.The current response due to the sinusoidal voltage described by:

$$i = I \sin(\omega t + \phi) \tag{13}$$

where I is the current amplitude and φ the phase angle between the phasors. A pure resistor will have a φ of 0. A pure capacitor will have a φ of $\pi/2$. Mixtures of the two will have values falling between the two.

The physical processes occurring with an electrochemical cell, from charge-transfer across the interface to mass transport through the electrolyte, can be represented as circuit elements in parallel and in series which comprise an equivalent circuit model. Among the most simple equivalent circuit models is shown below

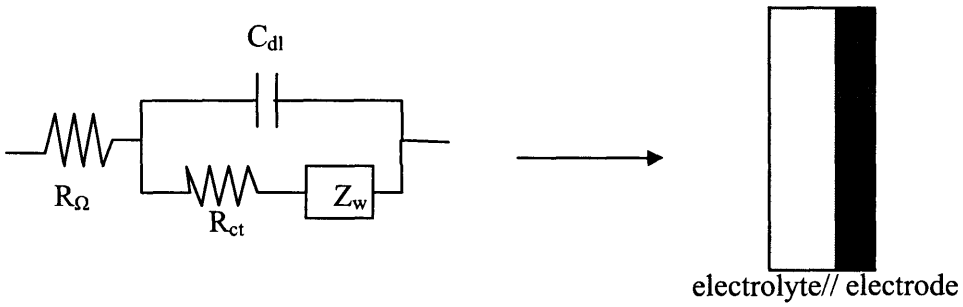

Figure 8: Equivalent circuit model (left) and physical model (right).

Here, R_Ω could represent the resistance associated with the electrolyte and lead wires, C_{dl} the capacitance associated with the double-layer that forms at the interface, R_{ct} the resistance associated with charge transfer, and Z_w a general impedance representing a type of mass-transfer resistance in the electrolyte. The above equivalent circuit is represented in terms of the real and imaginary impedances, shown below as a Nyquist plot (Figure 9). The direction of increasing frequency is shown in the arrows. At high frequency, the lead wires and electrolyte resistance, R_Ω is measured. As the frequency is lowered, C_{dl} becomes dominant at $\varphi = \pi/2$. Further lowering of the frequency allows the charge transfer process to reveal itself. At very low frequencies, the ionic diffusion through the electrolyte is able to respond to the AC signal.

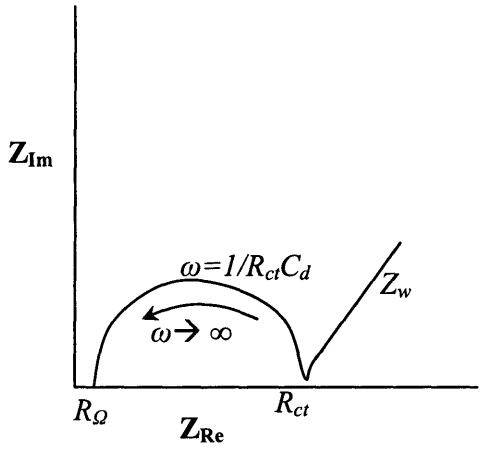

Figure 9: Example Nyquist plot

Experimental:

AC impedance measurements were performed on Solartron 1260 and 1255 impedance analyzers in either standalone configuration or in coupled modes with a potentiostat. The AC bias was generally between 10 - 25 mV with the frequency range between 10^6- 0.001 Hz. The AC bias was kept between 10-25 mV. For measurements requiring a series of impedance measurements at specific potentials, the potential was generally swept and held until equilibrium was obtained, after which an impedance scan was taken. Temperature scans with impedance were performed by placing cells into an insulated tube, subsequently placed within an oil bath. An external thermocouple placed into the insulated tube was used to obtain the temperature of the cell. Cells were generally kept at the setpoint temperature for 2 hours before an impedance measurement was taken. In the case where a solid polymer electrolyte was used, the thickness was estimated by measuring the weight of the dried polymer on the electrode and the area. Spacers were also used to prevent shorting along the edges. When possible, measurements were fitted with a simple equivalent circuit model shown above. Symmetric cells were used to evaluate more complex processes (e.g. solid-electrolyte interphases) and more appropriate equivalent circuits were tested and fitted using ZView fitting software.

AC Voltammetry

AC voltammetry (ACV) can be used to obtain more precise, quantitative information on electrode processes than can be determined through DC methods.[92] The technique involves superimposing a periodic AC signal ($\dot{E}_{ac}$) on a DC potential (E_{dc}) which is varied linearly with time. The sweep of E_{dc} is ideally tuned so that diffusion limitations are not controlling (i.e. a slow scan of E_{dc}). $\dot{E}_{ac}$, in turn, is set to values (e.g. 1 Hz – 100 kHz) high enough that charge-transfer information is accessed. E_{dc} establishes an effective, mean surface concentration (C_o) while $\dot{E}_{ac}$ forces smaller, more rapid concentration variations that can be measured via I_{ac}. Thus, the technique allows for uncoupling of the long-term diffusion established by E_{dc} from the rapid diffusional fluctuations established by $\dot{E}_{ac}$.[92]

For simple, heterogeneous electron-transfer reactions, the standard rate constant and transfer coefficient can be precisely determined. For example, in the case where the dc response is reversible but the ac response is irreversible (i.e. charge-transfer controlled), the amplitude of I_{ac} will be controlled by R_{ct}, the charge-transfer resistance. R_{ct} is dominant at the high-frequency range. The derivation of the analytical solutions has been described elsewhere in detail, and the results of the derivation are presented here.[92] The measurement of the I_{ac} versus DC potential gives the shape of the ac polarogram, and under the aforementioned conditions:

$$I_{ac} = \frac{\Delta E}{R_{ct}} = \frac{F^2 A k^o C_o^* \xi^\alpha \Delta E}{RT}\left(\frac{e^{\beta a}}{1+e^a}\right) \qquad (14)$$

where

$$a = \frac{nF}{RT}(E_{dc} - E_{1/2})$$

$$\xi = \left(\frac{D_o}{D_R}\right)^{1/2}$$

and I_{ac} is the amplitude of the ac current, ΔE the magnitude of the AC potential variation, F is Faraday's constant, D_o and D_R the diffusion coefficients of the oxidized and reduced species, $E_{1/2}$

the half-wave potential, k^o the standard rate constant, C_o^* the bulk electrolyte concentration, α the transfer coefficient, and $\beta = 1-\alpha$. Equation 14 describes the general shape of the ac polarogram.

A key feature of equation 14 is that the transfer coefficient, α, can be calculated if the reversible half-wave potential, $E_{1/2}$, is found. The transfer coefficient describes the symmetry of the energy barrier of the forward to reverse reaction. Its values can range from zero to unity, with one-half describing equal cathodic and anodic activation energies. It is also notable that I_{ac} is linearly dependent on k^o, ΔE, and C_o^* but independent of ω. Varying the frequency, additional kinetic information can be obtained.

A second term of interest is the phase angle, φ, between $\dot{I}_{ac}$ and $\dot{E}_{ac}$, whose relationship is described by:

$$\cot\varphi = 1 + \frac{(2D_o^{\beta} D_R^{\alpha}\omega)^{1/2}}{k^o}\left[\frac{1}{e^{\beta a}(1+e^{-a})}\right] \qquad (15)$$

The important result in this equation is that the maximum in the $cot\varphi$ occurs when $e^{-a} = \beta/\alpha$. Thus, identification of the maximum also allows derivation of the transfer coefficient, α. From equation 15, plots of $cot\varphi$ with $\omega^{1/2}$ allow for k^o to be determined from the slope, once α is known.

Several other approaches to obtaining k^o and α are discussed here, in addition to the $cot\varphi$ vs. $\omega^{1/2}$ approach. These approaches can be used as a cross-check for the obtained physical constants. It has been reported that between forward and reverse scans, a "cross-over" point can be identified, E_{co}, which is strongly dependent on α but independent of virtually all other experimental and system variables. The equation used to describe this relation is:[92, 96]

$$E_{co} = E_{1/2} + \frac{RT}{nF}\ln\left(\frac{\alpha}{1-\alpha}\right) \qquad (16)$$

To evaluate k^o, several approaches are available pertaining to cases where the DC behavior is non-nernstian. One method is to evaluate the peak ratios of the fundamental forward and reverse scans, which will depend on k^o and ΔE_p, the peak separation. A second method is to use the full width, half max values of the fundamental harmonic currents. Finally, the second harmonic peak-to-peak separations can also be used.

DC cyclic voltammetry has become ubiquitous in electrochemical materials research. Although the extension from DC to AC voltammetry has been successfully applied in systems for some time now, virtually no research involving ACV to evaluate battery electrode materials has been reported.[96, 97] The ACV method can be more theoretically challenging and may require slightly more elaborate instruments allowing one to obtain higher-order harmonics. This research aims to explore the utility of using ACV for evaluating Li battery electrode materials. It is important to note that, in comparison to simple electron-transfer reaction of solutions components, the battery systems involve more complex, multi-stepped reactions which add to the complexity of analysis. For instance, solid diffusion of the Li^+ species in the electrode can add additional complexity owing to the spatial extent of the electrode. Traditional electrode theory models systems consisting of metal electrodes and involve only solution-phase diffusion and charge-transfer reactions at the electrode-electrolyte interface.

Experimental:

Cells were tested by first obtaining a DC cyclic voltammagram to access the scan speed at which clearly defined peaks could be obtained. Next, using a Solartron 1250 impedance analyzer coupled to a Solartron 1286 galvanostat, the impedance of the system was obtained to measure the general range of frequencies to use for AC voltammetry. Initial test runs used a range of AC amplitudes (10 - 50 mV), a series of slow DC sweep rates, and a range of frequencies (0.1 – 500,000 Hz) to obtain the correct test conditions. Appendix A discussed the experimental setup in more detail.

Additional Techniques

Unless mentioned otherwise, all additional experimentation was performed in the Center for Materials Science & Engineering at MIT (CMSE). The vanadium oxide thickness was confirmed using surface profilometry (Tencor P-10) and cross-sectional scanning electron microscopy (JEOL 6320 FEGSEM). The surfaces of the samples were analyzed using both SEM and atomic force microscopy (AFM) in tapping mode (Veeco Nanoscope IIIa).

In situ, electrochemical atomic force microscopy (ECAFM) studies were performed with the assistance of Anne Clemencon (MIT, Dept. of Mechanical Engineering). Studies were performed using a Nanoscope IIIa (Veeco Instruments, Inc.) using a liquid cell holder (Figure 10) attached to a Veeco potentiostat. The liquid cell was assembled in a glove box, and briefly brought into atmospheric air to the AFM environmental chamber, which was purged with argon during testing. All tests were run in contact mode. Data acquisition was performed using Digital Instruments Nanoscope SPM software.

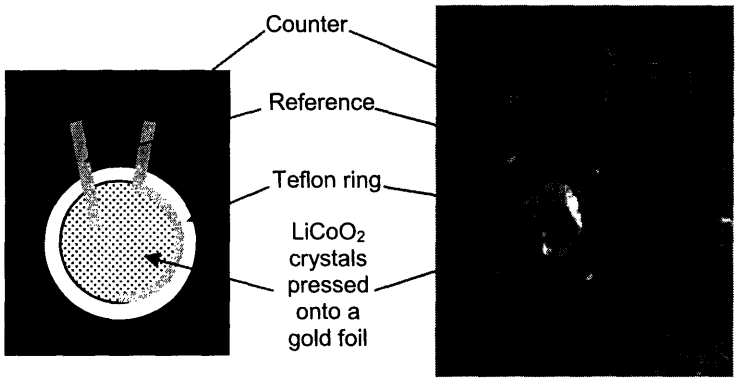

Figure 10: *In situ* AFM setup, courtesy of Anne Clemencon, MIT, Dept. of Mechanical Engineering

Cross-sectional transmission electron microscopy (TEM) specimens were prepared by means of mechanical pre-thinning and polishing, followed by Ar-ion milling. TEM sample preparation and analysis was performed by Professor Valerie Leppert and Dr. Jacek Jasinski (UC Merced) at the National Center for Electron Microscopy, Lawrence Berkeley National Laboratories. The studies were conducted on a JEOL JEM3010 microscope operating at 300 kV accelerating voltage.

Sample compositions, orientations, and lattice constants were determined using a Rigaku rotating anode x-ray diffractometer in Bragg-Brettano mode. Analysis of XRD patterns was performed using a Jade 7.0 software package that enabled pattern refinements and peak fits to be conducted (Materials Data Inc). Lattice parameters were obtained from a least-squares fit of six to eight reflections identified as vanadium pentoxide.

In order to evaluate the film compositions, secondary ion mass spectroscopy (SIMS) was performed on lithiated V_2O_5 films using a Cameca IMS-4f universal magnetic sector SIMS equipped with both oxygen and cesium ion beams (Applied Microanalysis Labs, Santa Clara, CA). The films for the SIMS analysis were sputtered on indium tin oxide (ITO) substrates.

Chapter 4: Thin Film Characterization

Structure of V_2O_5

V_2O_5 consists of an orthorhombic unit cell and is best described by VO_5 square pyramids that are edge and corner sharing, as shown in Figure 11(b). In general, $Li_xV_2O_5$ ($0 \leq x \leq 0.13$) is known as the "alpha" phase and is described by the space group Pmmn (#59) with lattice constants of a = 11.512Å, b= 3.564Å, and c = 4.368Å.[98] It is important to note that other equivalent space groups are often used through literature. For instance, the Pmnm space group is largely isostructural with just the *b* and *c* axis switched Three types of oxygen bonding exists and are designated as vanadyl (O_v), chain (O_c), and bridge (O_b) oxygens.[99] The vanadyl oxygens (2) are located directly above and below the vanadium in the <001> direction, the bridge oxygen (1) serves to connect the vanadiums within a chain, and the chain oxygen (3) comprise the edge sharing for the VO_6 octahedra. One of the oxygen atoms (O_v) in the VO_6 octahedra is weakly associated by a van der Waals bond which allows for easy cleaving in the <001> direction between planes. Due to the loose association of the vanadyl oxygen atom, the structure is often described by VO_5 square pyramids, with corners consisting of oxygen that are edge and corner sharing. The one weak vanadyl oxygen bond causes the vanadium to be displaced slightly from the center of the octahedral so that there is one short and long V-O_v bond (1.577Å and 2.791Å). The resulting V-O_c bonds are also not equidistant due to the pull of the bonds towards the bridge oxygen atoms.

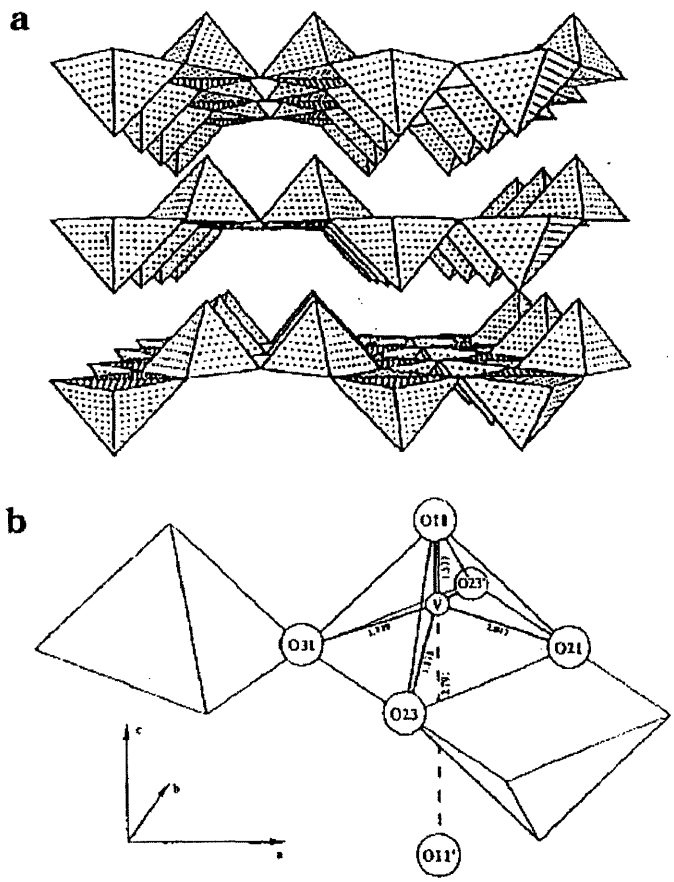

Figure 11: V_2O_5 structure showing (a) V-O layering and (b) vanadium coordination. Reproduced from Dietrich (1993).[100]

The VO_6 octahedra collectively bond along edges and corners to form octahedral chains which compose the layers. The $Li_xV_2O_5$ system can have a number of phases as a function of lithium content and temperature, as shown in Figure 12. The phases discussed below refer to those obtained by varying the lithium stoichiometry at room temperature.

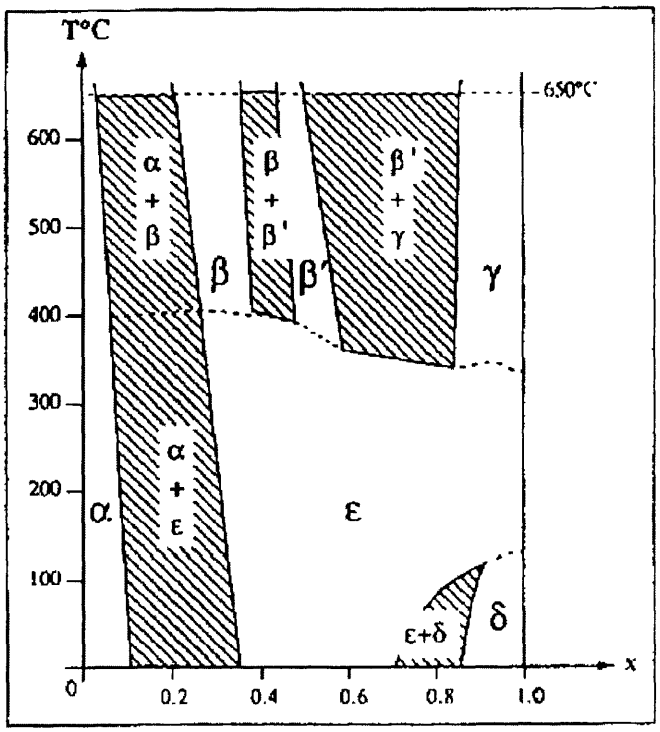

Figure 12: $Li_xV_2O_5$ Phase Diagram: Reproduced from Galy (1992).[101]

Phase Transformation

In general, the Li-V-O system is complex with a wide range of oxidation states and stoichiometries available. The V_2O_5 stoichiometry has among the highest energy density of the Li-V-O family largely because of the higher vanadium valence state resulting in higher potentials, as shown in Figure 13. While V_2O_5 has the highest theoretical capacity, able to intercalate 3 mole Li^+/ V_2O_5 (442 mAh/g), it can only reversibly intercalate in 1 mole Li+/ V_2O_5 without undergoing some degree of irreversible, structural transformation. However, once the structure undergoes this irreversible transformation ($\delta \rightarrow \gamma$), roughly 1.3-1.8 Li^+/V_2O_5 can by reversibly cycled (albeit the original phases and potentials are not retained).

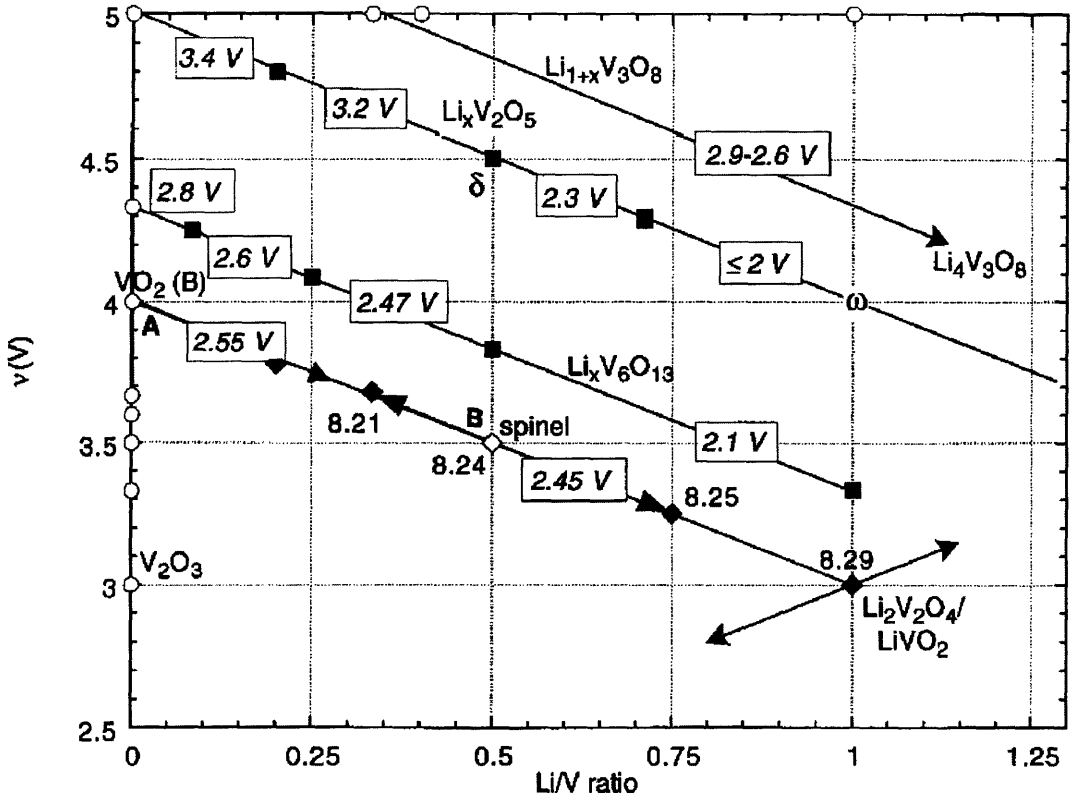

Figure 13: Li-V-O system phase diagram showing the vanadium valence state (v) vs. the lithium/vanadium ratio. Phases for each stoichiometry are denoted by greek symbols. Squares refer to the oxide bronzes, diamonds to spinels, and circles to other stoichiometric compounds. Filled symbols refer to compositions achieved by lithium insertion. A = VO_2, B = LiV_2O_4. Reproduced from Strobel (1996).[102]

Table 2: Phases of $Li_xV_2O_5$ and rough stoichiometric range.

x	0 – 0.1	0.2-.4	.85-.95	1.6-2.0	2.6-3.0
$Li_xV_2O_5$	α	ε	δ	γ	ω

Table 2 shows the range of stoichiometry values for the different $Li_xV_2O_5$ phases. The lithium insertion reaction into V_2O_5 is topotactic.[103] *Ab initio* studies point to the lithium being fully ionized, with the charge transferred to the transition metal centers and partially to oxygen.[104] The first two chemical reactions can be described by the following equations:

$$V_2O_5 + \tfrac{1}{2}Li^+ + \tfrac{1}{2}e^- \Leftrightarrow Li_{0.5}V_2O_5 \quad (3.4V) \qquad (17)$$

$$Li_{0.5}V_2O_5 + \tfrac{1}{2}Li^+ + \tfrac{1}{2}e^- \Leftrightarrow LiV_2O_5 \quad (3.2V) \qquad (18)$$

Equation (17) refers to the transformation from α to ε while equation (18) refers to the transformation from ε to δ. The phase transformation process of V_2O_5 upon lithium insertion has been described in detail elsewhere and is only summarized here.[31, 83, 98, 104, 105] In general, α-$Li_xV_2O_5$ ($0 \leq x \leq 0.13$) remains isostructural with the parent phase V_2O_5 during the initial intercalation.[98]

The positions of the lithium ions have been modeled only recently.[104] Generally, it is understood that lithium ions intercalate between the layers into interstitial sites. Atomistic simulation methods have identified several low energy sites along the *b* direction channel (see Figure 11). These positions fall about halfway along the *a* axis of the unit cell, ~ 0.4 along the *c* axis (in fractions of the unit cell distance), and vary between 0 to 0.5 along the *b* axis. Figure 14 displays the location of the low energy sites for lithium.

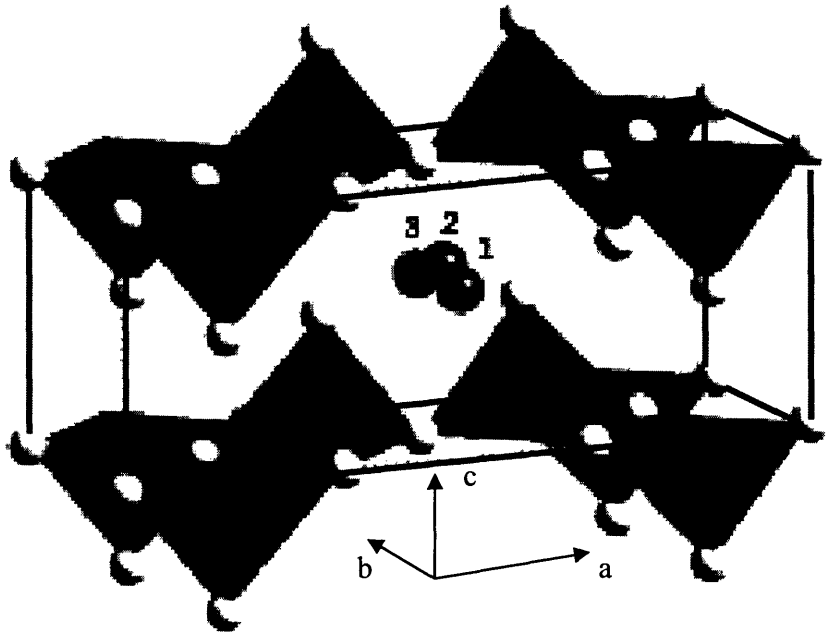

Figure 14: Unit cell of V_2O_5 showing low energy sites for Li^+. Light circles denote oxygen, dark circles denote lithium. Square pyramids denote vanadium coordination with oxygen. Reproduced from Brainwaite (1999).[104]

With further lithium insertion ($0.13 \leq x \leq 0.33$), the ε phase forms at the expense of the α phase. Diffraction patterns taken in this lab confirm the coexistence of the two phases on this composition intervals and give evidence of the phase transformation proceeding via nucleation and growth rather than by spinodal decomposition. The ε phase exists between $0.33 \leq x \leq 0.64$ and can be described by the Pmmn (#59) space group with lattice parameters of a = 11.3552Å, b = 3.5732 Å, and c = 4.6548Å. [106] The insertion of lithium causes an increase in the layer spacing as measured by c. The vanadium atoms continue to exist in a square pyramid coordination with oxygen. At x = 0.5, vanadium is equally split between $[V^{4+}]$ and $[V^{5+}]$ valency, so that both $[V^{5+}O_5]$ and $[V^{4+}O_5]$ coexist with the former being the smaller of the two pyramids. The decrease in a_o results in a puckering effect described by a "puckering" angle, μ, between V-O_v and the c-axis. This change in angle is shown in Figure 15. In the ε phase, $\mu = 7.1°$ and increases to 11.3° upon transformation to the δ phase. The lithium in the ε phase is coordinated to the oxygen in a bicapped triangular prism, CN 6+2.[106]

In the δ phase, lithium-oxygen electrostatic interactions lead to the shift of one oxygen atom, resulting in vanadium being surrounded by a triangular bipyramid of oxygen atoms.[107] The lithiums by contrast are surrounded in a bicapped tetrahedron oxygen environment, with CN = 4+2. A shift of alternating planes along the [010] in the Pmmn coordinate system occurs at x-values exceeding 0.64.[98] The shift corresponds to roughly ~ 1.8Å. The series of phase transformations is shown in Figure 16. The images were created using the software package Mercury (Cambridge Crystallographic Data Centre, Cambridge, UK).

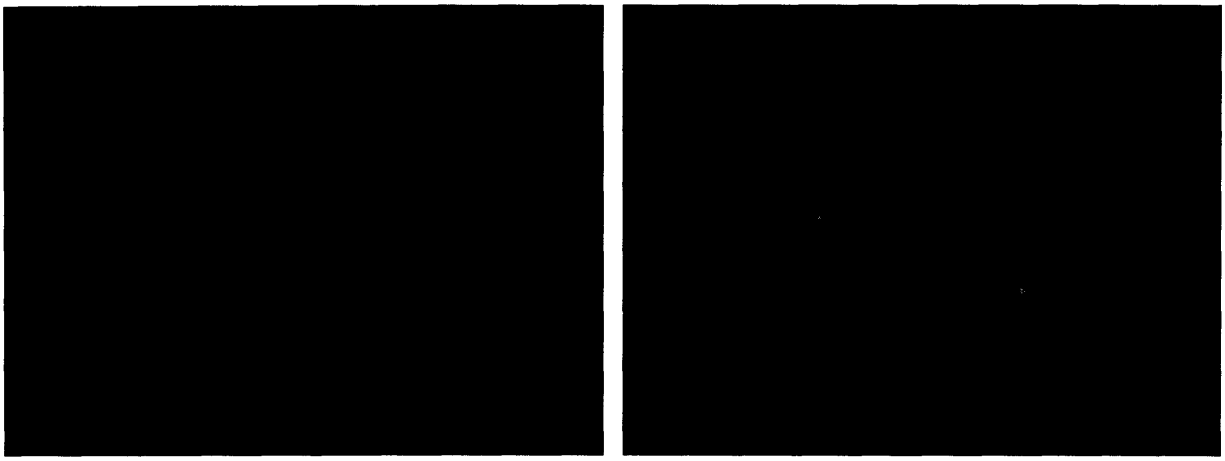

Figure 15: Distortion of the layering showing the puckering angle resulting from an alpha to epsilon transformation.

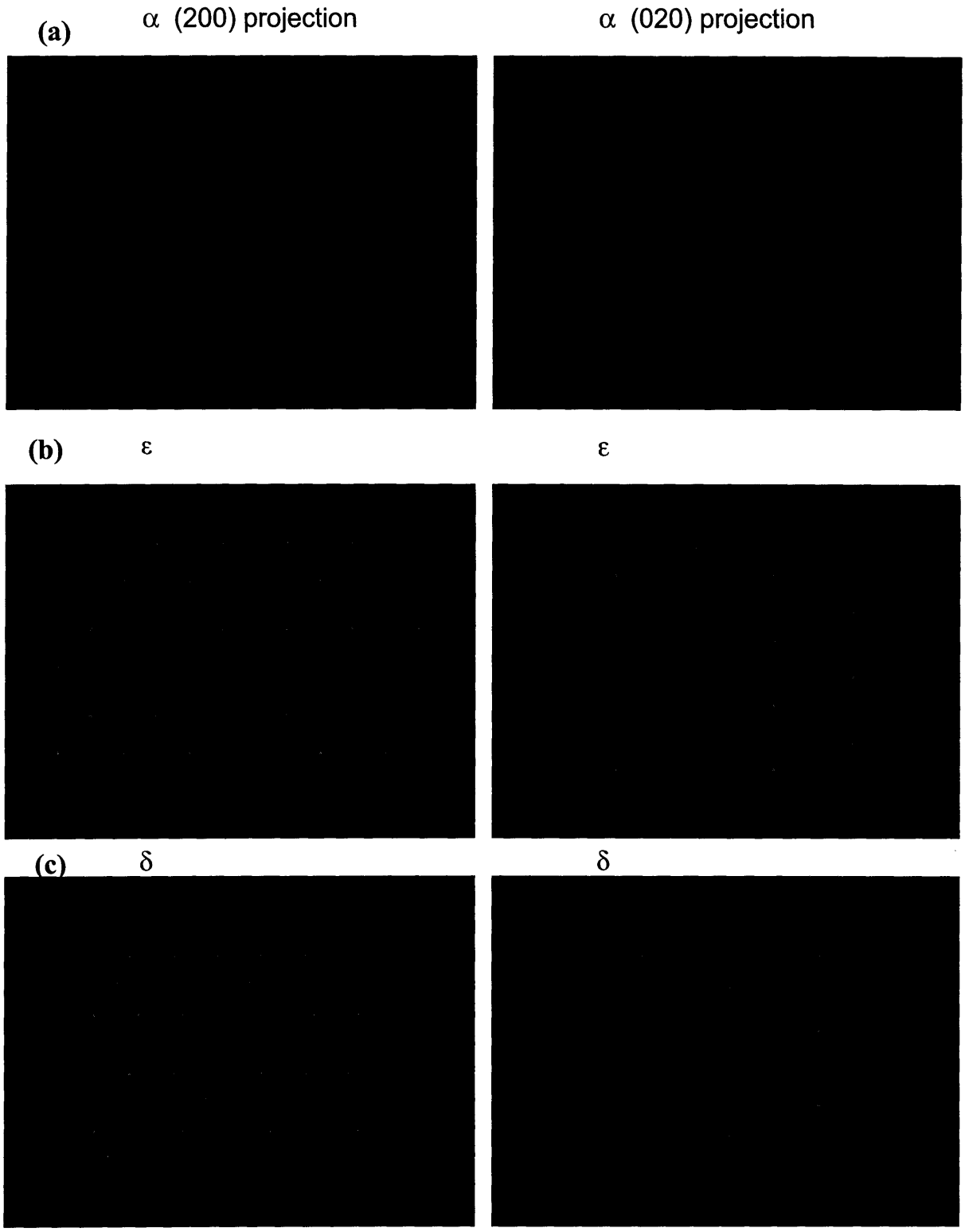

Figure 16: $Li_xV_2O_5$ phases showing (a) alpha, (b) epsilon, (c) delta. Arrows denote the glide direction for the layer.

Microstructure

Film morphology, including grain size and distribution, shape, orientation, and crystallinity, can vary as a function of the deposition method, deposition parameters, choice of substrate, and post-deposition heat treatment.[21-23] In this section, the deposition parameters and resulting microstructure are considered. The effects of heating rate during annealing are shown to also significantly affect microstructure, grain size, and orientation.

In general, thin film V_2O_5 cathodes were prepared using several sputtering approaches, including RF sputtering of both V_2O_5 targets and vanadium metal targets in a reactive environment. The microstructure was found to be highly sensitive to sputtering temperature, pressures, and substrate. Adhesion of V_2O_5 to such substrates as silicon or glass was also found to be a problem without the addition of an interlayer, such as titanium or aluminum. However, these layers were also found to be vulnerable to adhesion problems under long term exposure to non-aqueous liquid electrolytes.

Films with ~ 100 nm wide V_2O_5 "fingers" or brushes were produced under conditions in which a large thermal gradient is present at the substrate surface. Figure 17 shows one such structure grown on a (100) Si substrate with an adhesion layer of Ti and Al metal sputtered on the surface. Each finger represents a single crystal of V_2O_5. In general, to obtain this type of structure heat was applied using quartz halogen lamps at the back of the substrate and maintaining the substrate temperature at ~ 350°C. A V_2O_5 target was used and RF sputtered under reactive conditions (3 vol% O_2), a power of 300 W (~6.6 W/cm^2), and chamber pressures of 7-10 mTorr.

In contrast, Figure 18 displays a platelet-like V_2O_5 microstructure growing from an underlayer of ~ 100 nm of elongated grains of ~ 100-300 nm. Reactive DC sputtering of a vanadium metal target (380 W) was generally used to obtain this microstructure. A high concentration of oxygen (10% volume) was used in an argon atmosphere (8.3 mTorr) to oxidize the vanadium. Temperatures were moderate with the substrate kept at ~ 220°C to promote reaction between vanadium and oxygen and subsequent crystallization. Figure 19 displays films made by RF sputtering a V_2O_5 target (300 W) onto an ITO substrate with post-annealing at 400°C (left image) and heating at ~ 250°C during sputtering (right). Heating during sputtering promotes greater surface roughness and a more porous microstructure.

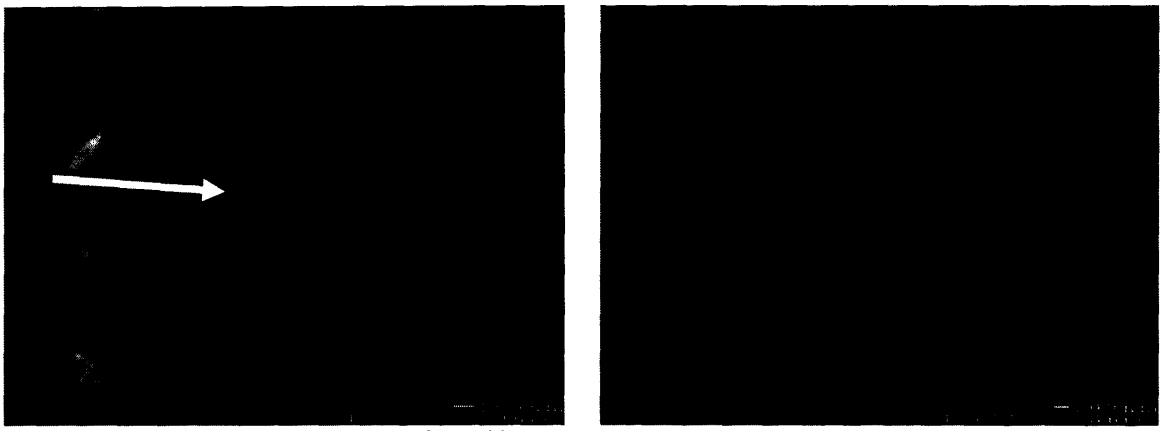

Figure 17: SEM micrographs of (Left) cross section, at 40kX and (Right) surface at 40kX showing nanobrush structure of V_2O_5. Arrow shows growth direction from substrate.

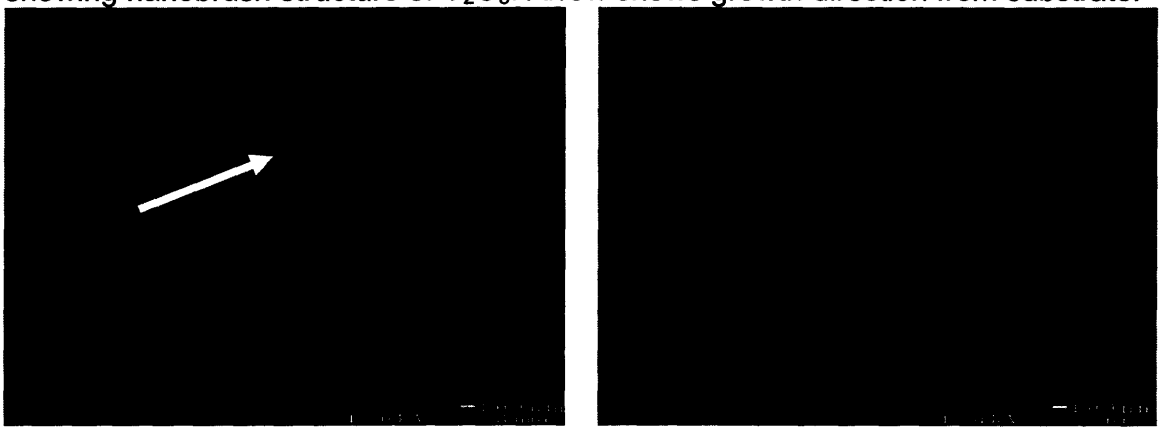

Figure 18: SEM micrographs of (Left) cross section, at 40kX and (Right) surface at 40kX showing platlete type growth and a nanograined underlayer. Arrow shows growth direction.

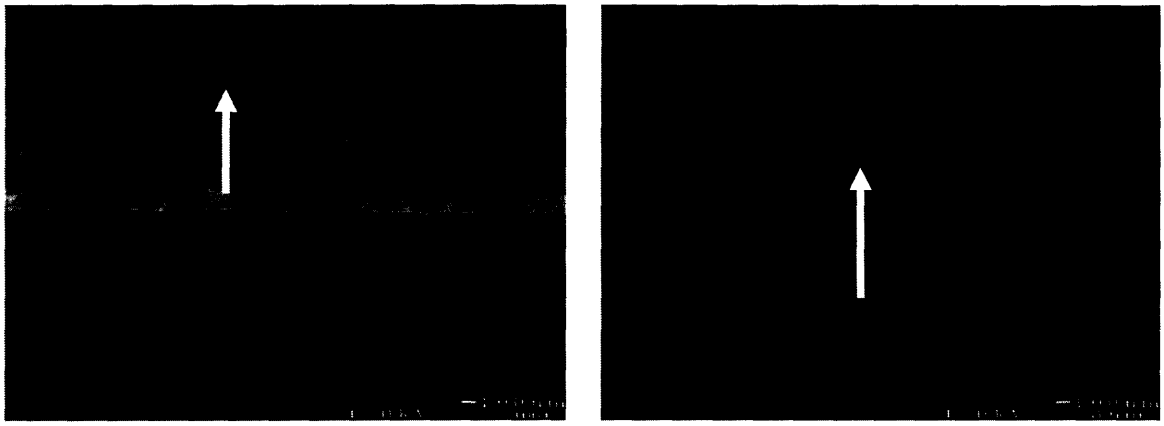

Figure 19: SEM micrographs (40kX) of V_2O_5 sputtered on ITO (~100 nm)/glass. (Left) No substrate heating during sputtering, post-annealing at 400°C; (Right) Sputtered with substrate heating at ~250°C. Arrows show growth direction.

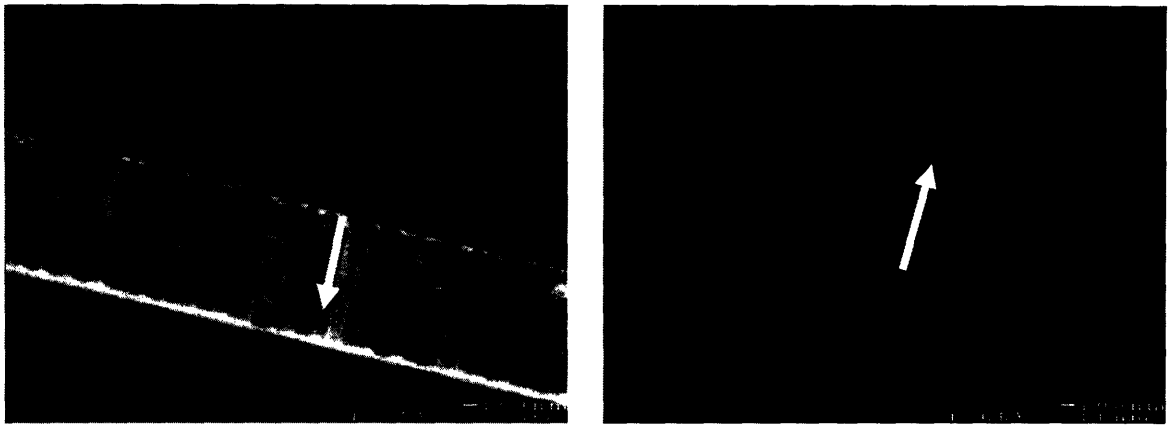

Figure 20: SEM micrographs (40kX) of V_2O_5 cross-sections sputtered at (Left) room temperature and (Right) subsequently annealed at 400°C. Arrows point to film growth direction.

Figure 20 displays the result of RF sputtering at room temperature onto a (100) Si substrate with thin (~10 nm) interlayers of Ti and Al. The V_2O_5 is observed to have well defined columnar type structure growing parallel to the substrate. The same sample, after heat treatment, is shown in Figure 20 on the right with the grains growing out of the columnar structure.

Annealing Effects

As shown earlier, a number of microstructures can be obtained by changing the three parameters: target, oxygen content, and sputtering temperature. Films that were sputtered at room temperature and subsequently annealed were found to be smooth and dense with variable grain sizes. The grain size and microstructure were controlled mainly via the heating ramp rate to the anneal temperature. Figure 21 shows samples undergoing heating ramp rates of 1, 5, and 70°C/min leading to very distinct microstructures.

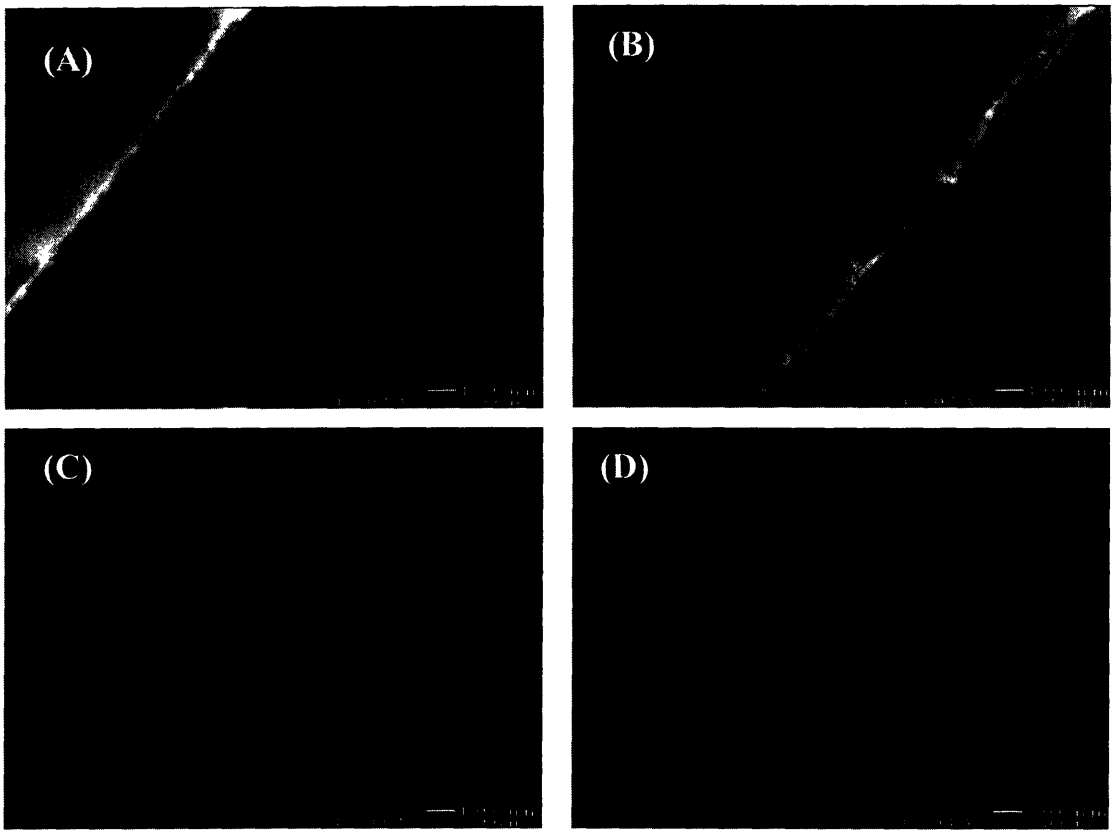

Figure 21: (a) FESEM cross sectional images of vanadium oxide as-sputtered (V2O5/Al/Ti/Si), (b) after heat treatment at 400°C in air with a 1°C/min ramp rate, (c) same, with a 5°C/min ramp rate, (d) same, with a 70°C/min ramp rate. (40 kX mag)

The plan view micrographs of an as-sputtered V_2O_5 surface versus an annealed surface from the same run are shown in Figure 22 below. The crystallization of the columnar growth is observed by the formation of grains that are somewhat elongated. AFM images also show evidence of faceting after crystallization (Figure 23).

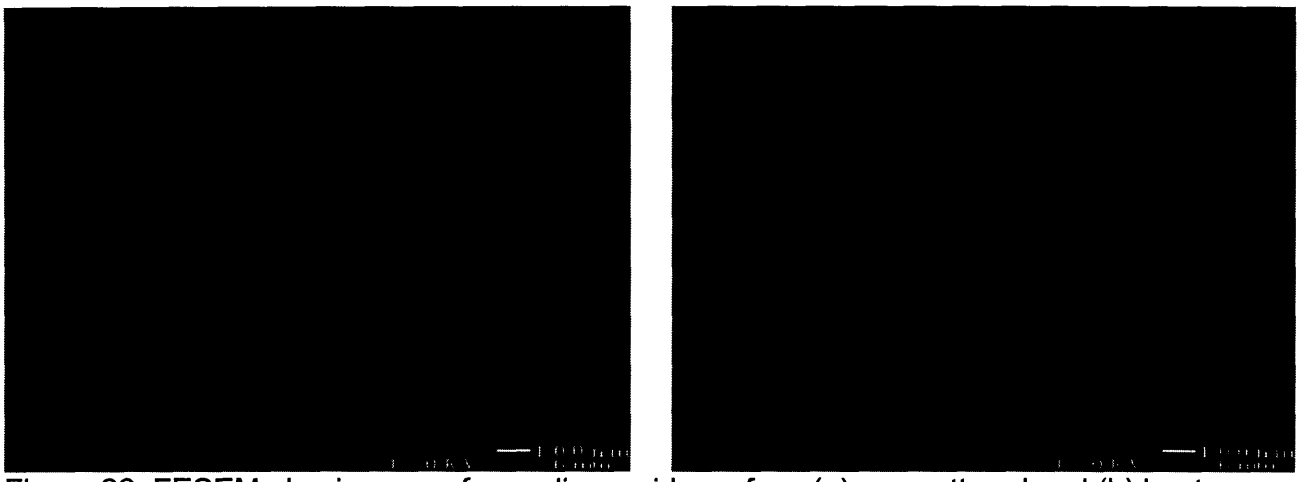

Figure 22: FESEM plan images of vanadium oxide surface (a) as sputtered and (b) heat treated at 400°C in air (40 kX mag) on Si/Ti/Al.

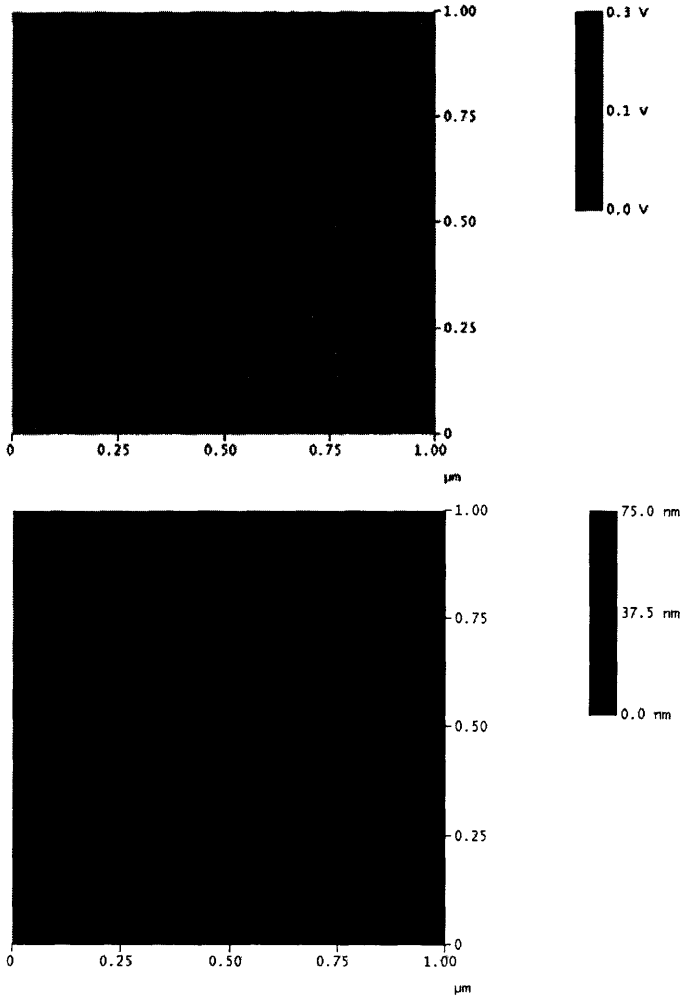

Figure 23: AFM (a) phase image and (b) height image of V2O5 film on Al/Ti/Si substrate that was annealed at 400°C in air.

In summary, films with smooth surfaces and dense microstructures can be grown by RF sputtering at room temperature. Higher temperature (> 300°C) sputtering was found to promote the growth of dendritic or platelet microstructures depending on whether the target was V_2O_5 or vanadium metal. At slightly lower temperatures (200-300°C), the film was rough due to preferential growth of crystallites within the film.

The annealing ramp rates were found to largely affect the grain size distribution, with larger sized grains growing at slower rates, and smaller grains growing at faster heating rates. Grain size distributions are explored more in depth in Chapter 6.

Surface Studies

A series of SEM studies of the surface of RF sputtered thin films at various stages of galvanostatic cycling was performed. The samples were sputtered from a 3 inch diameter target of vanadium oxide (V_2O_5) at 300 W in argon gas under an oxidizing environment onto both silicon and aluminum substrates. The substrate temperatures were heated between 350-400°C. Samples were approximately 280 nm thick, as measured by a surface profilometer (Tencor P-10). A wide-angle x-ray diffraction pattern was obtained of films on both substrates and revealed a V_2O_5 pattern with a slight (001) preferential orientation. Additional samples were similarly prepared and analyzed, albeit of different sputtered thicknesses.

2 cm^2 discs of the films were tested at 20 μA from 2.1-3.9V in a swagelok-type cell using liquid electrolyte (1 M $LiPF_6$ in EC:DMC, 1:1 Vol%, Merck) and a separator (Celgard 2300). Cells were cycled and subsequently stopped at various potentials. A final potentiostatic step was added to allow the cell time to equilibrate after which it was then disassembled and the electrode removed. The open circuit potentials were measured immediately before disassembly. In the glove box, cathodes were washed in PC followed by a mixture of anhydrous methanol and ethyl acetate. Samples were then dried under vacuum.

Samples were removed into air and analyzed using a JEOL 6320FV scanning electron microscope at 1 KV. As-sputtered samples of the V_2O_5 on aluminum foil appear as small crystallites densely aggregated, reminiscent of a microstructure dominated by the recrystallization and grain growth typical when bulk diffusion processes dominate during growth. Movchan and Demchishin (1969) named this as Zone 3 of their proposed Structure Zone Model.[23]

The morphology of the samples, as shown in Figure 24, consists of platelets stacked upon each other, oriented with the V_2O_5 (001) planes parallel to the substrate. The topography resembles that of fine-grained, metamorphic rock such as slate, cleaving easily as sheets along the [001] direction. The layering does not appear to be porous through the bulk, appearing to be virtually fully dense. At the surface are many elongated crystallites that are in fact, broken layers of these platelets, cleaved along the (001) planes parallel to the substrate. The morphology of the crystallites appears to be similar to bulk (~ mm) single crystals that were grown through chemical transport methods. Images of as-sputtered samples are shown below, along with slate for comparison.

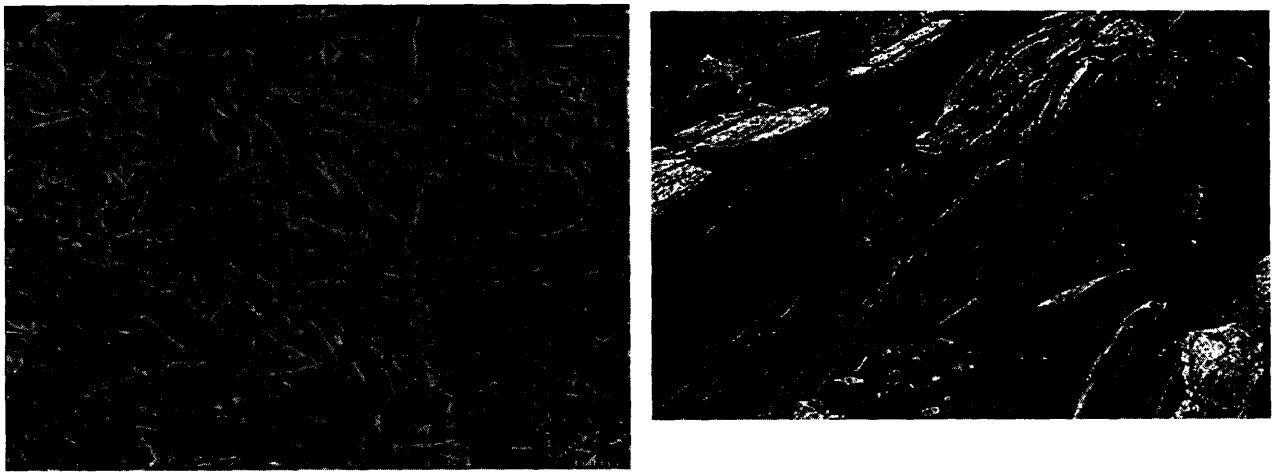

Figure 24: (Left) SEM of as-sputtered V_2O_5 (5 kX); (Right) Slate, showing platelet morphology.

V_2O_5 films grown on planar, slightly off-axis Si substrates <100> appear rough, consisting of small crystallites similar to those formed from a gas induced microstructure (Zone 2 of the aforementioned model). However, given that these samples were sputtered simultaneously, it is clear that the substrate has a strong influence on the microstructure as expected. Additionally, due to heating of the substrate's backside and local environment using halogen lamps, the actual surface temperature of the silicon substrate may be lower than that observed on the aluminum substrate due to the prior's lower thermal transport. Films that were sputtered in an oxidizing environment, albeit at room temperature, typically show the smoother surface topographies due to their amorphous structure and growth conditions. Similarly, semi-

crystalline, electron-beam assisted evaporation samples on aluminum of mixed-phase vanadium oxide show this smoother surface topography, as shown below in Figure 25.

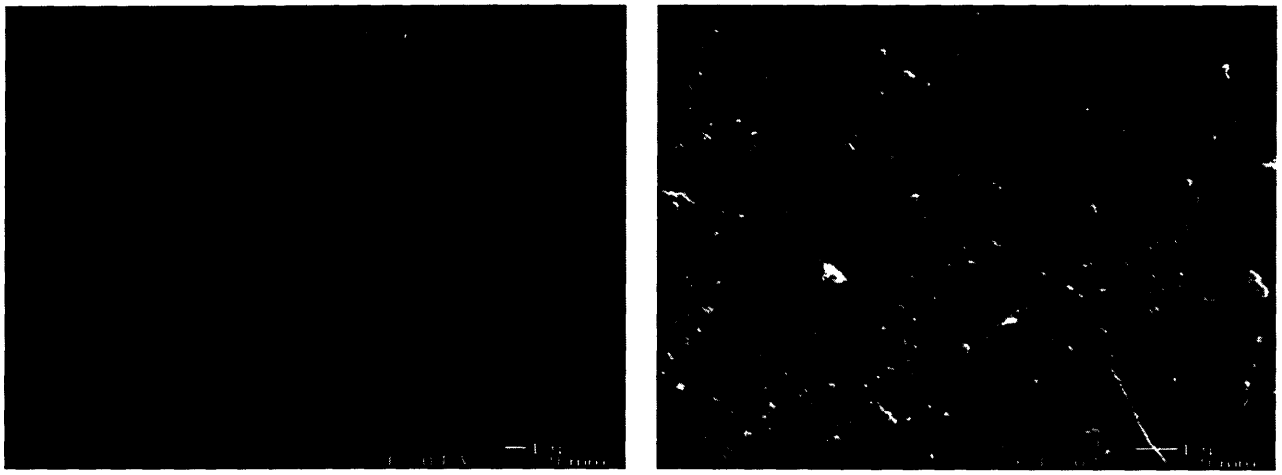

Figure 25: Left: SEM Image (5 kX) of an amorphous V2O5 film, sputtered under RF and reactive conditions; Right: SEM Image (x 10k) of e-beam assisted evaporation of vanadium oxide, Lincoln Labs, MIT.

The images of the oxide over the 1st discharge and charge cycle show a similar morphology to that of the virgin sample (Figure 26). The discharged sample, however, shows a less clearly defined surface interface, with a surface film appearing dendritic and covering the crystallites. These possibly consist of reduced species of the electrolyte with lithium salt, or a Li_xO_y compound as found in XPS studies of lithiated V_2O_5 thin films by Passerini *et al* (1997). [108, 109] . However, a study by Bullard and Smith (2002) on single crystal V_2O_5 surfaces show evidence of pitting of the (001) surface upon initial intercalation and removal of Li^+ within the α-V_2O_5 phase, potentially due to volume excursions with lithiation.[64] Here, greater amounts of lithium are inserted (i.e. to the δ phase) such that it is unclear whether these results show actual pitting and removal of material, SEI layer formation, Li_xO_y formation, or all of the above.

Throughout the sample, darker regions appear, perhaps due to variations in the surface environment (i.e. high lithium content) or regions where lithium ions are reduced to lithium neutral and first insert. Close inspection reveals that the darker regions do not appear to be lowered areas or due to pitting or removal of material via the electrolyte, although this was not ascertained with *in situ* AFM. Images at higher magnification of the lithiated samples show a different surface with either roughening or formation of species on the surface. Subsequent

pictures of the delithiated sample after the cell is discharged and charged reveal a microstructure close to that of the pre-cycled sample, suggesting that the surface "roughening" may not be due to an SEI, which would be expected to remain throughout charging and discharging once formed. Finally, the films were exposed to air upon transfer from the glove box to SEM, so that a lithiated surface (in contrast to the unlithiated, charged sample) might be expected to react with the atmosphere to a greater extent.

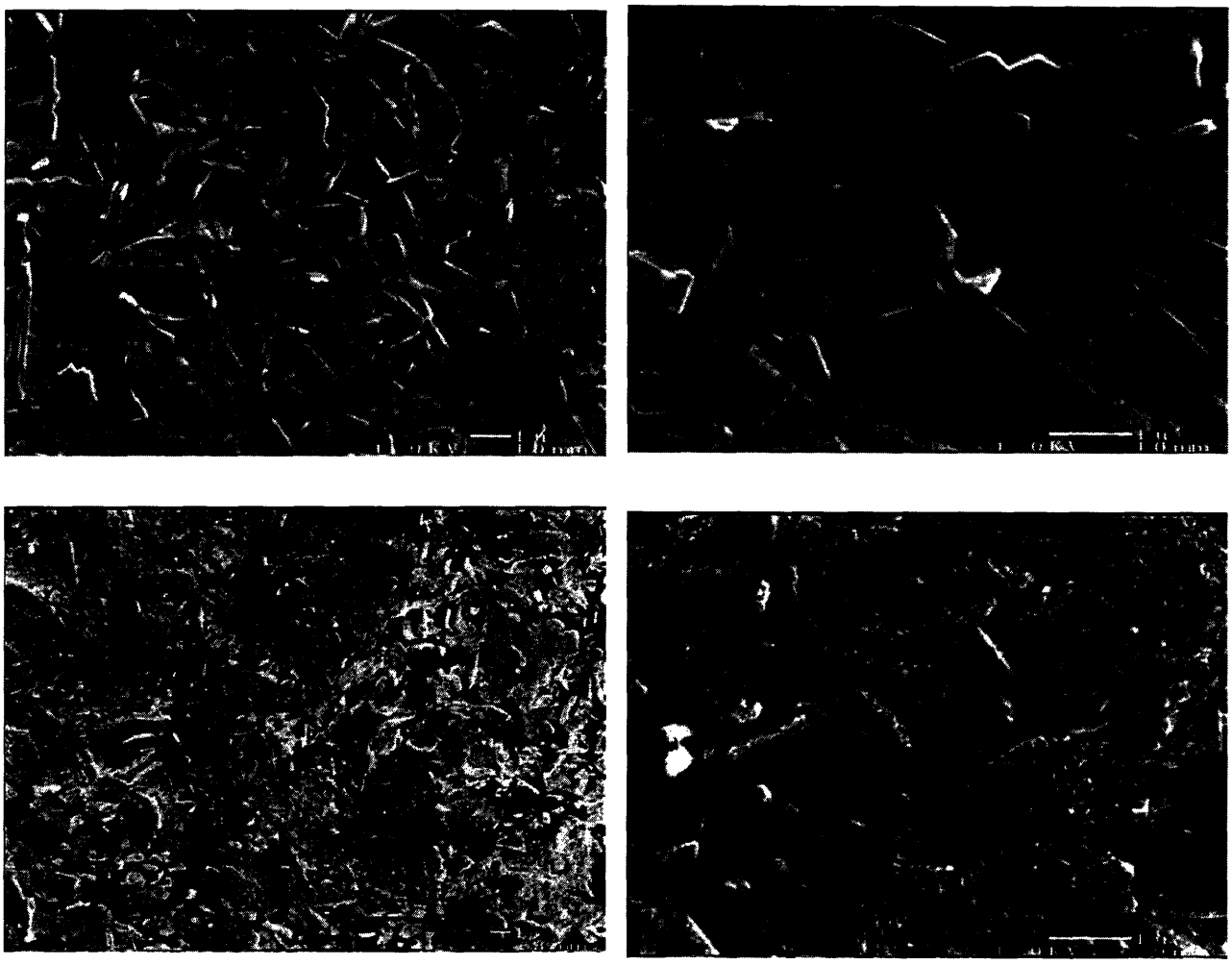

Figure 26: Top: SEM images of Delithiated V_2O_5 sample at 5 kX and x 2 kX mag (1st charge). Bottom: SEM images of Lithiated V_2O_5 sample at 5kX and x 20kX mag (1st discharge).

Subsequent cycling appears to fracture the surface even more, leading to a "random matches" type topography after extended cycling as shown below in Figure 27. After cycling 10 times and in a lithiated condition LiV_2O_5 and delithiated condition ($Li_xV_2O_5$, where $x < 0.1$), the surface of densely packed platelets is replaced with highly oriented dendritic type morphology, assumed to be crystallites broken up from the platelets, with dimensions on the order of 100-200 nm in width and 500-800 nm in length. These crystallites appear to be stacked on top of each other, resembling a randomly distributed pile of matches. Delithiated vanadium oxide shows the clear crystallite surfaces while the lithiated surfaces show evidence of roughening due to a changed surface. Additionally, crystallites appear to have been pulverized to some extent through the lithiation and delithiation steps. This process of reactant materials fracturing into smaller pieces and losing electronic contact is known as decrepitation[††] and is commonly observed for lithium alloys.[110]

[††] U.S. Bureau of Mines *Dictionary of Mining, Mineral, and Related Terms*, CD-ROM 1996: decrepitation is (a) method of differential disintegration of closely sized mineral, part of which explodes and is separable by finer screening or (b) the breaking up with a crackling noise of mineral substances upon exposure to heat, as when rock salt is thrown into fire. The terminology has been co-opted by the battery field to describe the crumbling of electrode materials.

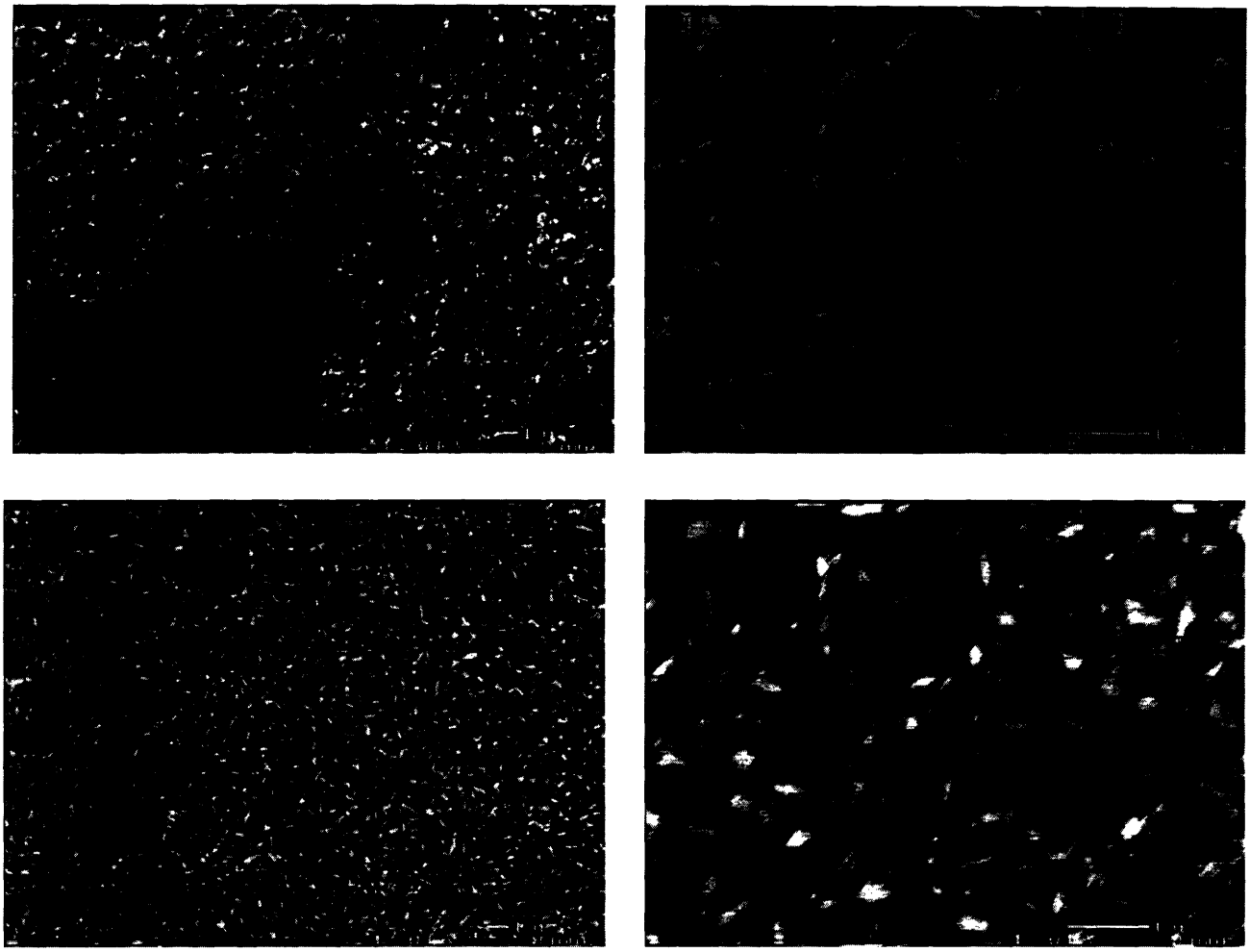

Figure 27: Top: SEM Images of V_2O_5 RF Sputtered, Cycled 10x, Lithiated to ~ 2.1V. (left 5 kX, right 20 kX). Bottom, same sample delithiated to ~ 3.9V. (left 5 kX, right 20 kX).

In summary, a platelet morphology is observed to be vulnerable to decrepitation, an observation that has been made in powder-based cathodes and lithium alloys. It is suggested that these platelet morphologies are unsuitable to serve as cathodes and lead to poor cycling life. Interestingly, under the SEM, the lithiated surfaces of the films were observed to be qualitatively different from the delithiated film surface. It is suspected that either formation of Li_xO_y or roughening due to the insertion process may be the cause of these differences.

In Situ AFM:

In situ AFM results was used to evaluate the possibility of surface changes during the phase transformation process. It was hypothesized that the thin film grains might expand with lithiation and phase transformation, such that the differences would be detectable using *in situ* AFM during the discharge process. The cell configuration was described in Chapter 3. A V_2O_5 film on an ITO/glass substrate was used with a circular geometric area of ~ 1.76 cm^2 exposed to the liquid electrolyte. A discharge current of 36 μA was used, equivalent to ~ 18 uA/cm^2 and a 1C discharge rate (i.e. 1 hour discharge). Thirty four continuous scans were performed in a 500 nm by 500 nm area from the open circuit voltage of 3.55V down to 2.5V vs. lithium. A discharge profile showing where each scan began is shown in Figure 28. A series of scans taken at various stages of discharge (potential shown) is shown in Figure 29.

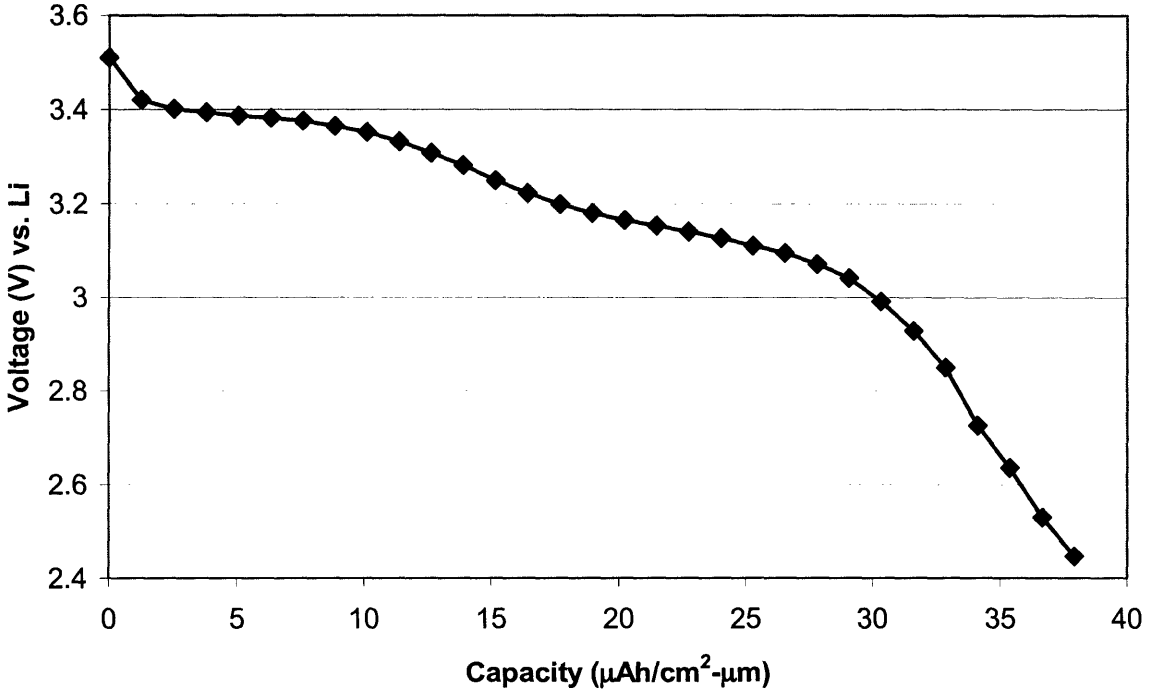

Figure 28: Voltage profile of cathode undergoing discharge with *in situ* AFM. Each point represents the beginning of a new scan. The description in the upper right corner describes the heat treatment of the cathode. The area ~ 1.76 cm^2, each point represents one AFM scan. Heat treatment ~ 0.5 °C/min, 300°C, 24 hour hold.

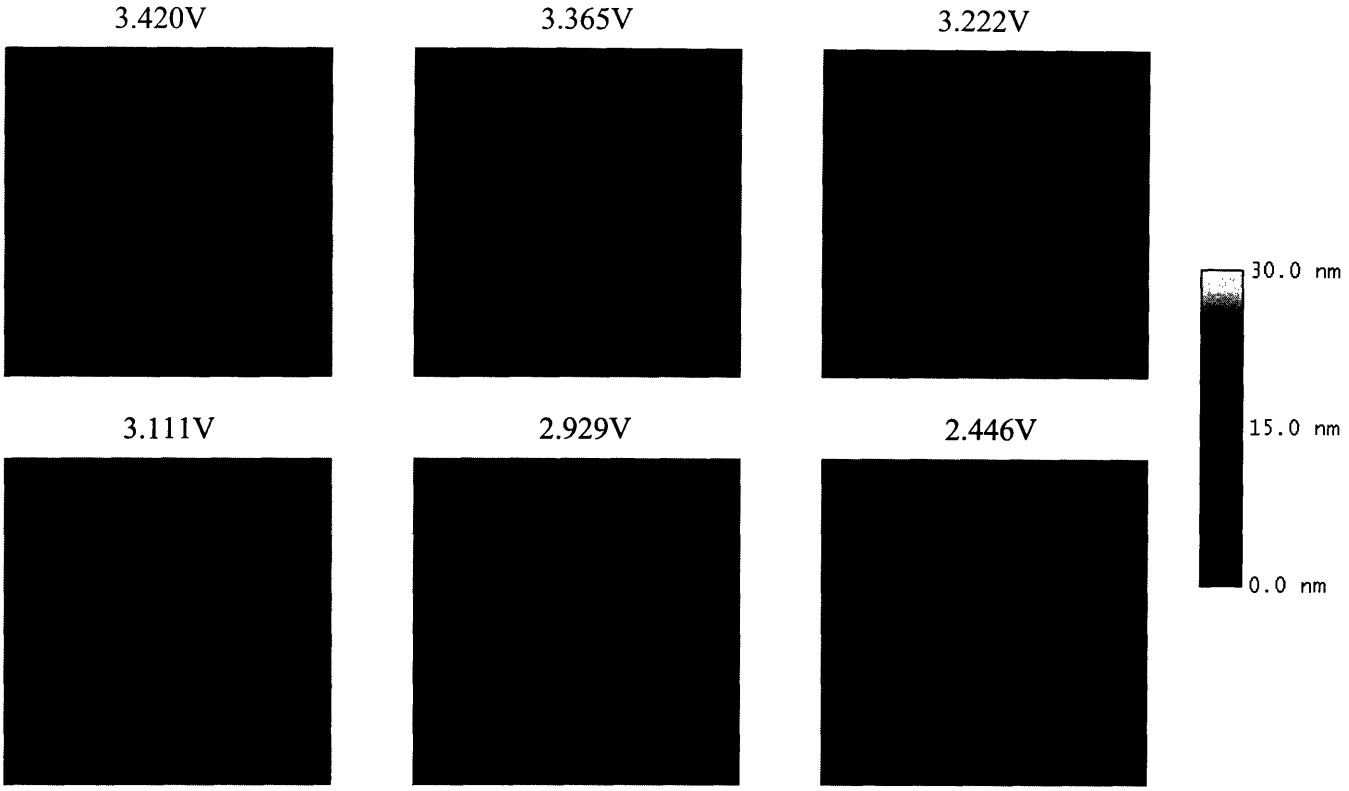

Figure 29: Partial series of *in situ* AFM scans of $Li_xV_2O_5$ surface with discharge. Each figure represents a 500 nm by 500 nm area. Starting potential shown. Height bar shown on right.

The samples show the same film region through the scans. Grains were observed to be several hundred nanometers in size. Unfortunately, substantial drift occurred during the scans, such that the image location shifts during the process of scanning. Unlike studies of single crystals, where one particular feature can be imaged decisively with the position remaining constant, a reference point was difficult to compare because of image drift in the vertical and horizontal directions *as well as* rotational drift. Hence, some of the images do not show consistent feature locations, making it difficult to accurately measure on the scale of several nanometers – the range in which volumetric changes might be expected to appear. Initial measurements based on sectioning of the AFM data did not show significant differences with lithiation (as measured by the movement of specific features) at the surface.

Electronic Conductivity

The electrical conductivity of V_2O_5 films was measured by impedance spectroscopy. Conductivity through the film, perpendicular to the substrate, was measured using a simple two electrode sandwich of the film with the ITO/glass substrate as one electrode and sputtered aluminum metal on the opposite side (with Ag conductive paint applied). The areas were masked using a washer with a 6 mm exposed area. An impedance spectrum of a representative film is shown below (the film was annealed to 500°C for 4 hours at a 1°C/min. ramp rate). A simple circuit model with a capacitor and resistor in parallel allowed both the capacitance of the film and resistance of the film to be measured. Taking into account the geometry, the conductivity is simply calculated via:

$$\sigma_e = \frac{\ell}{RA} \qquad (19)$$

where ℓ is the film thickness, A is approximately the geometrical area, and R is the measured resistance, here the width of the semicircle. The resistance at the higher frequencies ($Z' \sim 100\Omega$) represents the cell and ITO resistance. The conductivity of the film is $\sim 1.2 \times 10^{-6}$ S/cm, similar to values reported in literature. Measurements of amorphous films resulted in lower electrical conductivities, on the order of $\sim 1.6 \times 10^{-7}$ S/cm. Comparison with the Al foil substrate is also of interest. The conductivity of a comparable film prepared in a similar fashion on an Al foil substrate was measured to be 1.8×10^{-6} S/cm, roughly the same value as samples mounted on ITO given the uncertainty in area and thickness. The same V_2O_5/Al foil film, non-heat treated and XRD amorphous, measured conductivities on the order of 2.6×10^{-7} S/cm, or almost an order of magnitude lower.

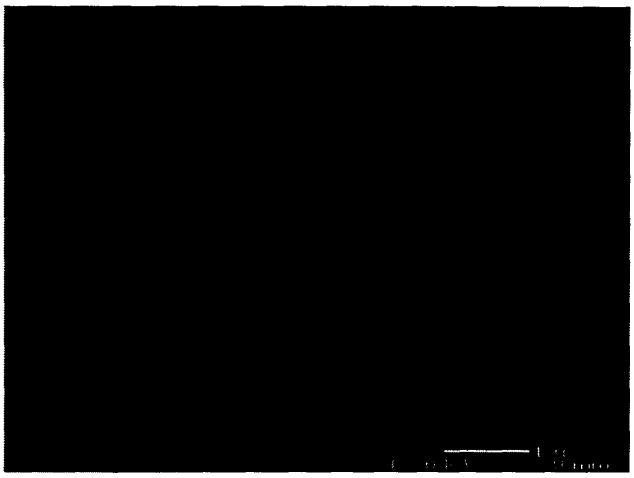

Figure 30: SEM Image of V_2O_5 film on ITO/Glass

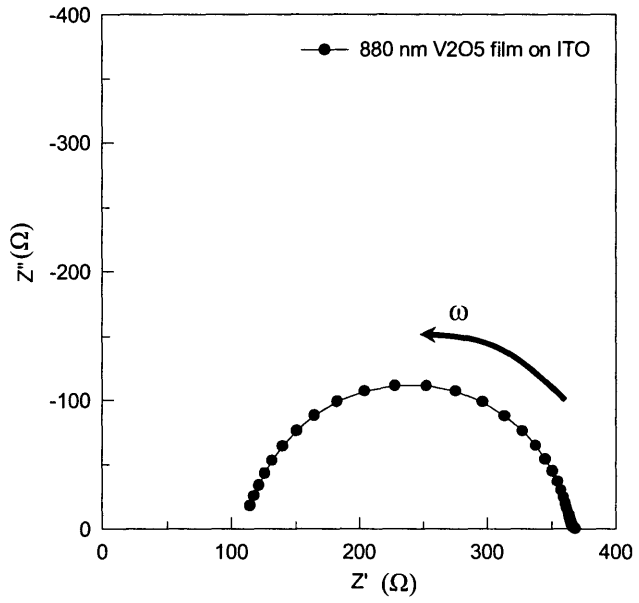

Figure 31: Impedance spectrum taken at RT of a V_2O_5/ITO film annealed at 500°C.

The variation of electronic conductivity with lithium content ($Li_xV_2O_5$) was determined using interdigitated electrode arrays (IDA). IDAs consisted of 25 platinum digit pairs of 0.5 μm width, 0.1 μm height, and 3 mm length, spaced 0.5 μm apart (Abtech Scientific, Inc). The Zaretsky cell constant for the IDA was 0.13 cm. Sputtering was performed on the arrays only, with other areas masked. The impedance of the as deposited, sputtered film (~ 200 nm) was measured (i.e. amorphous). The conductivity measured 1.68 x 10^{-6} S/cm, higher than the values obtained by the parallel plate method. However, it is known that different methods of measuring conductivities, together with anisotropic electrical properties in V_2O_5, can lead to differences in conductivity. Subsequent heat treatments on samples however to measure the crystalline properties proved unsuccessful due to the temperature constraints of the IDA.

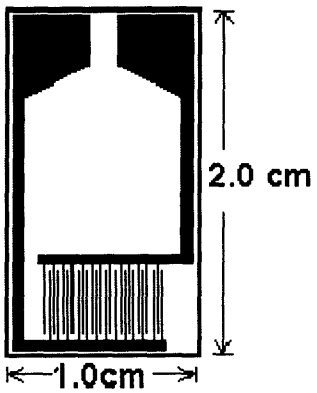

Figure 32: Schematic showing the interdigitated electrode array.

Summary

The microstructure of V_2O_5 thin film cathodes was found to be particularly sensitive to sputtering temperature, target, and the choice of whether reactive DC or RF sputtering was used. Films that were RF sputtered from a V_2O_5 target in a reactive environment at room temperature formed the most homogeneous films with the least roughness. It was also found that the subsequent annealing treatments of these amorphous films determined the grain size distributions and morphologies. The heating ramp rate was the most critical parameter in the anneal step in controlling the grain size distribution, more so than time and temperature. The effects of heating ramp rate in the battery literature have not been reported thus far.

Surface analysis of films with a platelet microstructure, post discharge, showed the appearance of dendritic, SEI surface layers. These layers are subsequently removed upon charging, as evident from SEM imaging. Subsequent cycling causes fracture in the films analogous to decrepitation found in lithium alloys. Hence, while the platelet morphologies provide high surface area films, these microstructures are unsuitable for extended cycling.

The electronic conductivity of the films that were uniform and smooth matched well with those reported in literature. Interestingly, the amorphous structure measured lowered conductivity values (roughly an order of magnitude) than their crystalline counterparts.

Chapter 5: Phase Transformation

In this chapter, the effects of thin film microstructure on capacity-rate performance were investigated in rf-sputtered V_2O_5 films. An evaluation of diffusion coefficients and potential transient response curves is performed to understand performance differences between samples. XRD and TEM analysis are also employed to understand the phase transformation process. When compared to a coarse grained microstructure, a fine grained film microstructure is shown to have lower rate-capability due to kinetic bottlenecks encountered during phase transformation.

Chronopotentiometry

Comparisons of electrochemical performance were made between samples from the same sputtering run to ensure batch-to-batch variations were excluded. Differences in microstructure and crystallite orientation were obtained by varying only one parameter, heating ramp rate, during the post-anneal step. Figure 33 displays TEM cross-sectional images of as-sputtered, x-ray amorphous V_2O_5 thin films subsequently crystallized using a slow heating rate of 5°C/min (1a) and a faster heating rate of 70°C/min (1b). Both samples were held at a dwell temperature of 400°C for 90 minutes. All samples originated from the same sputtering run and are ~ 500 nm thick. The samples treated at a slower heating rate appear to be of a coarser microstructure in the sub-micrometer range (150-500 nm, herein c-VO). Samples treated at a faster heating rate have a finer grained microstructure with significantly smaller grains (50-150 nm, herein f-VO). A graph showing the grain size distribution is included in 1(c). The mean grain size for f-VO is 89 ± 30 nm and for c-VO is 235 ± 84 nm.

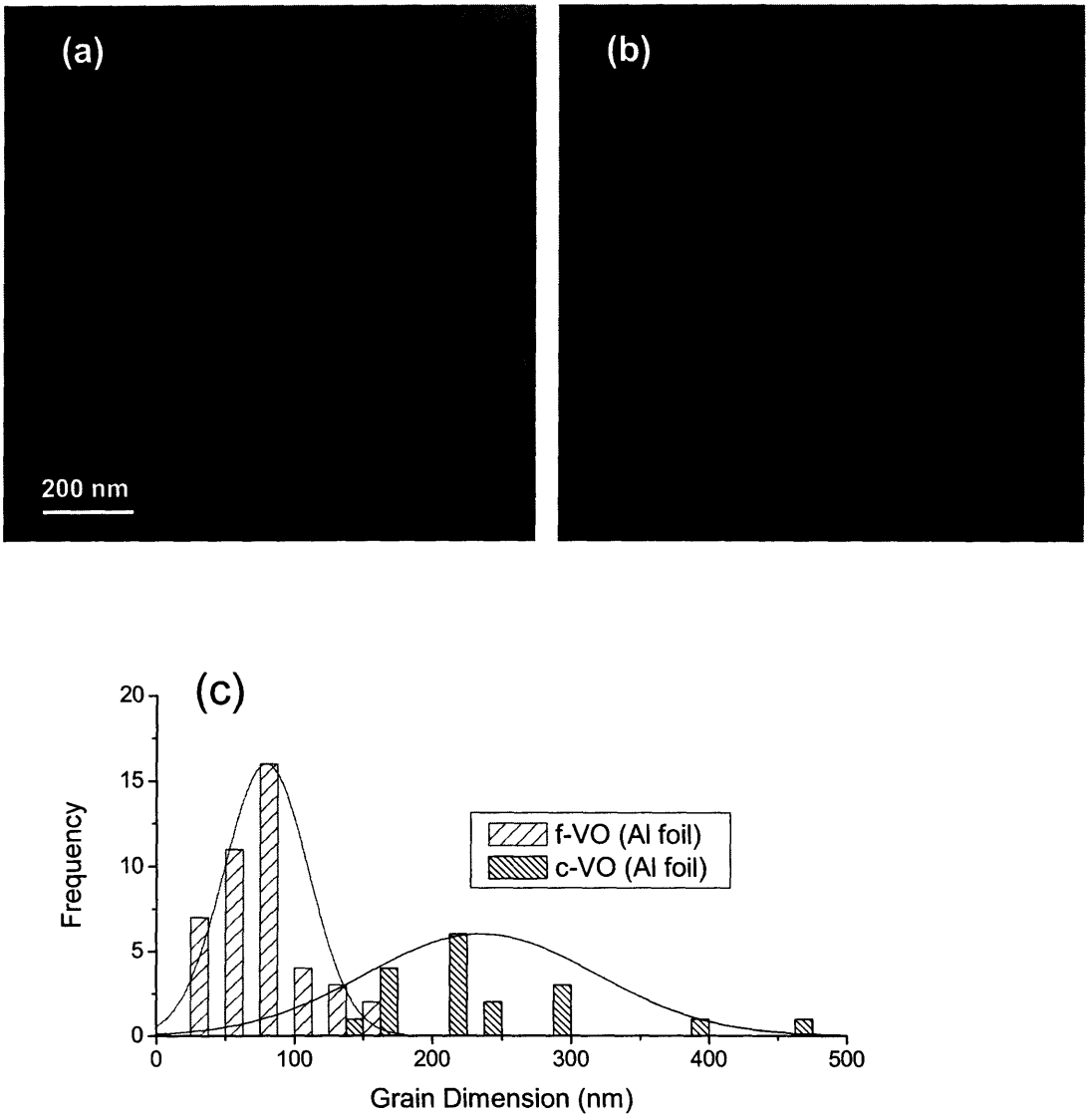

Figure 33: TEM micrographs of lithiated (a) c-VO and (b) f-VO (δ-phase $Li_xV_2O_5$ films, 3.08V versus Li). Film thickness ~ 500 nm. Figure 1(c) shows the grain size distribution of the films.

Figure 34 shows the capacity-rate performance of c-VO and f-VO. The potential range used (2.5 to 3.9V vs. Li) encompasses transitions through the α-$Li_xV_2O_5$ ($x \leq 0.1$), ε ($0.33 \leq x \leq 0.64$), and δ ($0.7 \leq x \leq 1$) phases.[98, 111] At 80% of the theoretical film density of 3.36 g/cm^3, x = 0.90 Li would correspond to a capacity of 35 μAh/μm-cm^2. Discharge capacities at a 1 μA/cm^2 current

rate yielded measured capacities of 35 ± 5 μAh/μm-cm^2 -- the expected theoretical capacity accounting for experimental error.

The rate performance of samples c-VO heated at a slower rate and having a coarser grained microstructure was dramatically improved over f-VO. The curve for c-VO is observed to asymptote at current rates approaching 200 μA/cm^2, while f-VO asymptotes near 20 μA/cm^2. Figure 35(a) and (b) show the galvanostatic discharge curves for c-VO and f-VO, respectively, at different current rates. At elevated current rates, the f-VO sample displays severe polarization as well as the disappearance of the discrete potential plateaus. The rapid reduction of capacity along with the loss of distinct potential plateaus can often be associated with slow mass transport.[31, 112]

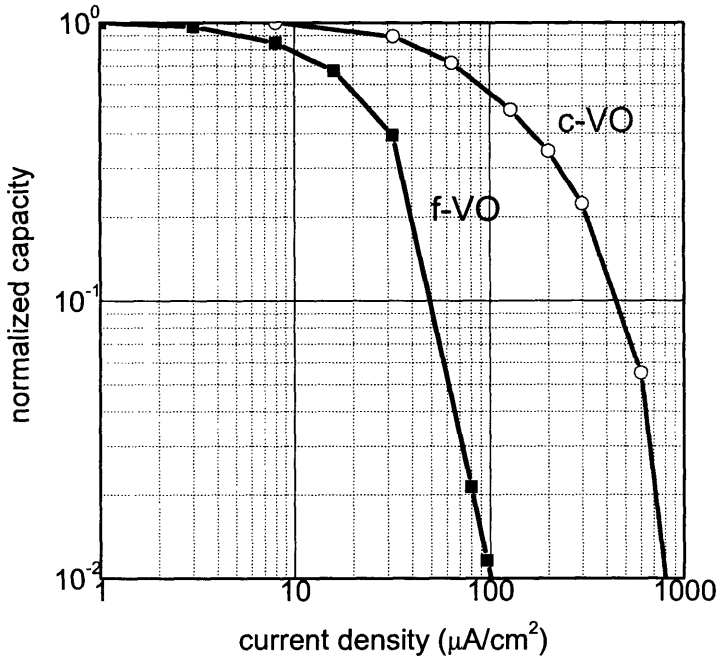

Figure 34: Normalized capacity-rate plot (log-log) of V_2O_5 thin film undergoing heating rate of (a) 5°C/min and (b) 70°C/min. The capacity obtained at 1 μA/cm^2 was normalized to unity.

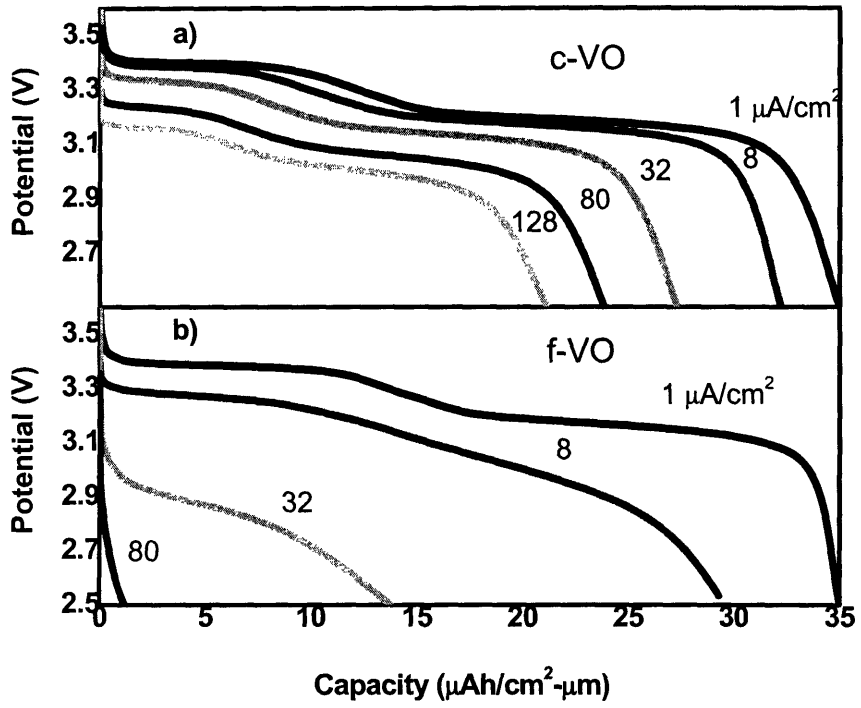

Figure 35: Discharge profiles of c-VO (5°C/min) and f-VO (70°C/min) for various current rates.

Classical nucleation theory suggests that a slower heating rate would lead to smaller local thermal fluctuations, leading to fewer nucleation sites, more stable growth, and larger overall grain sizes.[113, 114] As observed in the TEM micrographs (Figure 33), the finer grained samples (f-VO) contain greater volume of grain boundaries. The f-VO microstructure might be expected to enhance capacity-rate performance in thin films due to (1) enhanced diffusion along grain boundaries or (2) reduced diffusion distances within grains as the result of electrolyte permeation through film microcracks or micropores. However, the opposite result is observed. The reasons for these marked differences are discussed below.

Grain Orientation

XRD patterns of sample films are compared in Figure 36, with all peaks (marked) identified as V_2O_5 (PDF #41-1426) or from the aluminum substrate (unmarked). The space group

describing δ-V_2O_5 is Pmmn(59) with reported lattice parameters of a_o = 11.5160, b_o = 3.5656, c_o = 4.3727 Å.[115] The percentage of grains oriented with the (hkl) plane parallel to the substrate can be estimated by taking the ratio of the individual (hkl) peak area relative to the total peak areas. The resulting relative orientations are given in Table 3. Faster heating rates resulted in evolution of the (001) peak, denoting a greater percentage of grains with the [001] direction normal to the substrate. Differences in the relative orientations between f-VO and c-VO were observed for the (200), (001), and (110) peaks. The [001] represents a diffusion direction perpendicular to the V-O layers, while the [200], [020], and [110] directions represent faster diffusion pathways between the layers. It is notable that moving to slow heating rates (c-VO) resulted in suppression of the [001] oriented grains and an increase in the number of [110] oriented grains. The f-VO, with a larger amount of [001] grains, would be expected to have slower initial intercalation of Li^+ ions into the film.

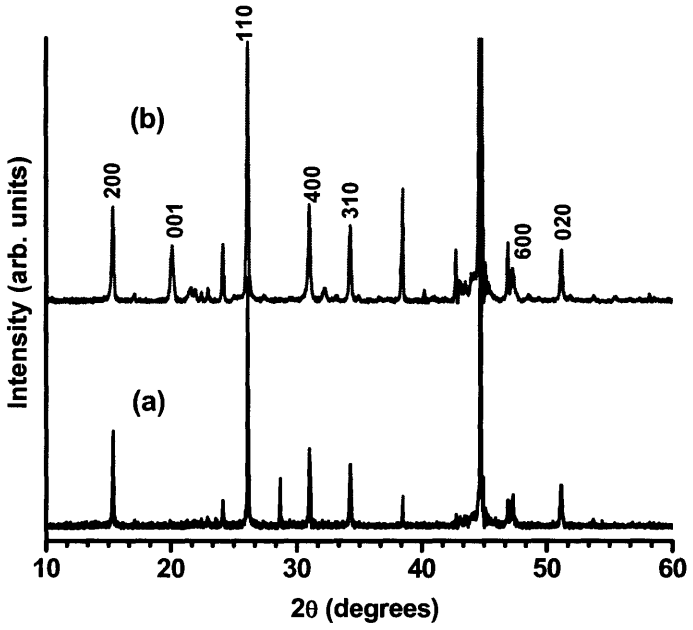

Figure 36: XRD Pattern of (a) c-VO and (b) f-VO after heat treatments. (110) peak intensities were normalized for pattern comparison.

Table 3: Percent grain orientations based on XRD peak intensities, c-VO and f-VO.

	{200}	(001)	(110)	(310)	(020)
C-VO, HT1	19.3%	2.2%	47.0%	17.7%	13.8%
F-VO, HT2	17.5%	19.9%	39.0%	12.4%	11.3%

Intermittent Titration

GITT was used to calculate the diffusion coefficient as a function of lithiation, following the approach first proposed by Weppner and Huggins.[82] A 2.5 μA pulse for τ = 12 min was applied to cells, followed by a relaxation until the potential change was less than 5 mV over 1000 s. Under diffusion-controlled conditions, if $\tau << L^2 / \widetilde{D}$, where L is approximated as the thickness of the film, then the chemical diffusion coefficient can be represented by:[82]

$$\widetilde{D}_{GITT} = \frac{4}{\pi}\left(\frac{V_M I_o}{SFz_i}\right)^2 \left[\frac{\left(\frac{dE_o}{d\delta}\right)}{\left(\frac{dE_p}{d\sqrt{t}}\right)}\right]^2 \qquad (20)$$

Here, V_M is the molar volume, S the effective area, F is Faraday's constant, z_i the moles of lithium involved in the reaction, I_o the current pulse magnitude, $dE_o/d\delta$ the slope of the steady-state voltage curve with lithium concentration, and $dE_p / d\sqrt{t}$ the slope of the transient voltage curve with the square root of time. A linear regression was performed to obtain the slope $dE_p / d\sqrt{t}$ for values of τ from 25 – 7200 s to ensure the initial IR drop was not included. Thus, the polarization results are attributed to the effects of mass transport within the film.

$\widetilde{D}_{GITT}$ values, derived from Fick's law, implicitly assume a single-phase system. Consequently, for two-phase regions $\widetilde{D}_{GITT}$ values are undefined. The single-phase regions are delineated in Figure 37(a) and (b) showing the steady-state voltage curve and the $\widetilde{D}_{GITT}$ values. Note that the two phase regions are shown only for completeness.

Figure 37: GITT derived (a) steady-state voltage, (b) $\tilde{D}_{GITT}$, (c) $(dE_o/d\delta)^2$, and (d) $(dE_p/d\sqrt{t})^2$. The vertical lines delineate the α, ε, δ regions. Values for $\tilde{D}_{GITT}$ are undefined in the two-phase regions.

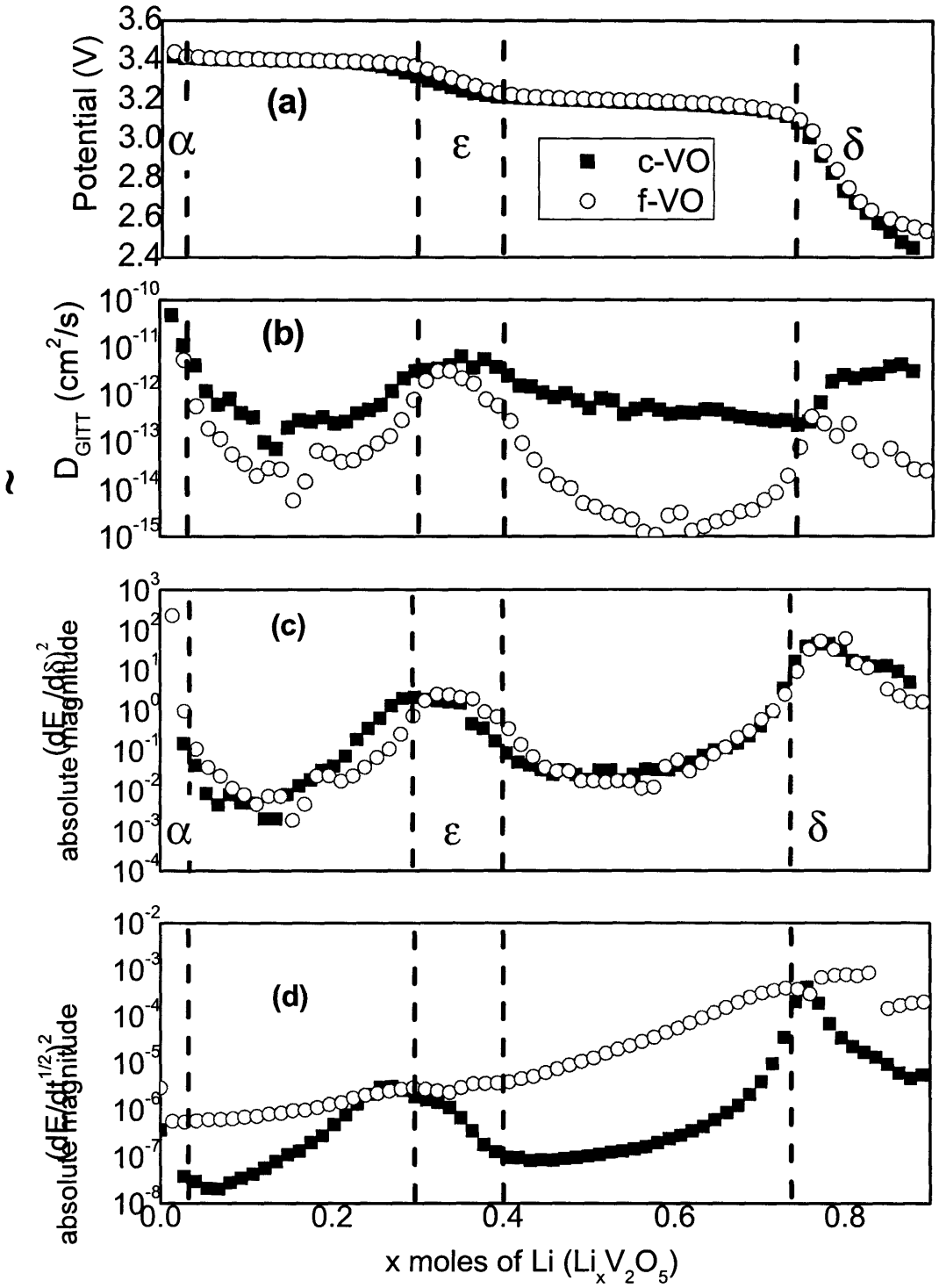

The convergence in $\widetilde{D}_{GITT}$ values over the α and ε single phases was unexpected given the poor performance of f-VO relative to c-VO. To better understand the significance of $\widetilde{D}_{GITT}$ values, a sensitivity analysis was performed upon eqn. (20). The analysis applies a reasonable range of values to evaluate whether the numerator ($n = dE_o/d\delta$) or denominator ($d = dE_p / d\sqrt{t}$) dominates in eqn (20). Table 4 displays the range of values applied. The analysis reveals that $\widetilde{D}_{GITT}$ will be dominated in most cases by $dE_o/d\delta$ by more than an order of magnitude. This is apparent because over the two phase regions, where the potential plateaus, the slope of the equilibrium potential curve will always approach zero. Axiomatically, the $\widetilde{D}_{GITT}$ values will always drop precipitously over this range, a result that does not fit with any physical model.

Aside, the thermodynamic factor, *W*, includes $dE_o/d\delta$ and represents the effects of interactions amongst charged species in addition to chemical potential gradients,

$$W = \left| \frac{\partial \ln a_{Li^+}}{\partial \ln c_{Li^+}} \right| = -\frac{zq\delta}{kT}\frac{dE_o}{d\delta} \qquad (21)$$

where a_{Li^+} is the activity of Li^+ in the solid, c_{Li^+} the concentration, *z* the charge number, and *q* the elementary charge. [82, 116] This factor is defined only for single phase systems and is directly proportional to the slope of the steady state voltage curve.[84] Again, one observes that variations in $\widetilde{D}_{GITT}$ are mainly due to variations in the steady-state potential curve rather than the transient potential response, a result also found by Jang et al. in order-disorder transition in $Li_{0.5}CoO_2$ thin film systems.[53]

Table 4: Values used for sensitivity analysis of GITT equation. "n" is used to emphasize the terms position as the numerator in the equation (20), and "d" the denominator.

10^{-2} to 10^{+3} (V/mole of Li)	10^{-8} to 10^{-1} ($V/s^{-1/2}$)

To better understand the kinetics within the two-phase region, in which the material undergoes phase transformation, Figure 37 shows only the terms $(dE_o/d\delta)^2$ and $(dE_p / d\sqrt{t})^2$ from eqn. (20) with lithium concentration. The latter term, $(dE_p / d\sqrt{t})^2$ represents the

magnitude of the potential transient response and is reflective of mass transport limitations in the cathode. It is proposed that this value can be used to compare the mass transport kinetics in two-phase regions. The figure shows that, as expected, the slope of the steady-state curve is similar for c-VO and f-VO while the potential transient response curve varies significantly. The f-VO, with smaller and more heavily [001] oriented grains, responds more sluggishly to current pulses over regions where phase transformation occurs. This response becomes even more pronounced with increasing lithiation. The sluggish transient responses shown by f-VO over the two-phase regions help explain the poorer rate capability compared to that of c-VO. The results suggest that rate limitations of the finer-grained film microstructure may primarily be attributed to the kinetics of phase transformation (i.e. two phase regions).

In summary, the term $(dE_p / d\sqrt{t})^2$ can be used to compare the mass transport limitations over two phase region. This term is preferred over calculating $\widetilde{D}_{GITT}$ values via the Weppner-Huggins analysis, which is applicable only to the single phase region. Over the two phase region, one might expect the effective diffusion coefficient to take on some fraction of the end member values – that is, those values established by the single phase regions.

Transmission Electron Microscopy

Due to the more faster heating ramp rate, f-VO might be expected to consist of crystallites with greater point, line, and grain boundary defects.[117] Application of large temperature gradients during rapid heating (or conversely, during cooling) limits the time over which defects can be "annealed out" via defect aggregation and annihilation reactions.[7] Elevated temperatures or longer anneal times are often used as a strategy to remove defects. Imperfections at the grain-boundary regions can strongly influence transport properties and subsequent rate capability. These grain boundary regions are more prevalent with decreasing grain size. Models of the amorphous grain boundary regions in V_2O_5 by Garofalini suggest that Li^+ diffusion along these regions can provide a rapid diffusion pathway.[27] This result was based on simulations in which the grain boundaries were perpendicular to the surface, thereby allowing Li^+ to diffuse further into the film. However, when considering transport *across* grain boundaries, as likely here, amorphous intergranular regions can serve as additional high resistance interfaces in series

[7] These annealing treatments are typical to remove defects during ion implantation in semiconductor devices and for tempering of cold worked metals.

with faster bulk diffusion.[118] In addition, electronic conductivity measurements discussed in chapter 4 revealed that amorphous films were an order of magnitude lower in conductivity compared to crystalline films. The faster diffusion pathways via grain boundaries may also, in the end, compromise electronic conductance through the film.

EELS mapping using energy-filter TEM indicated less vanadium at grain boundary regions. Highly defective intergranular regions are often sites of reduced coordination. While neutral atoms may have diffusion enhanced over these regions, it is unclear what effects the change in chemistry will impart upon ionic diffusion. The smaller grained samples may have greater structural defects located at intergranular interfaces, potentially retarding phase boundary motion through the film.

TEM studies by Iriyama et al. of the two-phase region of Li_xMoO_3 ($0 \leq x \leq 0.3$) revealed that lithium first inserts into preferred, surface-layer crystallites in a random fashion. Subsequent ordering within the crystallites occurred after an induction period before insertion proceeded into unchanged crystallites.[119] With a more favorable surface orientation and larger grains, c-VO may allow transformation within grains and phase boundary motion between grains to proceed more uniformly. In HRTEM of lithiated samples, lattice planes were observed to have some distortion (or waviness) for some grains as shown below in Figure 38. A smearing of diffraction spots also indicated a variation of lattice plane spacing, suggesting that a similar insertion and induction period may be present in $Li_xV_2O_5$ samples and that the lithiation process may proceed non-homogeneously.

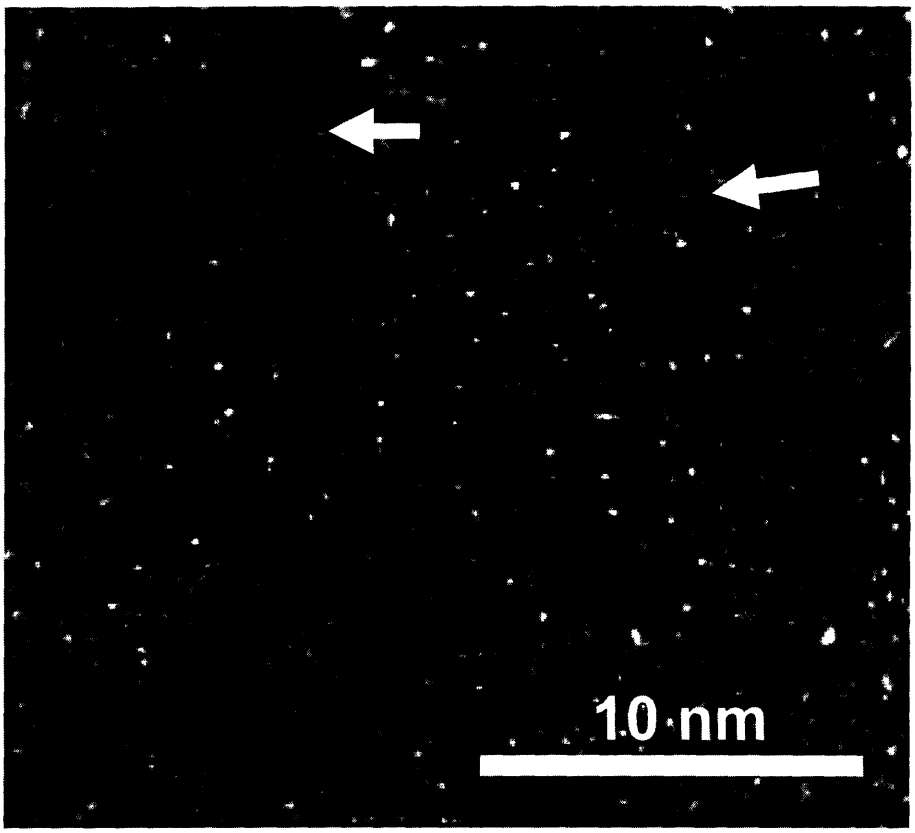

Figure 38: HRTEM of c-VO, δ-$Li_{0.9}V_2O_5$. Lattice fringes for the (001) observed in horizontal direction. The arrows point to the direction parallel to the planes.

Effects of Phase Transformation Kinetics on Performance

XRD:

To explore the differences during phase transformation between samples, XRD was also used to evaluate the composition after a slow and fast discharge to the ε + δ two phase region. Slow mass transport (diffusion or phase boundary motion) would be expected to lead to a higher concentration of the lithium deficient phases (i.e. α and ε-$Li_xV_2O_5$) in samples. Two scenarios were devised to observe the ε → δ phase transformation. In case (I), the c-VO and f-VO were discharged at a low current rate (3 μA/cm^2) into the ε+δ two phase region. The cutoff potential was fixed such that, upon relaxation, the potential equilibrated to 3.18V (surface concentration of $x \sim 0.6$, $Li_xV_2O_5$). In case (II), both samples were discharged at a higher current rate (200 μA/cm^2) into the ε+δ region and also allowed to reach an equilibrated potential of 3.18V. Relative changes in the interlayer spacing, d_{001}, allowed for an estimate of the degree of

transformation to the δ phase (~$Li_{0.9}V_2O_5$). This is shown schematically below with the degree of transformation pictorially represented. The actual expansion of the d_{001} as a function of lithium was reported by Cocciantelli et. al. (1991) and is shown in Figure 41.[120]

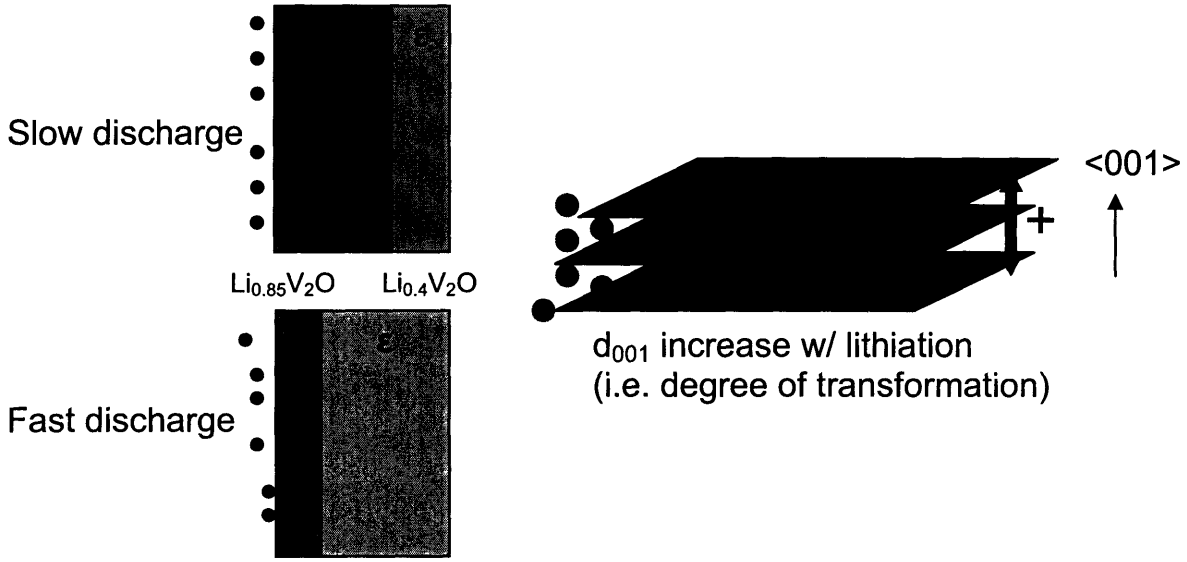

Figure 39: Picture of transformation process expected after a slow and fast discharge (left) and the increase in the d_{001} spacing with lithium insertion (right).

Table 5 shows that at the low discharge rate (case I), d_{001} has expanded by an average of 6.1% for c-VO and 4.2% for the f-VO sample. The results suggest that while the f-VO has a surface composition of ~ $Li_{0.6}V_2O_5$ during lithiation, the bulk of the film has not transformed to the extent observed in c-VO. This result is magnified at the high discharge rate (case II), where d_{001} expands by 5.8% for the c-VO but only by 1.9% for the f-VO. The latter 1.9% layer expansion for f-VO suggests that the overall bulk composition was closer to x ~ 0.1-0.2 ($Li_xV_2O_5$) and that a substantial fraction of α-phase still exists. The multiphase coexistence was further confirmed by analysis of the higher order reflections (600) and (020) peaks which showed effects of peak broadening and separation (not shown). However, the 001 reflection is at lower 2θ angles meaning that peak splitting is not as prevalent, so that only an average d_{001} could be obtained as observed in Figure 40. A clear shift in 2θ peak position is observed in addition to some broadening. Accurate quantification of the phase distribution, though, was not possible owing to the small sampling volume in the films.

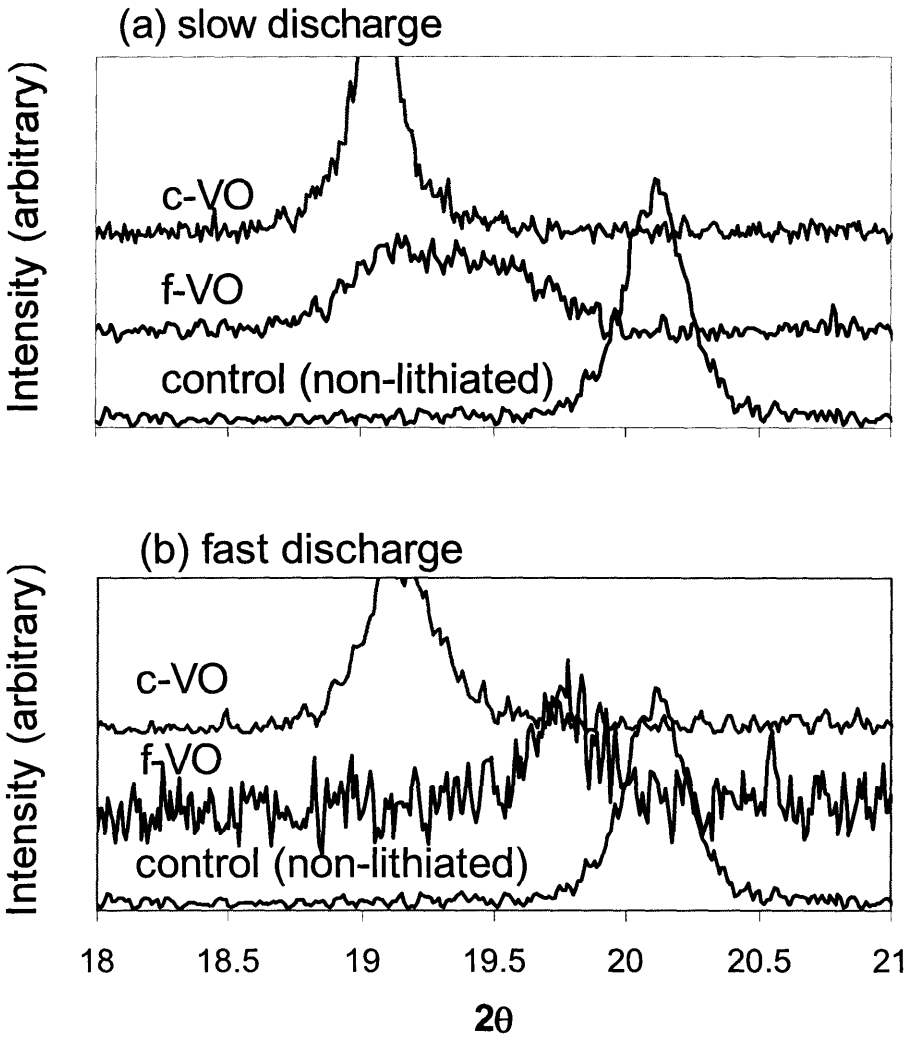

Figure 40: XRD showing (001) peak after (a) discharge at 3 μA/cm^2 and (b) discharge at 200 μA/cm^2.

Table 5: Relative change in layer spacing, Δd_{001} for case (I) 3 μA/cm^2 and case (II) 200 μA/cm^2 discharge rate.

	Case I (slow)	Case II (fast)
c-VO	+6.1%	+5.8%
f-VO	+4.2%	+1.9%

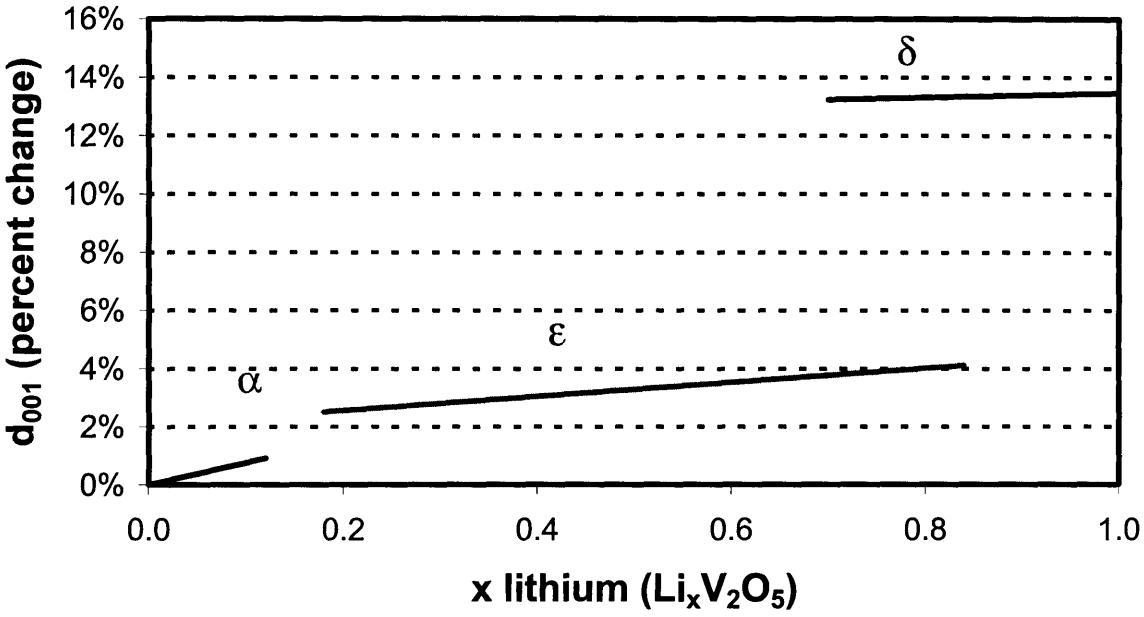

Figure 41: Change in d_{001} spacing as a function of lithiation. Reproduced from Cocciantelli et. al. (1991).[120]

SIMS Measurements

Samples that were galvanostatically titrated to the beginning, middle, and end of the ε → δ phase transformation were also compared (Figure 42) using SIMS which revealed how allowed the Li^+ concentration with position. To heighten the sensitivity of the measurement, the analysis was performed on films prepared on polished ITO/aluminosilicate substrates rather than Al foil. The grain orientation was largely similar to c-VO as shown in Table 6 but with smaller grain sizes (100-200 nm). The V/O intensity ratios were consistent between samples and uniform with depth. The estimated nominal compositions based on the integration of the ion intensities were (a) $Li_{0.49}V_2O_5$, (b) $Li_{0.66}V_2O_5$, and (c) $Li_{0.90}V_2O_5$. These values reasonably matched those obtained from the electrochemical results based on the steady state voltage curve and capacity: (a) $Li_{0.55}V_2O_5$, (b) $Li_{0.69}V_2O_5$, and (c) $Li_{0.90}V_2O_5$.

Table 6: Percent grain orientations based on XRD peak intensities, V_2O_5 on ITO.

	{200}	(001)	{110}	(310)	(020)
V_2O_5 on ITO	18.2%	0.0%	51.3%	15.7%	14.7%

The Li^+ concentration at the film surface was unexpectedly lower than the film bulk. Part of the initial variation is due to surface roughness (~ 10-15 nm) and passive film formed from the electrolyte. This was detected by measuring the carbon concentration which showed a layer of ~ 60 nm at the surface. Other effects, such as sample charging and material modifications caused by recoil-implantation, may induce ion migration and make interpretation of Li^+ concentration profiles difficult.[121-123] Several parameters were adjusted, including the use of a gold coating on the surface, application of an e-beam for charge neutralization, and use of the negative ion detection mode, to help reduce charging effects. However, the Li^+ depletion at the surface was still observed and appeared unchanged.

Still, it is interesting to note that in Figure 42 the Li^+ concentration diminishes linearly for films in the beginning and middle of the $\varepsilon \rightarrow \delta$ phase transformation, but not for the sample where transformation is completed. The linearity in the SIMS curve may suggest that phase boundary motion does not proceed as a planar front through the film. If the latter were true, it would be expected to result in a sharp drop in the lithium concentration with depth as the film is converted from ε to δ (absent substantial SIMS induced migration within the film bulk). Instead, a slight linear decrease is observed for (a) and (b), a result suggesting that the ratio of c_δ/c_ε (delta/epsilon phase concentration) is on average decreasing with depth. Similar to Iriyama's results showing a random, variable phase concentration within surface grains, the SIMS analysis suggests that the phase boundary penetration (and front) may be variable through the film rather than uniform.[119] Notably, the single phase δ sample (c) has a more uniform Li^+ concentration as would be expected.

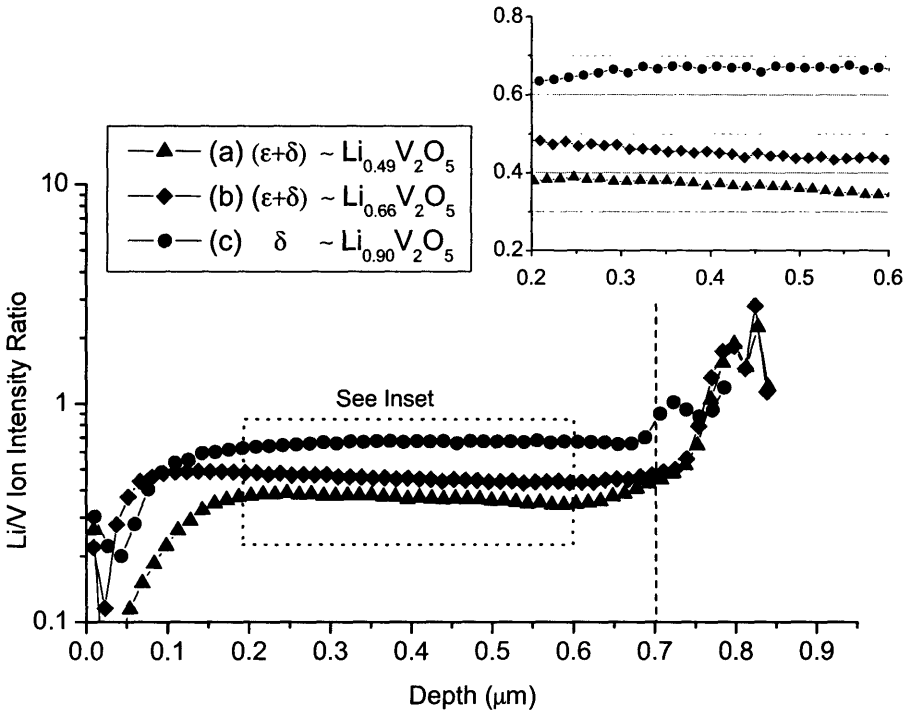

Figure 42: SIMS results showing Li/V concentration with depth for samples undergoing galvanostatic titration and equilibration to the (a) beginning, (b) middle, and (c) end of the ε → δ phase transformation. Dashed vertical line denotes the substrate.

This difference in lithium concentration is not attributed to slowness in diffusion, as the samples were equilibriated within the electrochemical cell and further allowed to rest upon removal for 4+ days before the SIMS analysis. In addition, a control sample fully titrated to the δ-phase showed more uniform lithium concentration. Very slow or hindered phase boundary motion would thus be responsible for a composition change with depth. The change in the ratio of ε and δ with depth suggests that there is an energy barrier preventing further transformation. This energy barrier appears to be higher for the f-VO sample rather than the c-VO sample based on GITT, capacity-rate testing, and SIMS results.

Substrate Effects

The poor performance may also be due to substrate effects from the aluminum foil that dominate at the thinner length-scales, but become negligible for the thicker films. It is also known that local substrate defects and substrate-film lattice misfit can lead to significantly

different local microstructures.[21] Thermal expansion coefficients for the aluminum foil (with an Al_2O_3 layer) are larger than that of the vanadium pentoxide film which may perturb the microstructure of the thinner samples so that the rate performance is more analogous to that of a randomly oriented structure rather than an oriented structure. XRD patterns of V_2O_5 films on dummy Si wafers (100) showed higher degrees of preferred orientation than the V_2O_5 on Al foil, supportive of the possibility of some substrate influence.

To investigate the role of strain, diffraction patterns from the f-VO and c-VO samples were refined and the FWHM, peak shifting, and lattice parameters were compared. For both heat treatments, the lattice parameters for a_o, b_o, and c_o deviated by less than 1% from the reported values $a_o = 11.516$, $b_o=3.5656$, $c_o= 4.3727$ Å.[115] Figure 43 displays the strain measured as a function of each d_{hkl} spacing based on Bragg's law, following the relation:

$$\varepsilon_{hkl} = (d_{hkl} - d_o)/d_o \qquad (22)$$

It is notable that all the planes are under a tensile strain, indicated by the positive sign. The interlayer spacing (001) is under the largest strain ($\varepsilon \sim +0.01$) for both samples. No significant differences between the samples are observed however that would explain large differences in performance, such as due to increased diffusion pathways.

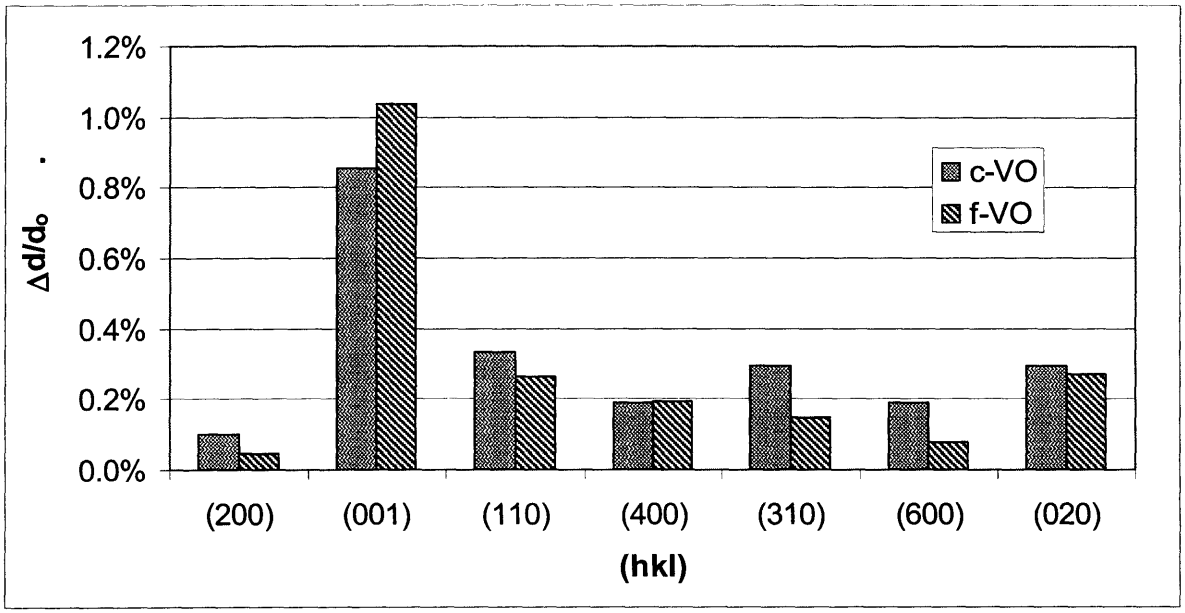

Figure 43: Strain present in the annealed c-VO and f-VO samples as measured via XRD.

The lattice mismatch of the V_2O_5 on the Al substrate can be compared with that of ITO via the misfit parameter, f_m, whereby

$$f_m = (a_{V2O5} - a_{Al})/a_{Al} \qquad (23)$$

where a_{V2O5} is one of the lattice parameters of V_2O_5 and a_{Al} is the aluminum substrate (or ITO substrate). The values shown below reveals that both substrates cause some strain for the V_2O_5 sample.

Table 7: Misfit parameters for V_2O_5 on Al and ITO substrates

V2O5	Al	ITO
a	1.84	0.12
b	-0.12	-0.65
c	0.08	-0.57

Interfacial Effects

In addition to differences in mass transport between c-VO and f-VO, interfacial effects were also considered. The initial *IR* drop during GITT measurements was used as a measure of the polarization corresponding to the summation of electrolyte, interfacial, and electronic resistances in the cathode and cell. Values for R_{GITT} ranged from 6 to 11 kΩ for c-VO and 11 to 17 kΩ for the f-VO over the lithiation range. For both samples, R_{GITT} increases rapidly from the lower range values to the higher values with increasing lithiation (*not shown*). Impedance spectroscopy and further polarization analysis were used to better understand trends in these results.

Different crystal habits at the surface may be expected to exhibit differing electrode-electrolyte interactions (e.g. adsorption, defect sites, surface charge). Although well matching equivalent circuits were not found due to the complexity of the system, impedance results showed the more randomly oriented f-VO with higher resistances associated with the interface (34 vs. 11 kΩ-cm^2), as shown in Figure 44. This may potentially be due to differences in orientation at the surface or surface roughness associated with the smaller grain sizes.

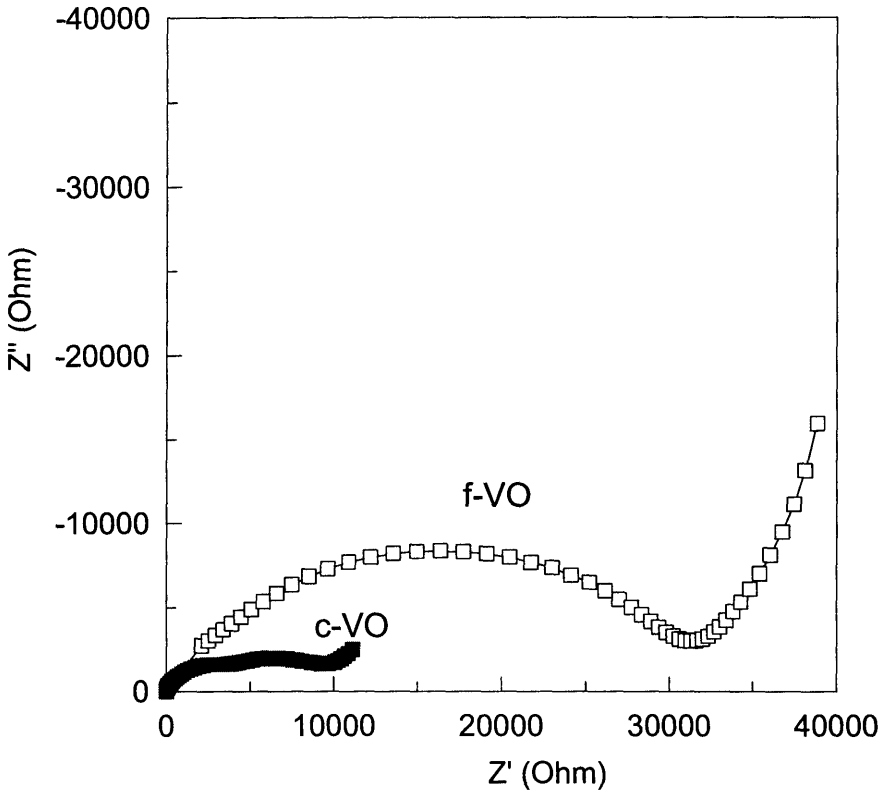

Figure 44: Impedance spectra of c-VO (filled squares) and f-VO (open squares) at 3.35V vs. Li

Impedance scans were taken as a function of potential (or lithiation) for both c-VO and f-VO samples (see Figure 45). A possible equivalent circuit, shown in Figure 46, was inferred. The complexity of the system did not allow a good match to be found, however the equivalent circuit is a typical one. R_s represents the cell resistance and electrolyte resistances, the first resistor and constant phase element in parallel (R_1 and CPE_1) representing perhaps a passive film, the second resistor and capacitor in parallel (R_2 and CPE_2) describing the charge-transfer reaction at the interface. Finally, a Warburg impedance is added to capture solid-state diffusion within the cathode.

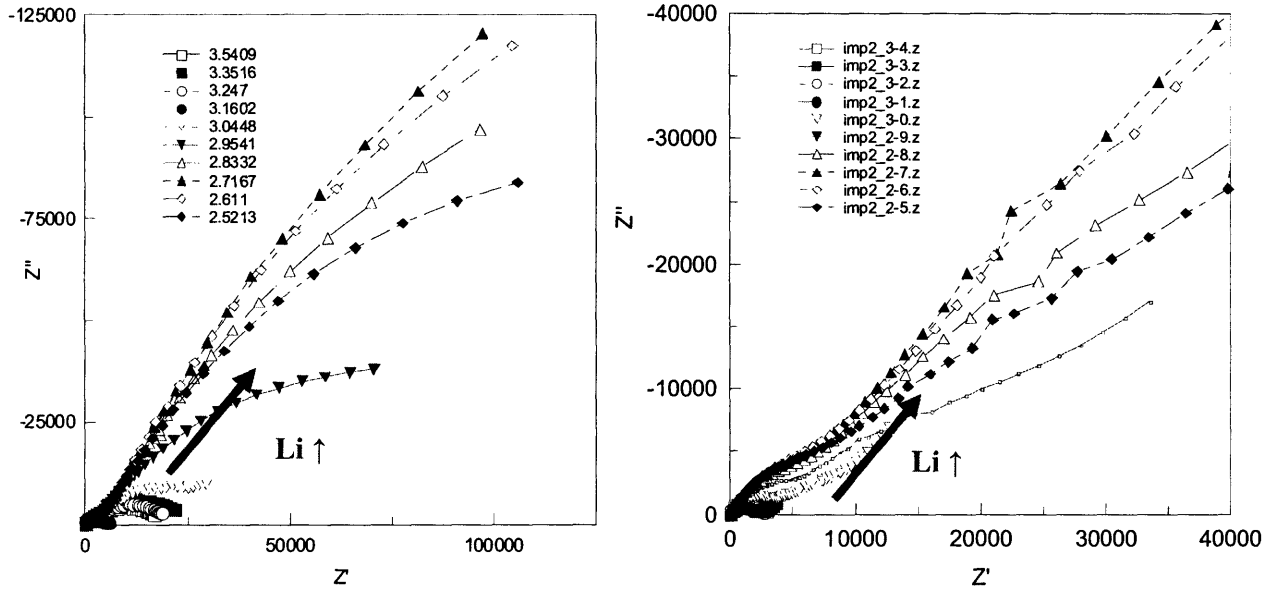

Figure 45: Impedance spectra of (left) f-VO and (right) c-VO with lithiation. Potential values vs. lithium shown.

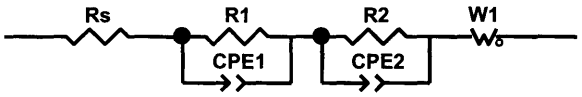

Figure 46: General equivalent circuit used to fit the impedance plots.

Qualitatively, it is of interest to compare the calculated values from the fit, shown in Figure 47. It appears that R_2 is relatively lower for both samples compared to R_3. R_2 for the c-VO appears to grow significantly while R_2 for f-VO remains relatively constant – possibly suggesting growth of a passivating film with lithiation in c-VO. In terms of charge-transfer resistance, R_3, c-VO is observed to have initially smaller values (i.e. at higher potentials), but then becomes more nearly equal to f-VO upon transforming to the δ phase ($\leq$ 3.0V). The large overall increase in R_3 upon entering into the δ phase also suggests that changes in the physical structure with transformation may invoke changes in the surface chemistry.

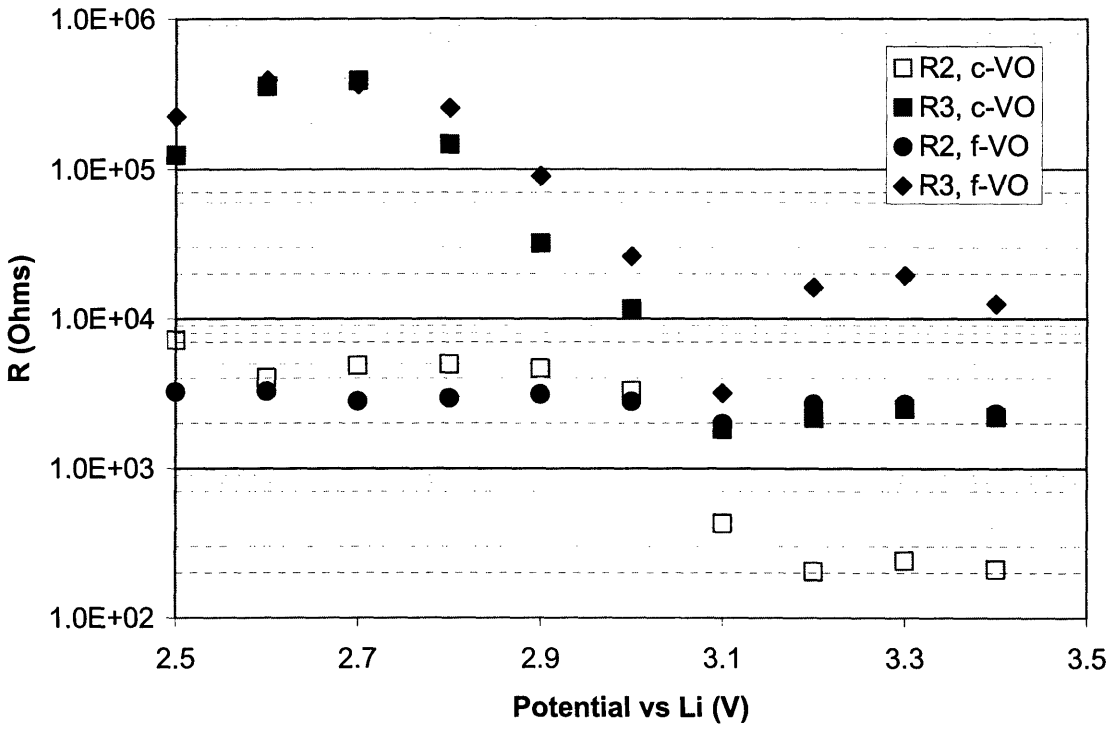

Figure 47: The values for R_2 and R_3 generated by the equivalent circuit for c-VO and f-VO samples

Morphological differences between oriented and non-oriented systems, including varying crystal habits and surface roughness, can result in differing interfacial properties and cell performance characteristics. While sample c-VO shows lowered R_{GITT} over the whole lithiation range, both systems show higher interfacial resistances for the δ-phase. Typically, the layered structure of $Li_xV_2O_5$ begins to buckle upon reaching the δ-phase which may contribute to the slower charge transport across the interface.

An analysis of the polarization that occurred during galvanostatic testing also supported the impedance and R_{GITT} results. The potentials of the α+ε and ε+δ plateaus were identified by taking the differential of the capacity versus potential, which allows identification of the potential plateaus (or peaks). The potential peak locations were plotted against current densities in Figure 48. The resulting slope revealed c-VO having resistances, R_η, of ~ 1.3 and 1.7 kΩ for the α→ε and ε→δ reaction respectively, while for f-VO these values were R_η ~ 14 and 24 kΩ

(see Table 8). These resistances represent the summation of both activation and bulk concentration polarization. The three results ascertained from evaluating the *iR* from the GITT data, from impedance plots, and the differential capacity all suggest that interfacial resistance is larger in the samples having greater percentage (001) orientation and smaller crystallites.

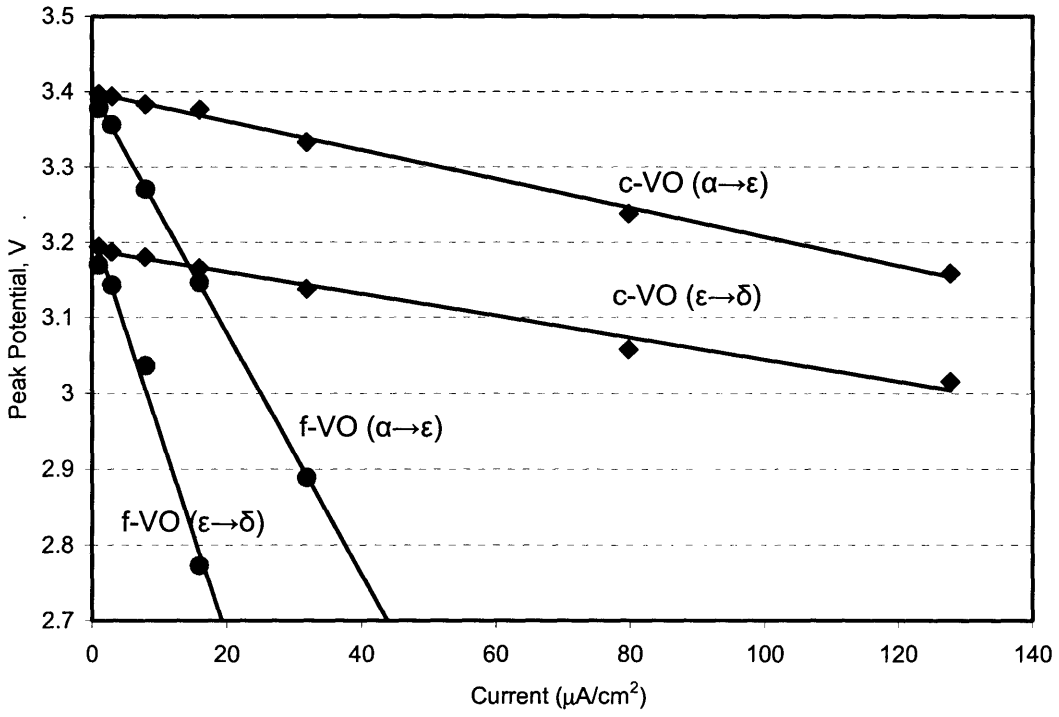

Figure 48: Peak position as measured by the differential capacity plot, as a function of current density. The slope represents the degree of polarization.

Table 8: Derived values based on a linear fit of the plots in Figure 48.

Sample	transformation	R (Ω)	E_o (V)	r^2
c-VO	α → ε	1680	3.3993	0.9965
	ε → δ	1326	3.1896	0.9849
f-VO	α → ε	14059	3.3990	0.9996
	ε → δ	23696	3.2182	0.9821

Table 9: Expected magnitude of polarization based on different values of interface resistances and current densities.

	j (uA/cm2)	0.75	1	3	8	16	32	64	96	128
	I (uA)	0.85	1.13	3.39	9.05	18.10	36.19	72.38	108.57	144.76
[redacted]		0.00	0.01	0.02	0.05	0.09	0.18	0.36	0.54	0.72
		0.01	0.01	0.03	0.07	0.14	0.27	0.54	0.81	1.09
		0.01	0.01	0.03	0.09	0.18	0.36	0.72	1.09	1.45
		0.02	0.03	0.08	0.23	0.45	0.90	1.81	2.71	3.62
		0.04	0.06	0.17	0.45	0.90	1.81	3.62	5.43	7.24

The results suggest that interfacial resistance is significantly larger in the samples having greater percentage (001) orientation and smaller crystallites. The effect of this difference in interfacial performance is demonstrated in Table 9, which compares the expected polarization with the charge-transfer resistance. At current rates approaching 100 $\mu A/cm^2$, the degree of polarization is severe with resistances greater than 5 $k\Omega$. These polarizations lead to greater suppression of the potential plateaus in f-VO compared with c-VO.

This result is further supported in an analysis of the capacity contribution of each two phase region ($\alpha+\varepsilon$ and $\varepsilon+\delta$), which was evaluated for Samples c-VO and f-VO (not shown). While the capacity contribution of the $\alpha+\varepsilon$ capacity contribution remained constant for both samples, the capacity contribution for the $\varepsilon+\delta$ phase transition was virtually absent at higher current rates for f-VO, explaining much of the performance loss in capacity. The buildup of lithium in the randomly oriented surfaces appears to cause greater concentration polarization and a resultant suppression of the voltage plateaus.

Summary

It was found that phase transformation kinetics can limit the current-rate performance in thin film V_2O_5. The use of the term $(dE_p / d\sqrt{t})^2$ was proposed to measure the degree of polarization during the phase transformation process and effective limitation due to both diffusion and phase boundary motion. Differences in orientation appear to affect the ability for phase boundary motion to proceed rapidly through the film. Experimental results suggest that the phase transformation may proceed in an inhomogeneous fashion through the film rather than as uniform, planar front. Interfacial resistance was also measured to be significantly larger for the more poorly oriented films. Collectively, these results are shown to largely explain the order of magnitude difference in capacity-rate performance in thin film V_2O_5.

Chapter 6: Grain Size and Thickness Effects

The effects of grain size distributions and microstructure on the rate performance of lithium ion batteries are explored in this chapter. Optimization of thickness in the absence of additives that enhance electronic conductivity – in order to determine the maximum thickness desirable from a performance perspective for thin film V_2O_5 is also considered. Several metrics are devised to help understand the thickness-performance relationship.

Controlling Grain Size

Experimental:

Distinct microstructures and grains were formed from amorphous films through post-deposition heat treatments as discussed earlier in chapter 4. Nucleation and coarsening theory was used to guide the processing steps. In general, larger thermal gradients led to more rapid crystallization and to formation of finer, semi rounded grains. Slower thermal gradients (via slower heating rates), produced coarser grains with strong faceting and more nearly rectangular shapes. Longer thermal treatments facilitated coarsening of the larger grains at the expense of smaller grains. In general, temperatures above 300°C resulted in fully crystalline films ($T_{m.p.}$ = 670°C).

Lattice mismatch between the substrate and film can also affect film orientation and film strain. Because of the orthorhombic structure of V_2O_5 ($a_o \neq b_o \neq c_o$), virtually all substrates will have at least one lattice parameter mismatched. Substrates with good lattice matching to V_2O_5 usually do not meet the additional requirements for (1) high electronic conductivity, (2) resistance to chemical reaction at elevated temperatures, (3) electrochemical inactivity with lithium and the electrolyte within the working potential range, and (4) flatness, and (5) cost.

ITO was selected as a substrate because of its ability to be sputtered, low surface roughness, electronic conductivity, and inactivity with lithium and the electrolyte. Unfortunately, the lattice matching was less than ideal although not worse than other metal systems (a_o = 10.2831 Å following a 300°C heat treatment).[124] Nucleation and island growth is expected for both Al and ITO substrates. During the annealing step, ITO is expected to expand similarly to V_2O_5 as the thermal expansion coefficients are comparable whereas that of Al is higher. The relative orientation in the film was investigated by x-ray diffraction. In general, films sputtered

onto the ITO/glass substrates were highly [110] oriented. The unique orientation, not observed by others, is suspected to be a processing artifact – largely caused by the sputtering angle being roughly 30° from the substrate's normal. The angle results in amorphous columnar growth that is at an angle relative to the substrate, as shown in Figure 49. Subsequent crystallization, it is believed, results in the <200> being parallel to the growth direction. The [001] orientation, normally the strongest peak and slowest diffusion direction, was observed to be largely absent in the films.

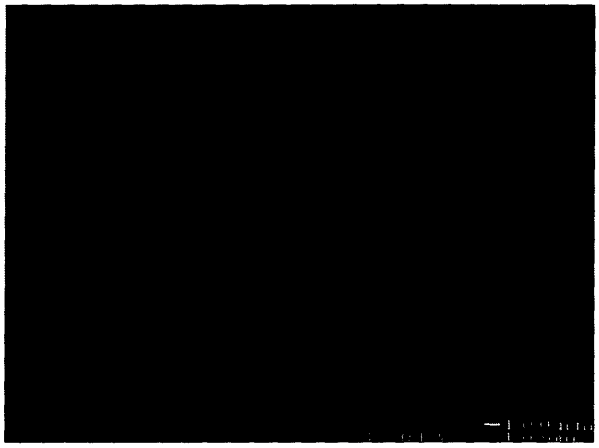

Figure 49: X-ray Amorphous V2O5 films as sputtered on ITO/Glass

Sample SEM images of the following heat treatments are shown below in Figure 50(a)-(d).

Table **10** reports the various heat treatments. The red arrow represents the V_2O_5 growth direction from the ITO/glass substrate. Different microstructures can be obtained depending on the post-anneal treatments.

Table 10: Sample Heat Treatment Description

HT1	300	0.5	24	≤ 10	1, Air
HT2	500	70	1.5	≤ 10	1, Air
HT3	500	0.5	1.5	≤ 10	1, Air
HT4	400	1	1.5	≤ 10	1, Air

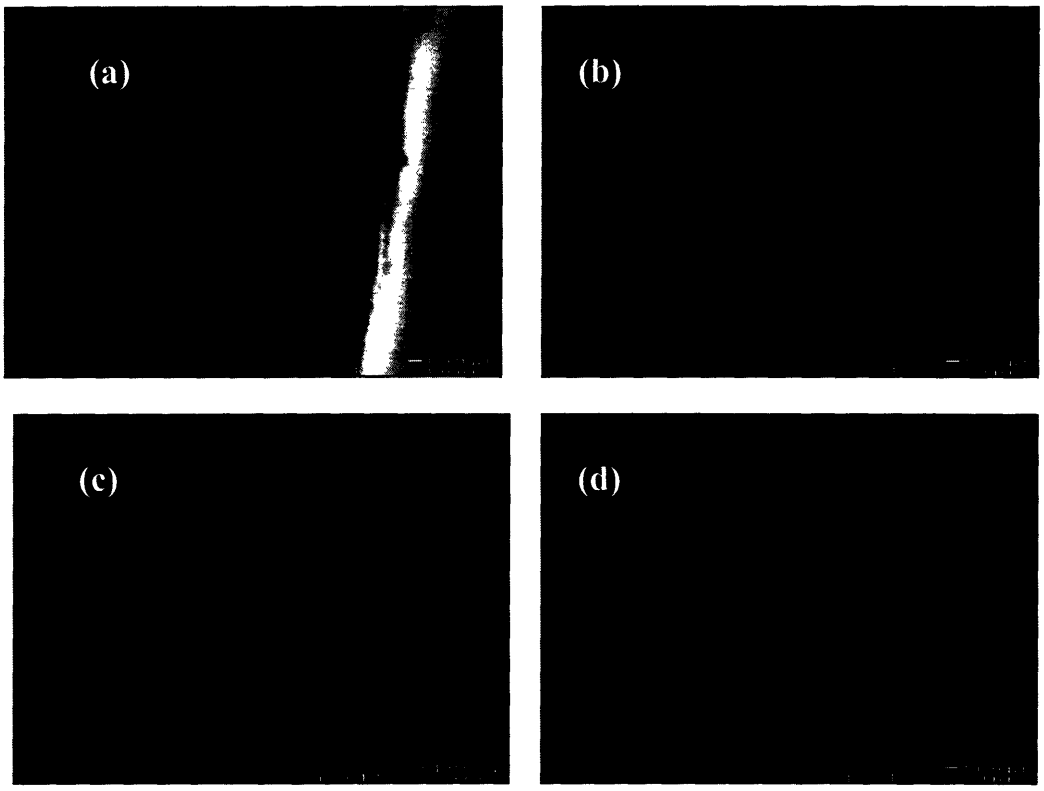

Figure 50: V_2O_5 films from same sputtering run undergoing (a) HT1, (b) HT2, (c) HT3, (d) HT4. Arrows denote growth direction.

The overall grain orientations from a sample set of films are shown in Figure 51. The orientation for the ITO substrate samples are shown to be largely independent of the heat treatment, again suggesting that the orientation is controlled by the substrate and sputtering conditions in the ITO substrate rather than the post annealing treatment.

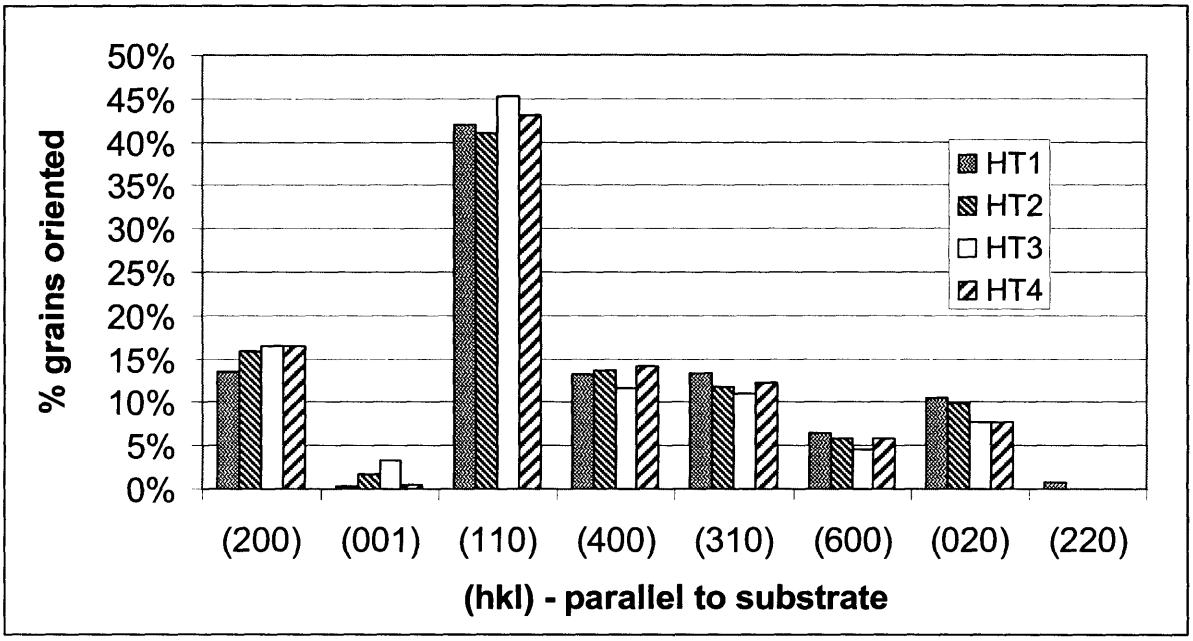

Figure 51: Percent of V_2O_5 film grains in specific orientation as a function of heat treatment.

The d-spacings were measured by peak profile fitting of XRD peaks using Jade 7.0 software. The peaks were similar with only slight variation from sample to sample. In general, d-spacings were less than 0.7% larger than those reported in the powder diffraction files for V_2O_5 (PDF#01-086-2248), as shown in Figure 52. The graph displays the strain corresponding to each d_{hkl} spacing calculated using Bragg's law, following the relation for strain shown earlier in equation 22. The results suggest that the film is under slight tensile strain, analogous to the Al substrate samples. This may be due perhaps to lattice mismatch with the ITO sample and/or expansion of oxygen-deficient V_2O_5 amorphous films into crystalline V_2O_5 during annealing.

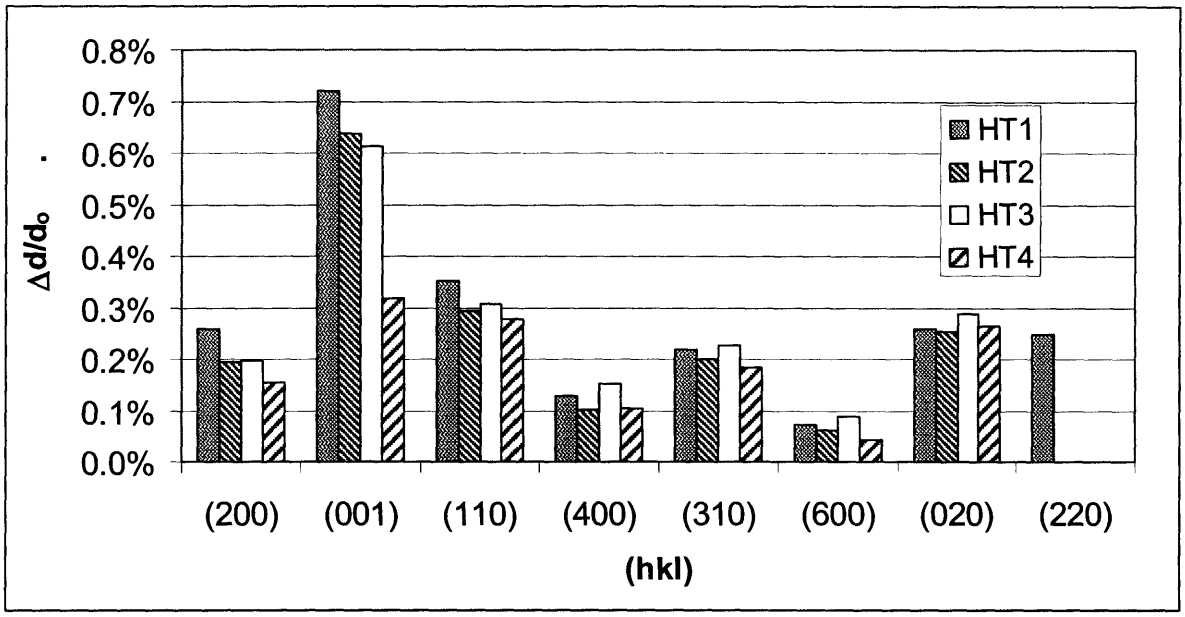

Figure 52: Strain as measured from a change in d-spacing for lattice planes relative to a reference diffraction pattern.

Cross-sections of films were prepared and imaged by SEM. The variations in microstructure (from more rectangular, columnar grains to finer, faceted grains) made it difficult to compare grain sizes. Parameters including grain shape/geometric form, grain size, grain surface texture, and roundness (i.e. curvature of corners) make it difficult for distinct comparisons to be made.[8] Two measurements per identifiable grain, roughly at a 90° angle, were taken and averaged. Typical magnifications used for analysis were between 40,000 – 60,000x. Due to the limitations in image resolution, nanograins (< 50 nm) are expected to be undercounted. Even smaller subgrains, characterized by regions separated by small-angle grain boundaries, are typically unobservable absent high-resolution TEM of the lattice planes. Histograms (Figure 53) below show the distribution of average grain dimension using this approach. Figure 54 is also included showing additional heat treatments that were performed on a separate batch (i.e. sputtering run). It is important to note that while large grains may occur less frequently, they represent a larger volume fraction relative to the smaller grains. In addition,

[8] Interested readers about particle analysis are directed to Elisabeth T. Bowman, Kenichi Soga, and Tom Drummond (2000), "Particle shape characterization using fourier analysis," University of Cambridge, Geotechnical and Environmental Research Group, Technical Report #315, CUED/D-Soils/TR315. Last viewed 3/31/2005, http://www-civ.eng.cam.ac.uk/geotech_new/publications/TR/TR315.pdf

because of batch to batch variation, it is important to compare only samples from the same batch in order to infer trends.

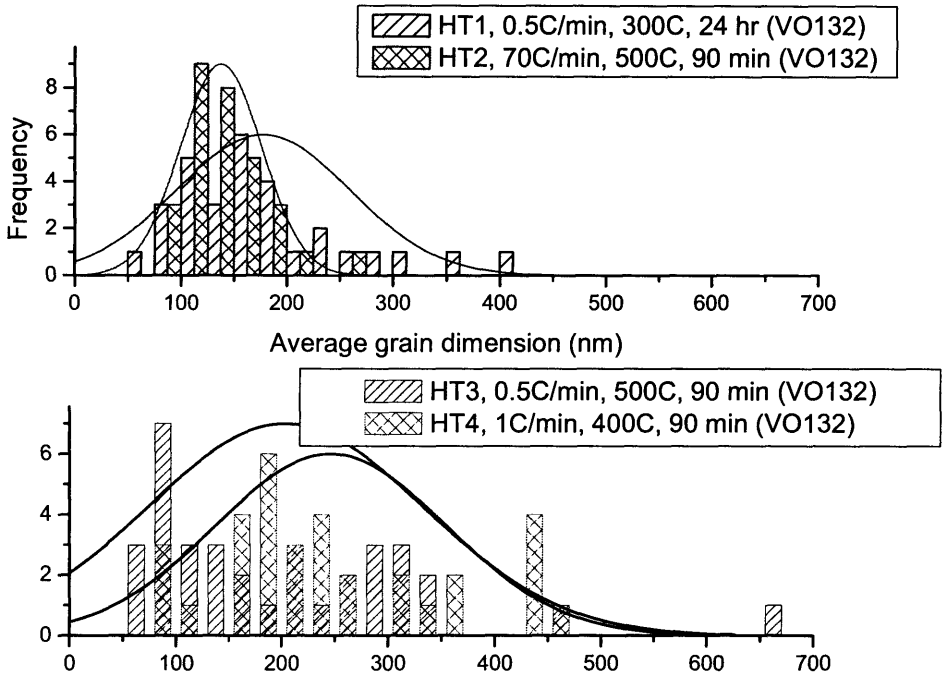

Figure 53: Histograms of average grain dimensions for 4 heat treatments (film batch #VO132). Discussed throughout unless otherwise stated.

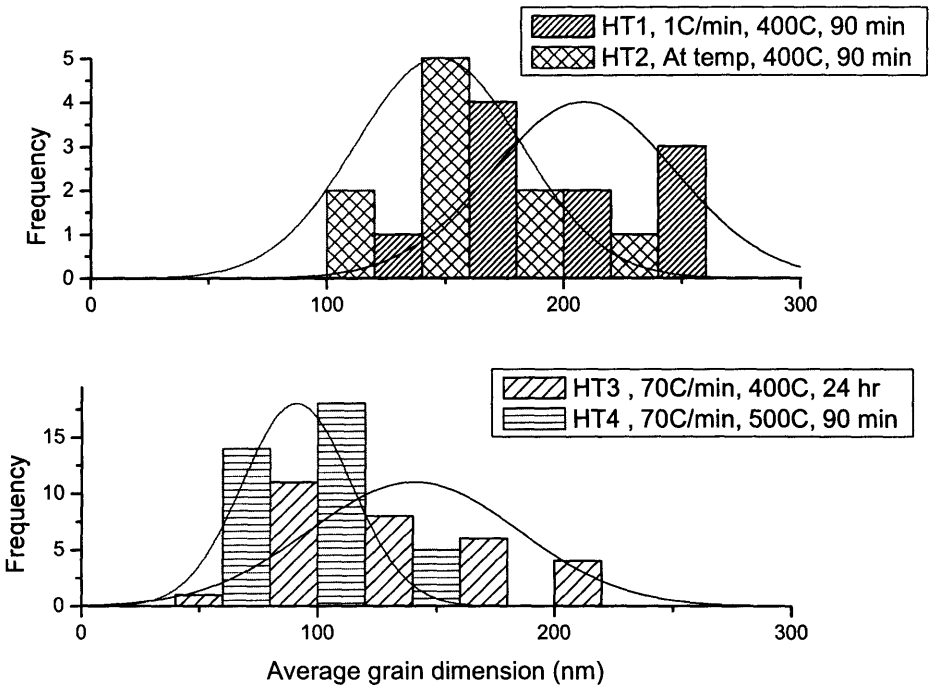

Figure 54: Additional histograms for another sample. Histograms of average grain dimension for 4 heat treatments (film batch #VO131).

Samples were subjected to other heat treatments (not shown). The general trends are summarized here. As expected, the fast thermal ramp rates and higher temperatures result in smaller average grain sizes with a narrower distribution. Slower thermal ramp rates, creating a more uniform thermal front, result in less nucleation and larger grains. Longer anneal times allow for further coarsening as evidenced by a broadening of the grain size distribution. Unexpectedly, placing samples into pre-heated furnaces, rather than ramping up from room temperature, results in larger average distributions perhaps due to greater thermal variation through the sample and substrate (i.e. hot spots in the sample). The results suggest that the "ideal" anneal step to obtain the smallest grain size would consist of a flash anneal whereby multiple nucleation sites are initiated but the growth time kept to a minimum. The largest polycrystalline grain structure can be obtained through limiting the nucleation via a small thermal gradient and to use directional crystallization (e.g. similar to single crystal growth). Summary statistics are given in Table 11.

Table 11: Summary statistics for grain size distributions

	Mean (nm)	Standard Deviation	Min (nm)	Max (nm)
VO132HT1	177	82	68	407
HT2	138	39	76	267
HT3	203	130	62	658
HT4	200	78	60	428

A second measurement system involves estimating the volume represented by each grain, as opposed to simply the average dimension. An ellipsoidal volume was estimated by using the long and short axis of each grain. Because two dimensional images were taken from SEM micrographs, a third length was estimated by taken the average of the long and short axis. The resulting volume representations are shown in Figure 55 and Figure 56 shown below. Figure 55 displays the volume represented by each grain measured for the different heat treatments. The strong overlap of the volumes may represent more a function of the measurement and volume calculation procedure (i.e. assumption of ellipsoidal shapes). Interestingly, sample HT3 shows some discrepancy in volume suggesting a more distinct grain shape. It is clear from this graph that while the majority of grains are below 200 nm in dimension, the largest grains represent 1-2 order of magnitude increases in volume. Thus the larger grains comprise a disproportionate fraction of the total volume.

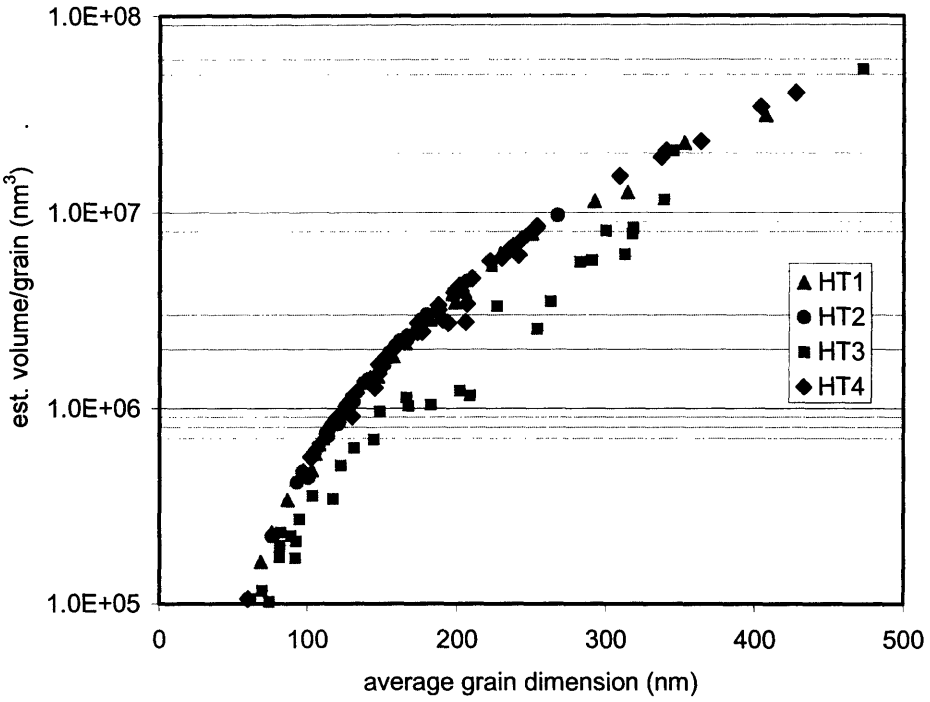

Figure 55: Estimated cumulative volume of grains as a function of average grain dimension, based on measurements taken from SEM micrographs.

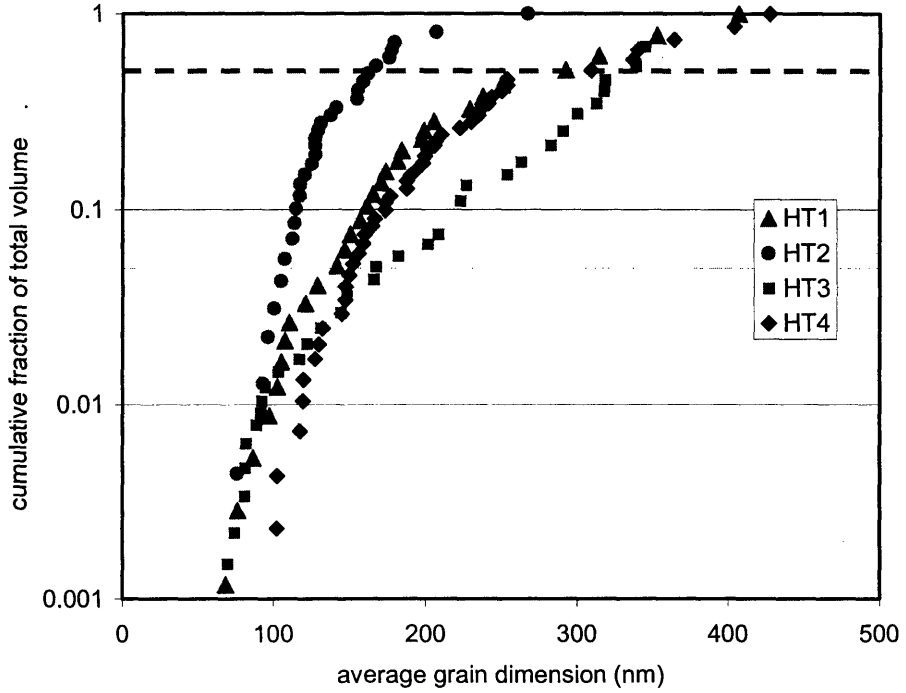

Figure 56: Cumulative fraction of total volume based on average grain dimension. Red dashed line indicates 50% of total volume.

In Figure 56, the cumulative fraction of volume based on grain size is shown on a log scale. The red dashed line delineates a volume fraction of 50%. The differences from sample to sample are clearer in this figure, as 50% of the volume for the fast thermal ramp rate (HT2) is made up by grains between 150 – 250 nm while for the slower ramp rates 50% of the volume is made up by grains between ~ 250-500 nm. Figure 56 also shows the cutoff in grain sizes at ~ 300 nm for the fast thermal ramp rate (HT2).

To evaluate differences in grain boundary volume, the following procedure was used. The surface area was estimated by assuming a tetragonal grain, assuming a grain boundary width of ~ 1 nm, and dividing by the estimated bulk volume. The results are shown in Figure 57 below. The trend shows HT2, with a finer grained microstructure, having roughly twice the grain boundary areas as other samples.

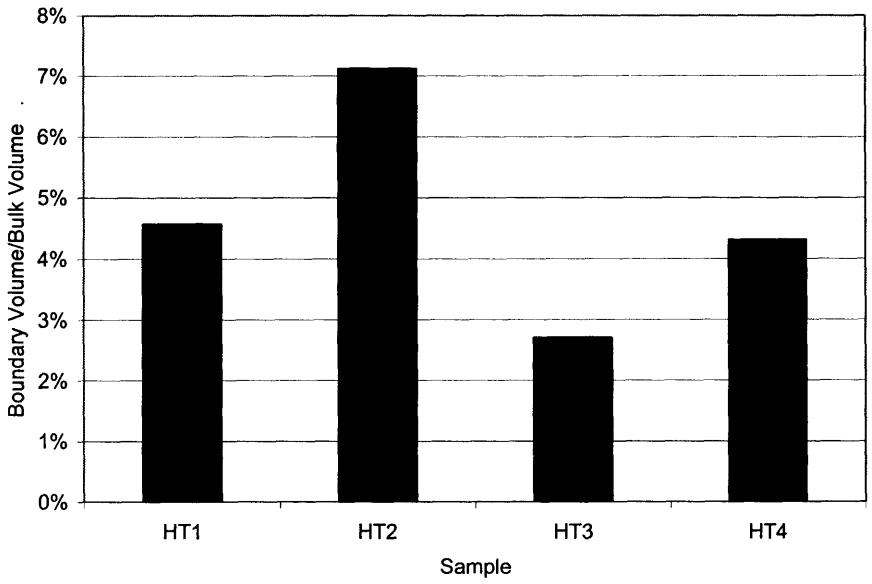

Figure 57: Estimated ratio of grain boundary to bulk volume for various heat treatments.

Experimental Results

The dependence of capacity on current rate was determined for the films. Results are shown in Figure 58. Interestingly, the different film microstructures perform similarly despite differences in the grain morphology, size, and volume of grain boundaries. The fine grained systems (HT2) – with a larger fraction of grain boundaries, would be expected to result in

improved capacity-rate performance if grain boundary diffusion played a significant role. However, no significant performance enhancement beyond the experimental error is observed. The result suggests that grain boundary diffusion is not the dominant characteristic affecting the film performance.

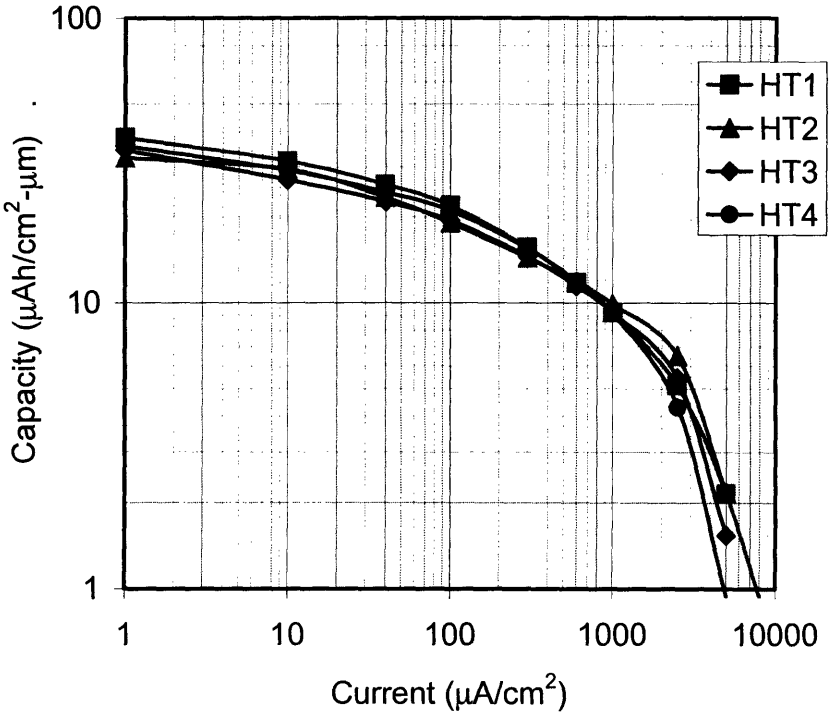

Figure 58: Capacity-rate performance of cells made using samples undergoing HT1 through HT4. Note log-log scale of plot.

Hence, differences in grain size distributions and grain boundary volumes (2.5-7%) do not appear to affect the capacity-rate performance. Partly, this may be due to the size distributions being broad and overlapping. However, these ranges present typical and reasonable distributions for polycrystalline thin films – it would be expected that practical production techniques would yield similar distributions. A close visual inspection of the film microstructures show more variation than the mean size alone might suggest. Additionally, the estimated range in GB volumes (2.5-7%) is large enough that large differences in D_{GB}/D_{Bulk} should be noticeable in the capacity-rate performance.

Based on electronic conductivity measurements (see chapter 4), the solid-state diffusion would be expected to be the limiting factor at the lower rates. The chemical diffusion coefficient with lithiation is shown in Figure 59, obtained using GITT as discussed in Chapter 3. The corresponding transient response curve is also shown in Figure 60.

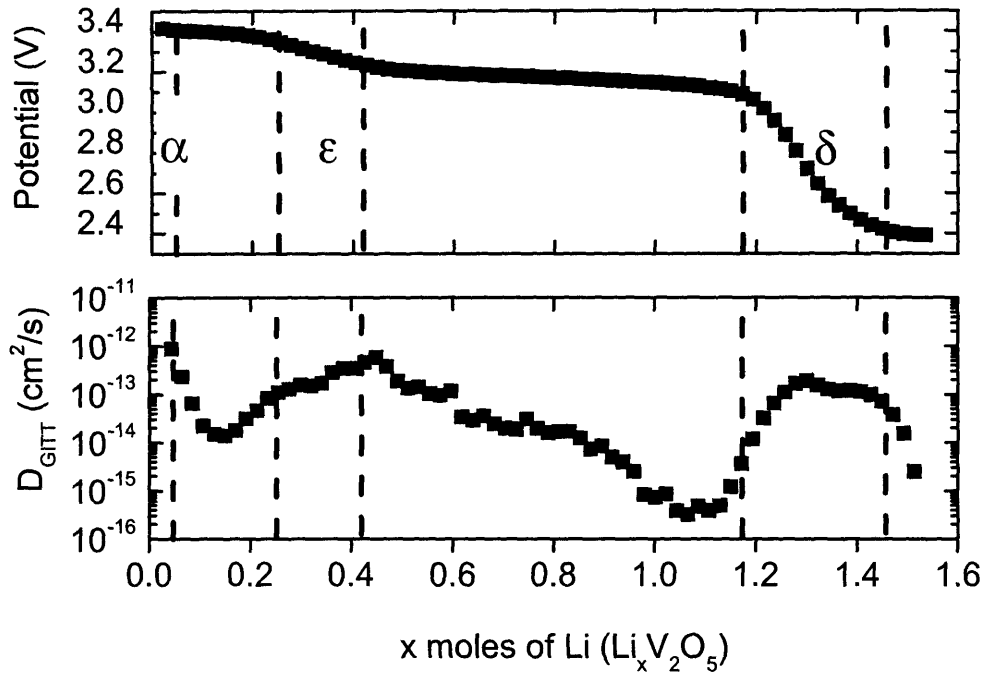

Figure 59: (Top) Equilibrium potential curve and (bottom) D_{GITT} vs. concentration

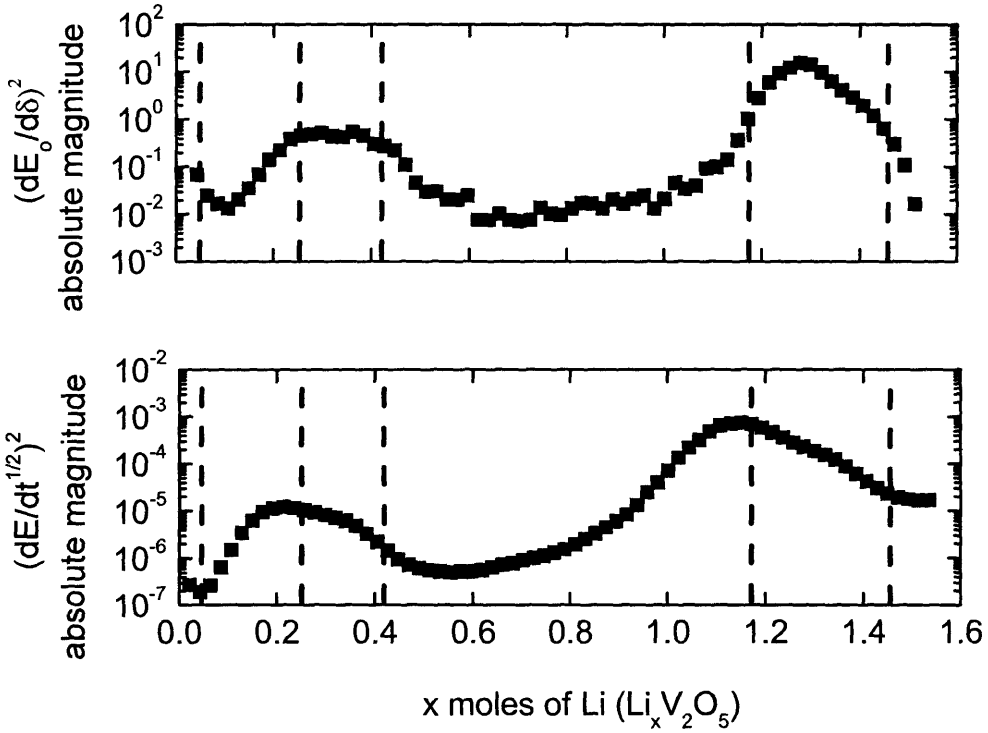

Figure 60: GITT (top) slope of equilibrium voltage curve and (bottom) potential transient response curve.

One important conclusion that may be derived from the results is that approaches that focus on grain boundary engineering for thin film cathodes may lead to only limited improvements in power performance. Based on electronic conductivity studies in Chapter 4, amorphous regions perform an order of magnitude lower than crystalline regions. Thus a tradeoff may also occur between electronic conductivity and solid-state diffusion in grain boundaries. If the grain boundary strategy is pursued further, thin films with grain boundaries perpendicular to the substrate and extending through the thickness would be ideal (i.e. columnar type grains). Deposition processes that allow for uniformly sized grains with high grain boundary segregation coefficients would also be desirable.

Amorphous and Crystalline Film Comparisons

Performance comparisons were made between a crystalline and an amorphous film from the same sputtering sample discussed above. While the initial capacities are somewhat different between amorphous and crystalline films, the important comparison is the drop off in capacity, as shown in Figure 61. It is observed that the amorphous sample has poorer performance above 300 $\mu A/cm^2$. The capacity rate performance is several times lower than the crystalline version. While it has been reported that amorphous films have a higher diffusion coefficient, the lower electronic conductivity can also partially dominate at the higher current rates, particularly for thicker films (in this case, 560 nm). Table 12 below displays a possible explanation for the poorer performance observed from amorphous films by examining the differences in electronic conductivity. In chapter 4, the electronic conductivity was reported as $\sim 10^{-6}$ S/cm for crystalline samples versus $\sim 10^{-7}$ S/cm. Hence, at current densities of 1000 $\mu A/cm^2$, the crystalline film will observe an ohmic polarization ~ 0.056 V while the amorphous film will observe polarization of ~ 0.56 V.

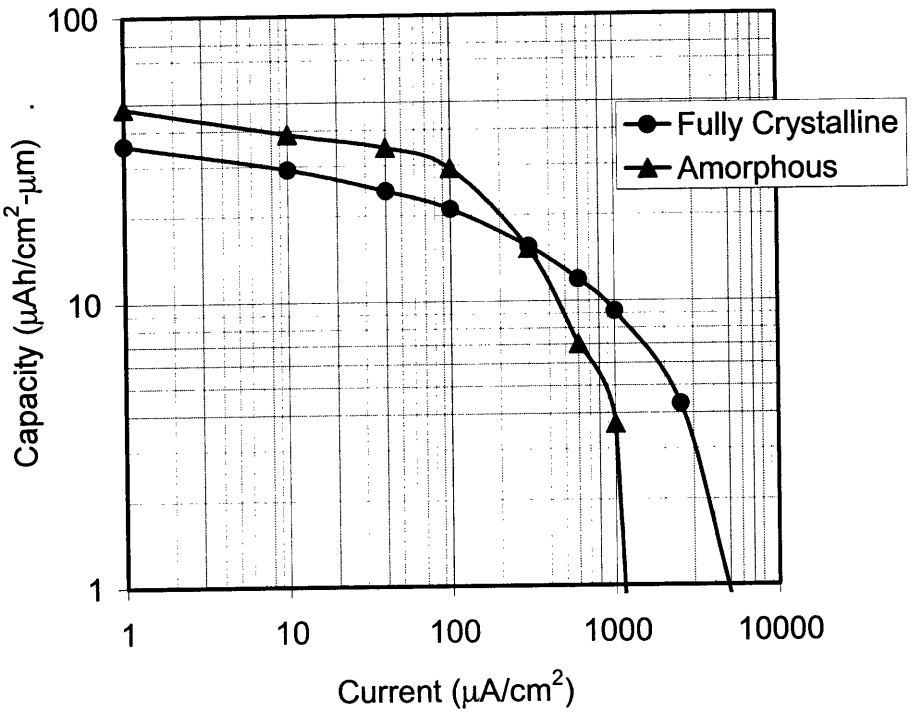

Figure 61: Capacity-rate comparison between HT4 (fully crystalline) and a non-heat treated (amorphous) version of the same film.

Table 12: Calculated polarization associated with film electronic resistance (thickness = 560 nm). Shaded region represents the range of interest.

conductivity (S/cm)	Resistivity . (Ω-cm)	Resistance (Ω)	Polarization (Voltage) (x5.6)				
			1 μA/cm²	10 μA/cm²	100 μA/cm²	1000 μA/cm²	10000 μA/cm²
10^{-5}	10^{5}	5.6	10^{-6}	10^{-5}	10^{-4}	10^{-3}	10^{-2}
10^{-6}	10^{6}	56	10^{-5}	10^{-4}	10^{-3}	10^{-2}	10^{-1}
10^{-7}	10^{7}	560	10^{-4}	10^{-3}	10^{-2}	10^{-1}	1
10^{-8}	10^{8}	5600	10^{-3}	10^{-2}	10^{-1}	1	10

Effects of Thickness

V_2O_5 films of varying thickness on ITO substrates were prepared and evaluated for capacity-rate performance. An earlier study of V_2O_5 films prepared via DC reactive sputtering, which yielded a platelet structure, are discussed in the Appendix but not discussed in this section. Figure 62 displays the results showing the normalized capacities with current rate for thicknesses spanning over an order of magnitude (90 to 1350 nm). At very low currents densities (≤ 1 $\mu A/cm^2$) the capacities are observed to converge towards the theoretical capacity. Thickness related differences are observed even at the lowest current rates. At the lowest rates (1 $\mu A/cm^2$), the ohmic polarization will be negligible between the different thicknesses (see Table 12), so that solid diffusion will be the controlling factor. At rates below 1000 $\mu A/cm^2$, divergence as a function of thickness is observed in the plots, suggesting that the diffusion process dominatese the kinetics of the system. At higher rates, a convergence is observed in the capacity seemingly independent of thickness. Two factors account for this. First, a larger error in the capacity-rate performance is observed at the highest rates, partly due to the discharge time being on the order of 1 second which poses a challenge for data acquisition. Second, interfacial (or charge-transfer) resistance, ohmic contributions, and ionic conduction in the electrolyte will become more significant at higher current rates. The ohmic drop due to electronic resistance in the cathode, however, would be expected to scale with thickness -- an observation not borne out by the results at high current rates. It has also been observed that the electrolyte is capable of managing much higher current densities.[125] The addition of the reference electrode also reduces the potential polarization caused by electrolyte limitations. Thus, it seems more plausible that above 1000 $\mu A/cm^2$, reaction kinetics (or charge-transfer resistance) dominates.

An additional picture of the differences at higher rates is found by comparing the power versus energy for the different thicknesses (i.e. a Ragone plot) as shown in Figure 63. In the Ragone plots, energy and power densities are accounted for whereas the capacity-rate plot measures only the differences in discharge time ($C = I \cdot t_d$)

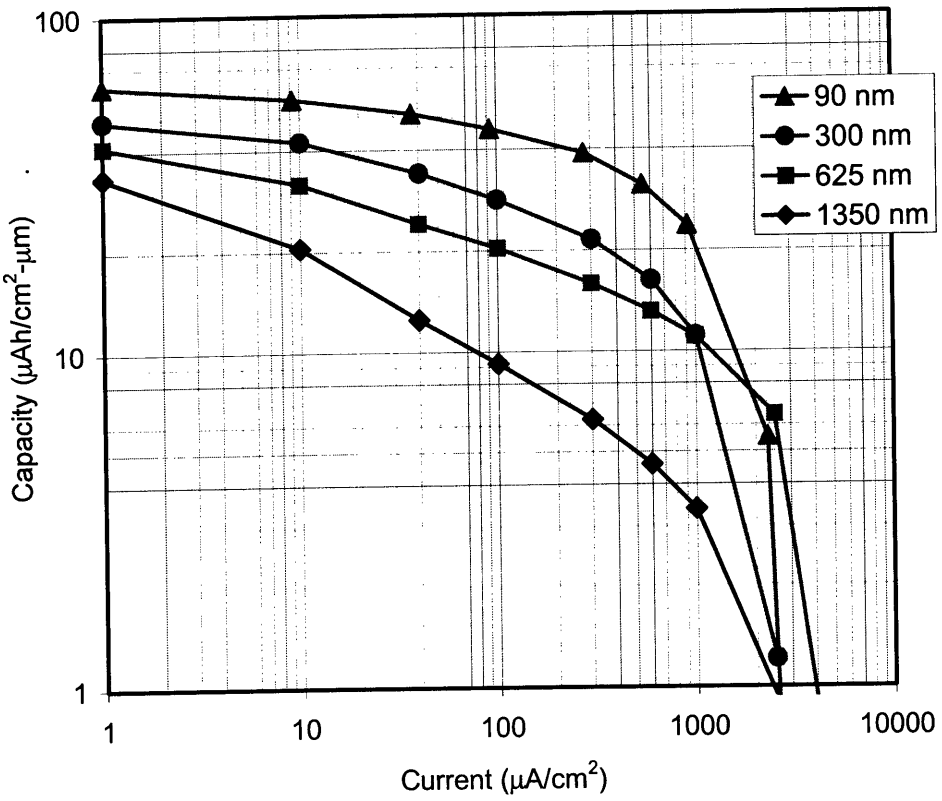

Figure 62: Capacity-Rate Plot of V_2O_5 films of varying thicknesses sputtered on an ITO substrate.

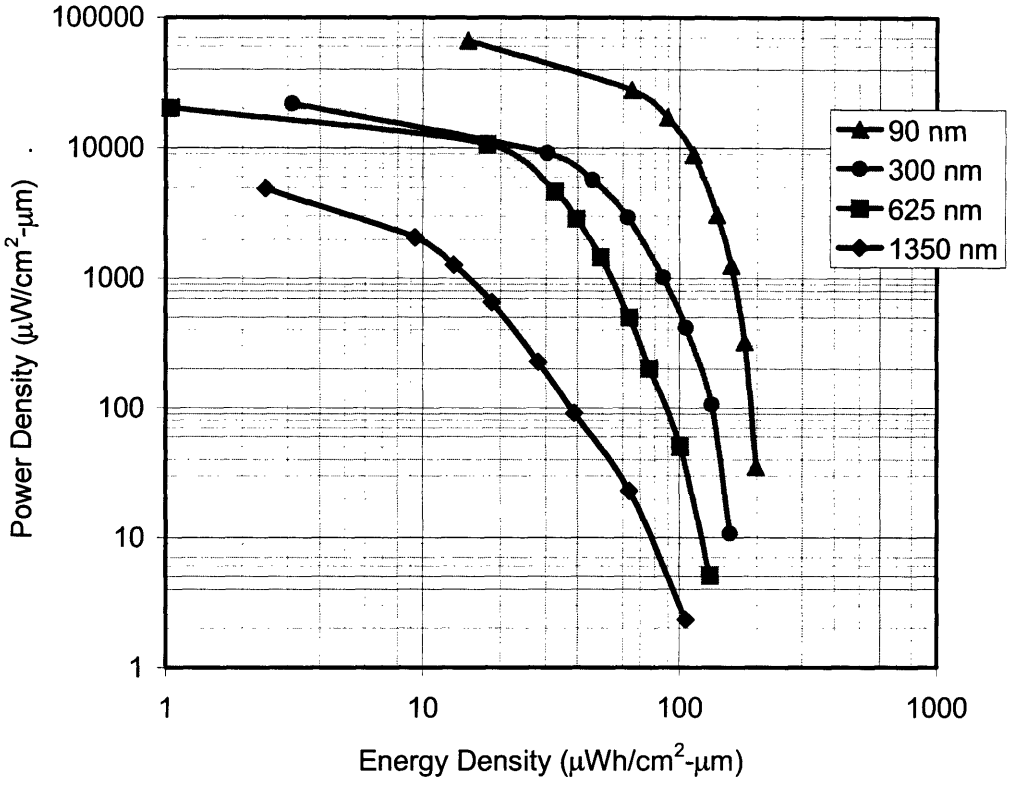

Figure 63: Ragone plot of V_2O_5 films of varying thicknesses.

Data Analysis:

Additional calculations were performed to obtain a Ragone plot (Figure 63) showing the dependence of cathode power and energy density on film thickness. The energy density was obtained by integrating the entire voltage profile over capacity ($E = \int V dq$) while the power density was calculated by multiplying the average voltage and current ($P = I \bullet \overline{V}$). The values were normalized by the area (cm^2) and thickness (μm). As expected, the energy densities appear to converge at very low power densities toward the theoretical energy density. At large power densities, the obtainable energy density is effectively reduced with thickness.

Comparison of the profiles with analytical models by Doyle and Newman (1997) appear qualitatively similar to models assuming the current to be solid-phase diffusion limited.[79] However, the simplified models for a diffusion-limited case yield a linear relationship between capacity and current density, a result not observed in the experimental testing. Instead, a logarithmic decrease in capacity with increasing current is observed. These differences between

the predictions of the model and the observations made in the present study may be due to the inability of a model constructed for porous electrodes to be able to describe the behavior of nearly-dense thin films. Solution-phase diffusion limitations and ohmic limitations (e.g. reaction rate, cell and electronic resistance) both become more prevalent at the larger current rates, meaning the assumptions of the model may not hold for this set of experiments.

To further investigate the performance differences, plots were made of the capacity as a function of thickness (Figure 64). This approach has the advantage of turning the *iR* contribution (from interfacial and cell resistances) into simply a constant offset at each current rate. The plots are remarkably similar for each current rate up to 600 $\mu A/cm^2$, a result that suggests the same physical mechanism (i.e. diffusion) is dominant within this range. Above a rate of 600 $\mu A/cm^2$ (not shown), the slope of the plots begin to approach zero, suggesting that other contributions, such as charge-transfer resistances at the interface, also begin to significantly affect the obtainable capacity.

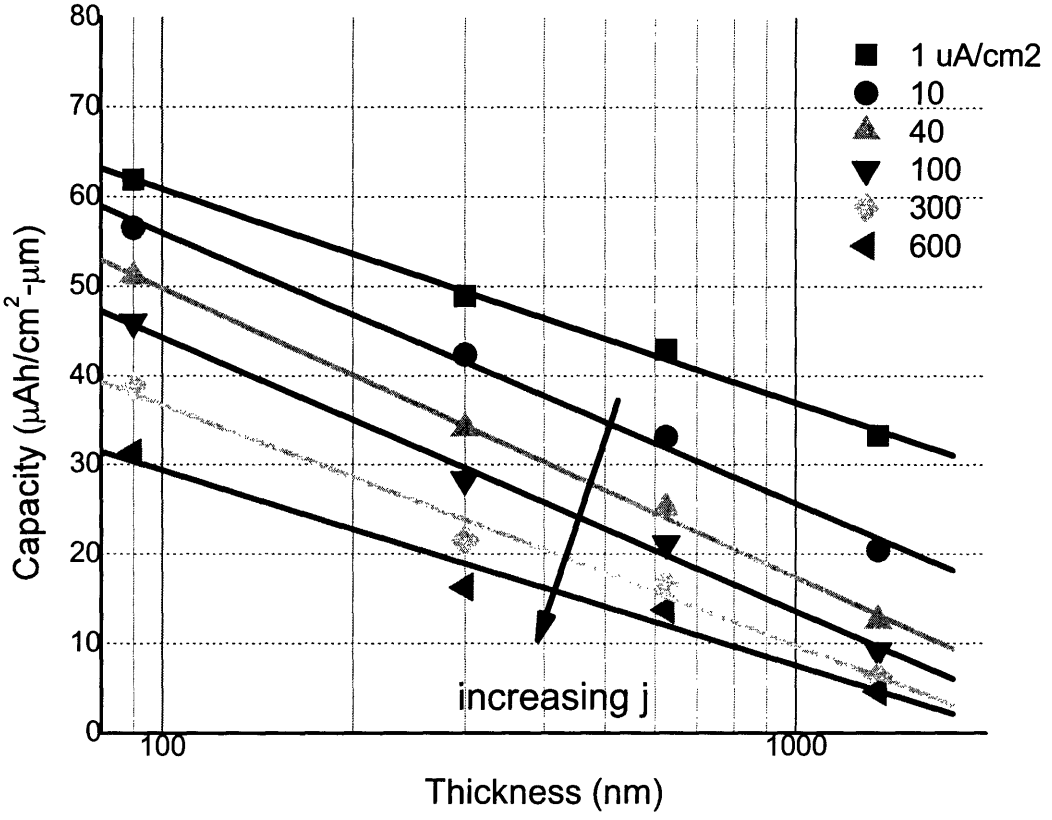

Figure 64: Capacity values with thickness for current density values between 1 to 600 μA/cm^2. Least square linear fit applied for each current density. Arrow shows trend in slope with increasing current density.

A logarithmic fit was applied to the curves in order to derive an equation describing the change in capacity performance with thickness. Equation 24 describes the capacity-thickness relationship as a function of rate

$$C = -m\ln(\ell) + C_o \qquad (24)$$

where C is capacity, m the change in capacity with the natural log of thickness [$\Delta C/\Delta\ln(\ell)$], ℓ the current density, and C_o is a function of current density j and is the capacity as $\ell \rightarrow 0$. Table 13 shows the fit parameter values. In general, m is fairly constant with rate until higher current rates. Above 300 μA/cm^2, the change in capacity with thickness is diminished, and the obtainable capacity becomes less dependent on thickness. Although the $j > 600$ μA/cm^2 are not shown due to the errors and poor fits involved at the very high rates, the curves show the m values

approaching 0 at the limit. That is, the capacity becomes independent of thickness. A transition from a diffusion-controlled to ohmic or reaction-controlled regime would be expected to cause this behavior, as the former is related to thickness and the latter is thickness-independent.

Table 13: Parameter values for least squares fit. j = current density; m = slope of capacity-log thickness plot, C_o = initial capacity

1	10.374	108.61	0.9961
10	13.167	116.61	0.9936
40	14.074	114.61	0.9977
100	13.32	105.59	0.9948
300	11.686	90.468	0.9855
600	9.4711	72.94	0.9699

The term C_o accounts for the effect of j (current density) on the capacity-thickness performance. In Figure 65 below, C_o is shown to be fairly linear with j. Newman and Doyle have shown previously that for solid-phase diffusion controlled systems and for very short discharge times, the relationship between current rate and discharge time is

$$t_d \propto \frac{Da\ell}{j^2} \qquad (25)$$

where t_d is the discharge time, D is the diffusion coefficient of lithium in V_2O_5, a is the surface area, ℓ the cathode thickness, and j the current density. Rearranging terms, the relationship for capacity can be written as

$$C = It_d = jat_d \propto \frac{Da^2\ell}{j} \qquad (26)$$

Note that the C_o values simply represent the limit where t_d is infinitely short (i.e. $\ell \rightarrow 0$). Indeed, Figure 65 shows the relationship between capacity and current rate is an inverse one and linear. While in theory, values for D can be calculated from the data, more accurate approaches are used to evaluate D and are discussed elsewhere in the thesis.

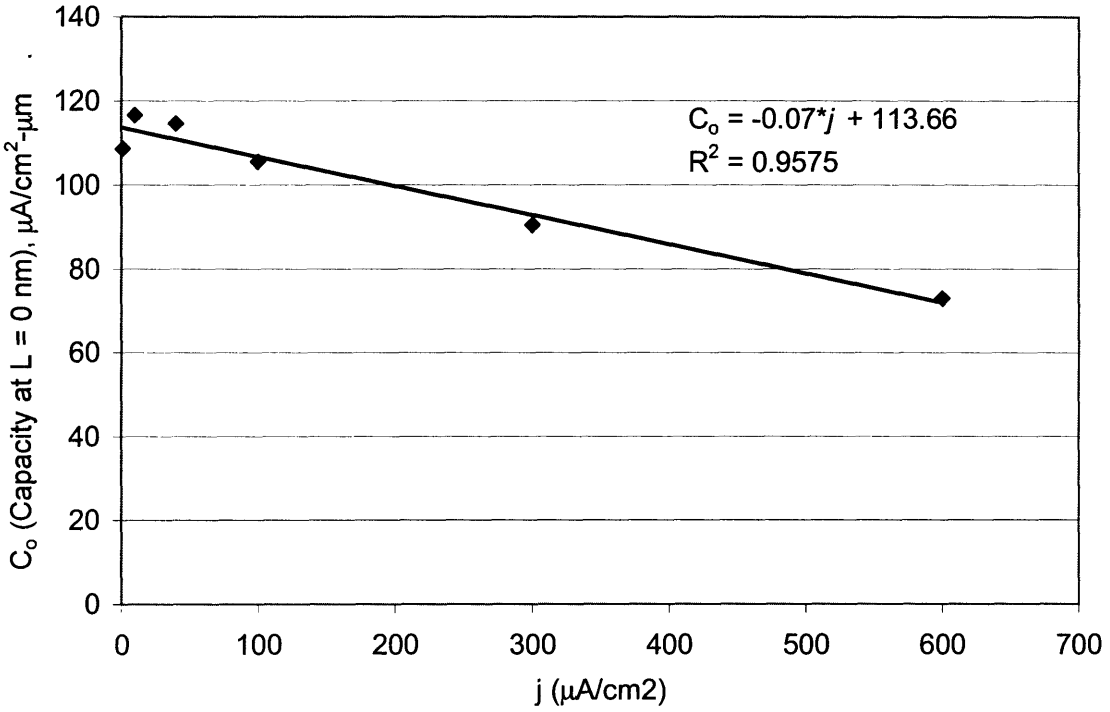

Figure 65: Plot of Co capacity values (at ℓ = 0 nm) as a function of current density. Least squares fit shown with equation.

In practice, the C_o values should not be considered as a theoretical capacity but simply as an offset parameter that accounts for the effects of current density. The limits of the above model are apparent if one considers that C_o will always be bounded in practice by the theoretical capacity. Even as thickness approaches zero, there still always exists double-layer charging which manifests itself as capacitance. As the thickness diminishes, this double-layer capacitance becomes an increasing fraction of the measured capacitance. Instead, C_o displays how quickly the capacity-thickness curve is pushed downward with increase current rate. In the case of V_2O_5 thin films, the linear fit in Figure 65 shows that the capacity will be lowered by ~ 7 μAh/cm^2-μm for every 100 μA/cm^2 increase in current density.

In summary, the capacity was found to diminish at a rate of about 12 ±2 μAh/cm^2-μm for a change in thickness by a factor of e (i.e. 2.718).[9] The kinetics were also observed to switch

[9] The slope m represents $\Delta C/\Delta \ln(\ell)$. In order for the denominator to be unity, $\Delta \ln(\ell) = \ln(\ell_1) - \ln(\ell_2) = \ln(\ell_1/\ell_2) = 1$. Thus $\ell_1/\ell_2 = e$ or $\ell_1 = 2.718\ell_2$.

from diffusion controlled to a reaction-controlled or ohmic-controlled regime above ~ 600 $\mu A/cm^2$. The analysis developed herein demonstrates the usefulness of obtaining the values of m and C_o in order to optimize the capacity performance. These parameters can also be obtained for other thin film cathode material systems and used to tailor the battery design for specific current and power requirements.

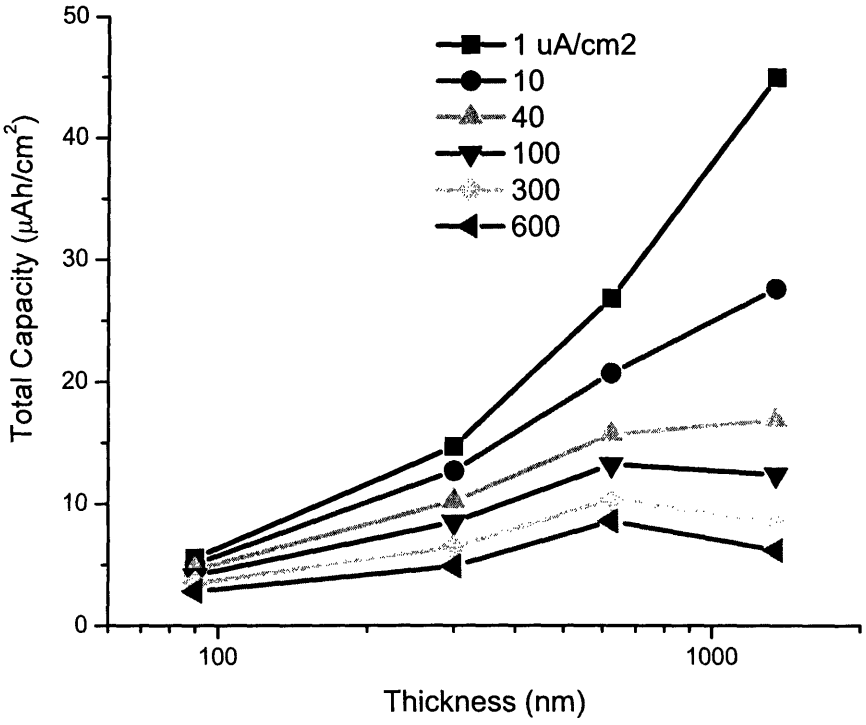

Figure 66: Total obtainable capacity ($\mu Ah/cm^2$) as a function of thickness.

Another metric that can be used in the selection of cathode film thickness is the overall capacity normalized for geometric surface area [$\mu Ah/cm^2$] (Figure 66). It can be observed that for current rates at or above 100 $\mu A/cm^2$, the obtainable capacity reaches a maximum between 600 -1200 nm. Therefore, for applications where higher power is necessary, increasing the film thickness (or active mass) far beyond ~ 0.5 μm offers no advantage. Further increase beyond this thickness range actually leads to diminishing returns in terms of overall, obtainable capacity (or energy).

Comparisons of Capacity

Among the questions that arise from the analysis is how thin film V_2O_5 systems compare against other thin film material systems and architectures (e.g. sol-gel, nano and bulk composites, fiber or brush electrodes). Interestingly, a review of literature reveals that the reported performance diverges tremendously (over two orders of magnitude) despite the material system being the same. Dudney *et al.* (1995, 2003) explored the capacity-rate performance of thin film $LiCoO_2$ cathode systems and V_2O_5.[15, 47] The power density of the films, in comparison with the V_2O_5 films shown here, are similar as observed in Figure 67 (note that the energy density is lowered because of the degree of lithiation and the different materials system used). The results also appear similar to thin film V_2O_5 results observed by Park *et al* (2002).[126] Extrapolating data based on their discharge curves yields approximately 42 and 22 $\mu Ah/cm^2$-μm at rates of 10 and 250 $\mu A/cm^2$ respectively for the voltage range considered herein (2.5-4V).

In comparison, powder systems largely exceed the current rate capability of thin film batteries on a geometric area basis (i.e. $\mu A/cm^2$). Current densities between 1-15 mA/cm^2 are commonly reported for these composite systems.[127] Considering very high surface area cathodes (i.e. nanofibers), Martin and Patrissi have reported rate capabilities upwards of 250 mA/cm^2 (geometric area) for fibrils (*sic*) of ~ 250 to 700 nm in diameter. The nanofibers, prepared using a template synthesis method involving porous alumina, were oriented perpendicular to the substrate.[125, 128-130] Figure 68 reproduces the current rate performance reported by Martin and Patrissi (2001). The fibrils are shown to be capable of remarkable current rates of over 5000C. The divergence in the current density limits span over two orders of magnitude (from ~ 2 to 250 mA/cm^2). It is shown here that this divergence is not the result of material property differences, but rather the use of inappropriate metrics for current density.

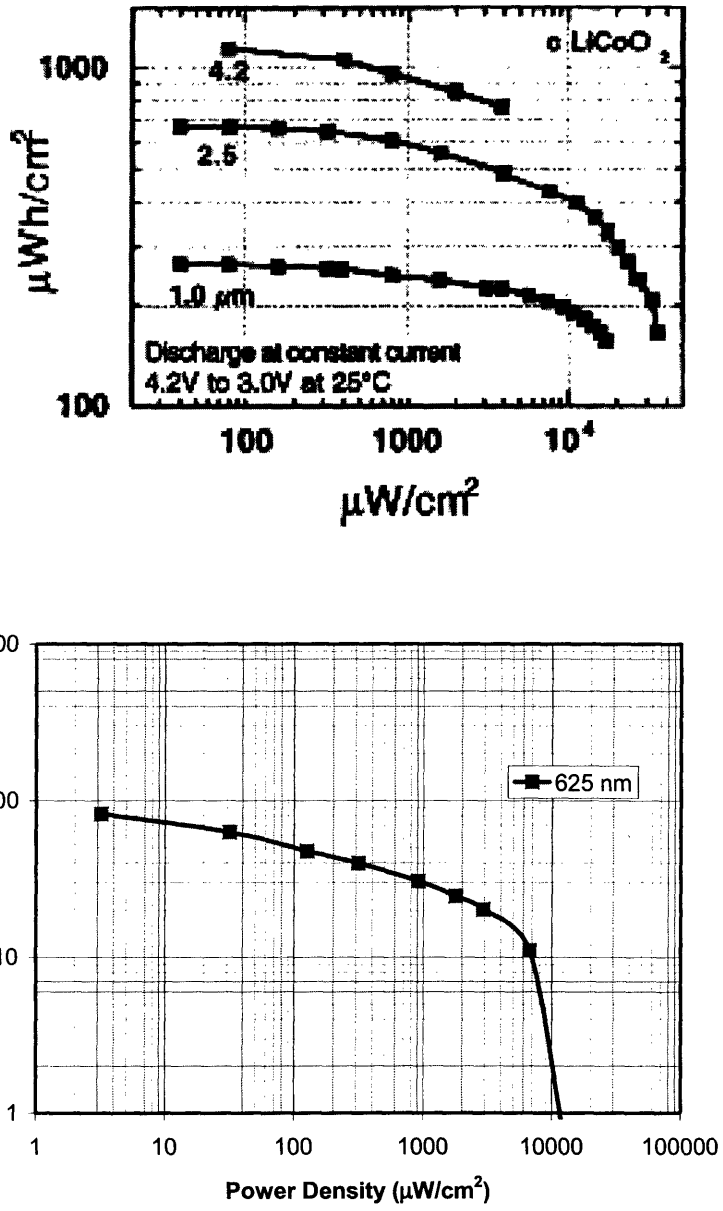

Figure 67: Comparison of capacity rate of (top) $LiCoO_2$, reproduced from Dudney (2003) and (bottom) V_2O_5 prepared in our labs. Change in energy density attributed to film thickness, material system, and voltage limits.

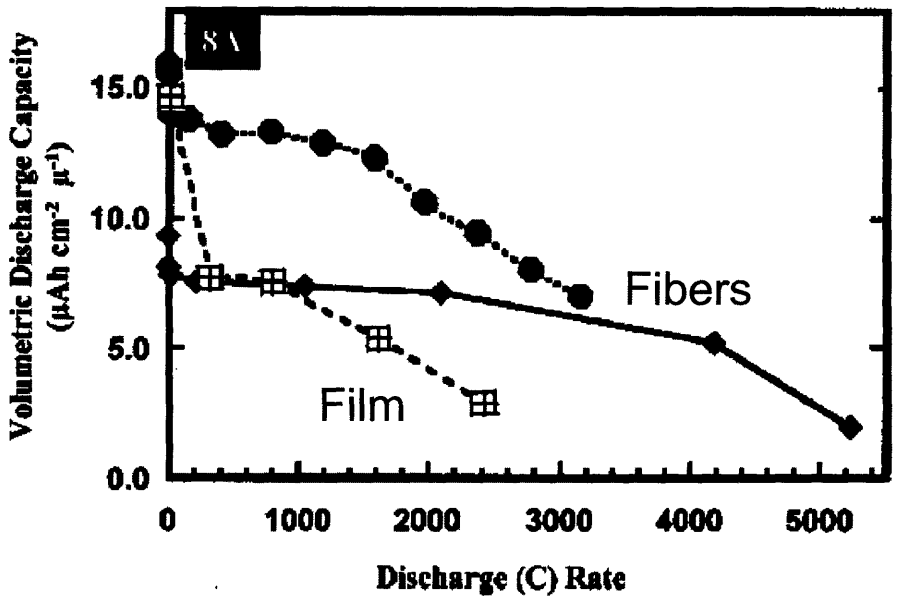

Volumetric capacity *vs.* discharge rate. (A) (♦) e50-nm, (●) e400-nm + TIVO, (⊞) thin-film. (B) (♦) e400-nm, (●) e400-nm + TIVO, and (⊞) thin-film.

Figure 68: Reproduction of C-rate graph from Patrissi (2001).[125] Numbers refer to fiber size and TIVO refers to the application of a sol-gel on the surface to increase the volumetric density of the fibrous material. A 1C current rate is defined as the current to lithiate the sample to the theoretical capacity (142 mAh/g) in 1 hour.

Definitions of Current Density:

Three definitions of current density are discussed here, the first two of which are the most widely used in the battery research field. They are: *C-rate*, geometric current density, and effective current density. The most popular current density, *C-rate* or (*C/n*), is defined as the current rate needed to drain the rated capacity of the battery (*C*) in *n* hours. Thus, if the batteries capacity is drained in ½ an hour, one has presumably used a *C-rate* of *C/0.5 = 2C* current rate. Higher *C-rates* translate to higher current densities (i.e. 10C = 10 x 1C). The *C-rate* is often used within the industry when reporting rate-performance data. Since the theoretical capacity of the battery is based in part on the (1) mass of active material and (2) amount of lithiation (i.e. determined by the operating voltage window), this term is dependent on both the battery geometry as well as the operating conditions. For a $Li_xV_2O_5$ cathode ($0 \leq x \leq 1$) and weighing

0.5 g , *C* would be defined as [theoretical capacity/unit weight] X [weight of active mass] = [147 mAh/g] X [0.5 g] ~ 73.5 mAh. Since *C* is really proportional to the weight used, the *C-rate* is actually equivalent to defining a gravimetric current density [mA/g]. Graphs using *C-rate* would appear identical to graphs reporting units of [mA/g].

The second most commonly used metric is the geometric current density [mA/cm^2 cathode area]. The term accounts for only the geometric cross-section of a cathode. This metric is useful from a product design standpoint because it allows one to access the drain rate possible from a manufactured battery. While the cross-sectional area of a cathode is easy to define, the actual current density observed by the active material relates to the effective area (i.e. total surface area). Thus, the metric is a poor choice for studies investigating transport phenomena, comparing different architectures, or accessing the rate limiting steps.

The proposed metric to use for the studies is the effective current density. This more precisely defines the current drain rate with respect to the area of active material, termed the effective area. For a smooth thin film, the effective area will be close to the geometric area. For any other system, however, the effective area will be *greater* than the geometric area.

Examples:

The following examples attempt to show how the performance converges for different architectures once the effective area is considered. Consider a typical composite cathode with the following properties

- 2 cm^2 cross section
- 50 mg of material (85 mass % V_2O_5)
- 50 μm diameter spherical powder

and compare this to the same sample made with 50 nanometer particles under a current drain of 10 mA/cm^2 (geometric area). The parameter values were input into a spreadsheet model developed to calculate the effective surface area and various metrics of current density. These results are shown in the Appendix. The surface to volume ratios are shown as a function of particle size in Figure 69. The effective current densities are compared to the geometric current densities for the two particle sizes in Figure 70. The effective current density is shown to be much lower than the geometric current density (Table 14) particularly for the nanoscale particles.

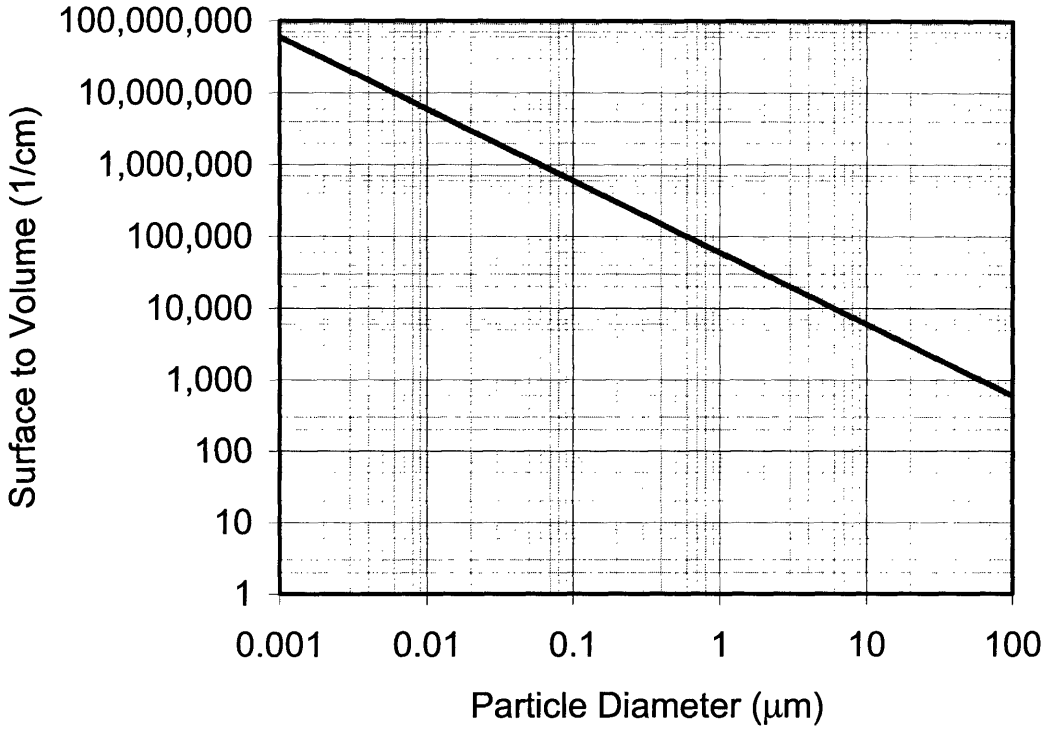

Figure 69: Surface area to volume ratio as a function of particle diameter.

Reported values of 10 mA/cm^2 for the cathode with 50 μm particles should, on an effective area basis, be lowered to 1.31 mA/cm^2. This difference is even more significant for nanoscale based electrodes. In the case of a 50 nm diameter powder, the reported 10 mA/cm^2 should be lowered to 1.31 ***μA/cm^2*** (emphasis added). Unfortunately, the use of the geometric based metric is pervasive through literature. From a transport perspective, the effective area is the relevant parameter that should be used.

Table 14: Gravimetric versus Effective Current Densities

D (μm)	Gravimetric (mA/cm^2)	Effective (mA/cm^2)
0.05	10	1.31×10^{-3}
50	10	1.31

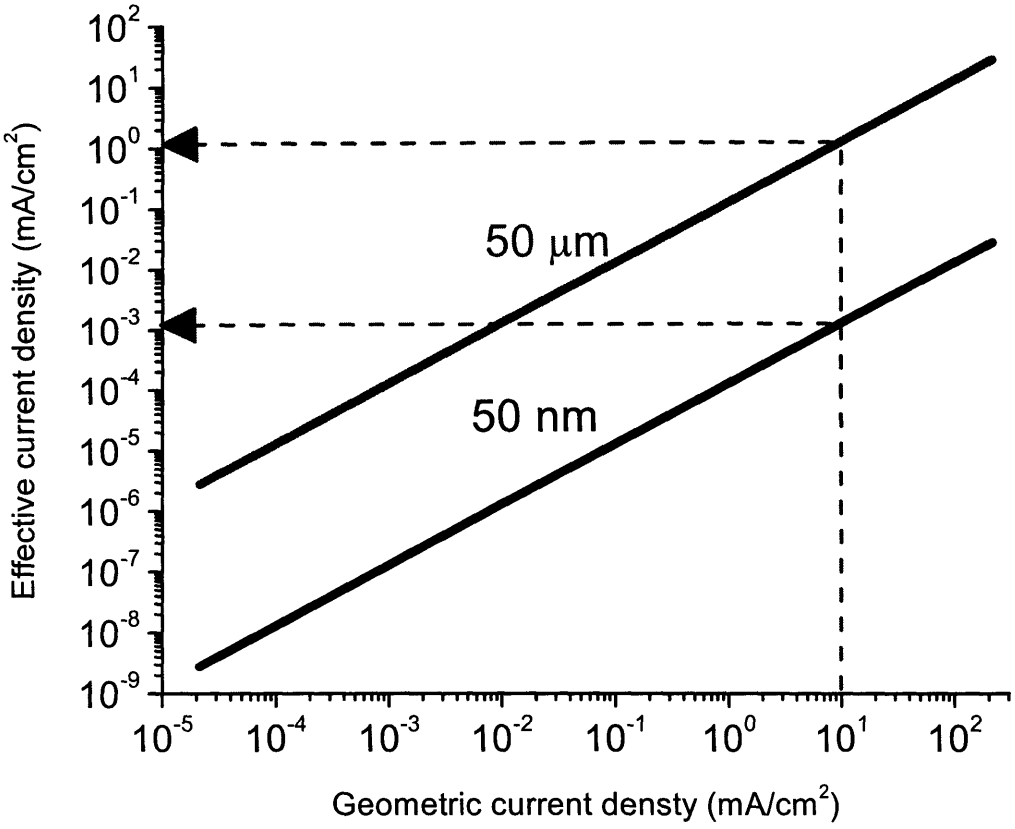

Figure 70: Effective versus geometric current density for two particle sizes.

Next, the case of the nanofiber electrode is considered, as shown in Figure 68. Martin and Patrissi (2001) did not report the effective area of their cathodes, which might have been experimentally difficult to verify.[131] They did compare the rate capabilities of their electrodes on a per unit mass basis and provided enough information regarding the mass and geometry of their nanofiber structure to estimate the effective area. The surface area of their cathodes is assessed here by using the sample descriptions reported in their work. Assuming their reported values of

- 250 nm diameter fibrils
- 5 μm thick electrode
- electrode mass loading of 326 μg

One finds that the fibrils would need to be spaced approximately 0.5 μm apart. An effective surface area of 16 cm^2 (48500 cm^2/g) is obtained for an electrode 1 cm^2 in geometry. The high c-rate of ~ 5000C (~250 mA/cm^2 geometric) as cited above falls sharply to 15.7 ***mA/cm^2*** (effective).[10] This current density limit is within an order of magnitude of the capacity rate limits reported for the thin film systems herein. Interestingly, if one now normalizes the comparison graph shown in Figure 68 in terms of effective current density rather than C-rate, the curves show great similarity. This is shown below in Figure **71**.

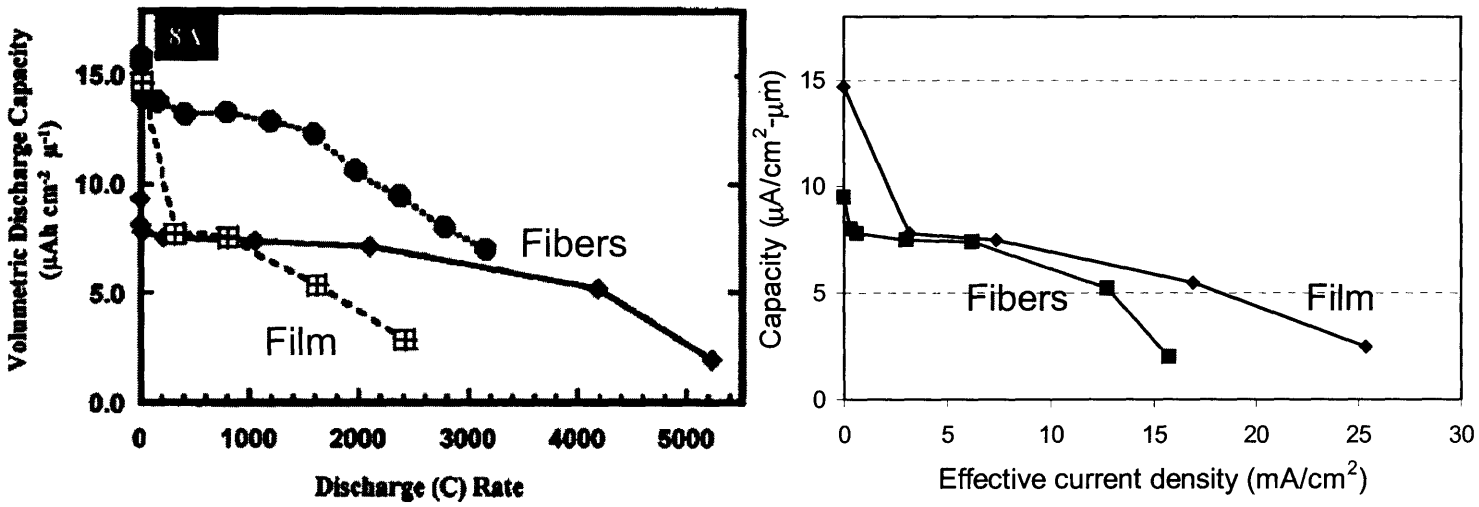

Figure 71: Comparison of fiber and film electrode (left) as reported using C-rate or mA/g and (right) using effective current density. Note that only two series were graphed on the right. Left graph reported in Patrissi and Martin (2001).[131]

This analysis suggests that the capacity rate performance is largely similar (slightly better for the film), *despite* diffusion length-scales of 2.3 μm for the thin film and 125 nm for the fibers, a difference spanning over an order of magnitude. Thus, a surface reaction rate or interfacial resistance governs the performance, similar to the results shown herein. Reporting the current

[10] The *C-rate* or *C/n* represents one measure of the specific (or gravimetric) current density. *C* represents the theoretical capacity of the electrode (i.e. how much lithium can be intercalated) while the *n* represents the time to drain the battery. Because *C* is defined in terms of a gravimetric theoretical capacity (mAh/g), the *C-rate* effectively has units of mA/g. This term is problematic however, because the theoretical capacity depends in part, on the voltage limit which is an experimental parameter.

density in terms of the *effective* area results in a convergence of the capacity-rate performance between thin films, composites, and nanofibers. This observation would also suggest that diffusion length-scales may not necessarily be the limiting factor, but rather the interfacial step and/or reaction rates. Based on the above results, the advantages currently observed in V_2O_5 systems incorporating nanoarchitectures appear to be trivial size effects, as described by Maier (2002, 2003).[132-134] Maier states that trivial size effects are those based "solely on the increased surface-to-volume ratio" compared to "true-size effects" (or quantum effects) that rely on "changes of local material properties."[133].

Summary

Variations in the grain size distribution of thin film cathodes appear to lead to limited changes in battery performance. It was suspected that the presence of additional grain boundaries would allow for fast diffusion and result in improved electrochemical performance. However, a range of GB volume between 2.5-7% did not result in significant differences. Changes in the crystallinity of the film, however, did significantly affect performance. Amorphous V_2O_5 films, reported to have higher diffusion coefficients than crystalline V_2O_5, were measured to have lower electronic conductivity in chapter 4. This lower conductivity value became a significant overpotential above 300 $\mu A/cm^2$, resulting in poorer performance compared to fully crystalline films.

Thickness studies of films also revealed that more than one mechanism is dominant over the range of currents used in the capacity-rate experiment. At the lowest current rates, diffusion is dominant while at the higher rates, polarization from reaction and/or ohmic limitations become dominant. Analysis of the data shows the rate at which capacity diminishes by increasing thickness is ~ 12 ±2 $\mu Ah/cm^2$-μm for a change in thickness by a factor of *e* (i.e. 2.718). If the cell is used at even moderate current rates, increasing thickness to obtain higher energy provides no benefit. From an analysis of other electrode systems (composite and nanofibers) reported in literature, it appears that similar reaction rate limitations are observed once the *effective* surface areas are taken into account. The findings suggest that the advantages observed for nano-architecture systems are based purely on increased surface to volume ratios rather than on true-size effects.

Chapter 7: Kinetic Parameters for V_2O_5 battery systems

AC Voltammetry Technique

Experimental:

Thin film V_2O_5 sputtered on ITO coated substrates were assembled into three-electrode cells containing lithium metal for the reference and counter electrodes. A typical liquid electrolyte was used (1 M $LiPF_6$ in EC:DMC, Merck GMBH Industries). In general, working electrode areas measured ~ 1 to 1.5 cm^2. Solartron impedance analyzers and potentiostats were used together in coupled mode and were both controlled using Zplot software (Scribner Associates). In Appendix A, the setup is described more completely. In summary, a forward and reverse sweep of the DC potential was taken at a rate of 25 μV/s between 3.7V to 2.9V Li. The magnitude of the AC bias was |10 mV|, with data points taken every 5 mV.

Results:

Figure 72 is the AC voltammagram of a typical V_2O_5/ITO thin film system for frequencies from 0.05 to 5 Hz. Higher frequencies are subsequently discussed. It was observed that $|I_{ac}|$, I', and I'' increase with frequency as expected. The forward and reverse peaks, as expected using ACV, are split largely because of activation overpotentials (i.e. sluggish electron transfer), with the standard potential, $E^{o\prime}$ located between them.

The baseline also is observed to increase, reminiscent of scans obtained by DC cyclic voltammetry. This is particularly true for the out-of-phase, ac harmonic current (Figure 72b), which lags E_{ac} by 90° and is indicative of capacitive contributions. In DC voltammatry, the effects of the charging current and uncompensated resistance lead to a background current (i.e. $|i_c| = AC_d\nu$, where A = area, C_d = double-layer capacitance, ν = sweep rate). It is unclear here though why the baseline increases despite the sweep rate being fixed. This changing background is attributed to the effects of other processes occurring within the electrode, as discussed earlier, not accounted for by traditional electrode theory. For instance the double layer charging at the surface is observed increase with frequency. Rapid fluctuations at the surface would be expected

to occur differently if there is also a "sink" for these ions, i.e. diffusion into the solid, an effect found for all lithium intercalation compounds. These chemical and electrode complications can lead to different instantaneous ion concentrations at the surface from those at a metal electrode.

Bond et al. (1976), an early pioneer of applied ACV, stated that for non-nerstian DC behavior, "one observes that the ac wave shape, position, and magnitude can depend markedly on scan rate, scan direction, number of preceding scans, the switching potential, the initial potential, and electrode sphericity."[96] This comment suggests that familiar, well-established data analysis procedures in ACV may not be as applicable to evaluating the constants in cathode materials if other complex mechanisms also occur. However, this background – despite its uncertain causes – can be removed so that the peak height is evaluated relative to this background. This is the method normally applied in previous ACV experiments.[96] Unless otherwise stated, this procedure has also been performed here.

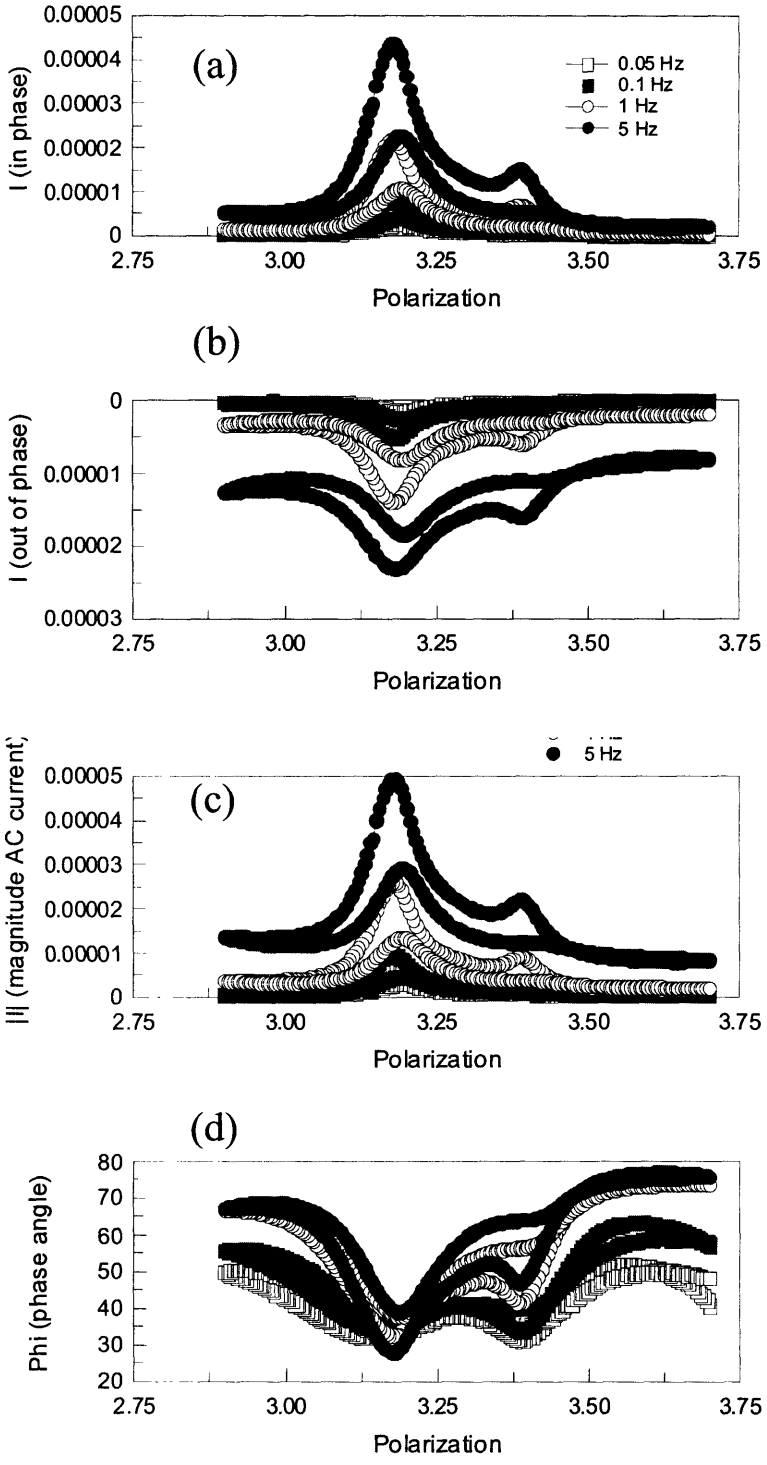

Figure 72: (a) I'ac, (b) I''ac, (c) |I|ac, and (d) φ from AC voltammetry between 2.9 to 3.6V vs. Li

The fundamental peak currents as a function of $\upsilon^{1/2}$ are shown in Figure 73 (note that the background current was removed). The magnitudes were observed to initially increase with frequency followed by a decrease or plateau. In a reversible system (i.e. rapid kinetics, slow diffusion), $|I|_{fundamental}$ should be proportional to $\upsilon^{1/2}$. However, in the quasi-reversible or irreversible case (i.e. slow kinetics), the magnitude becomes independent of υ as the system becomes completely controlled by heterogeneous kinetics.[92]. This may explain the behavior observed in the higher frequency domain.

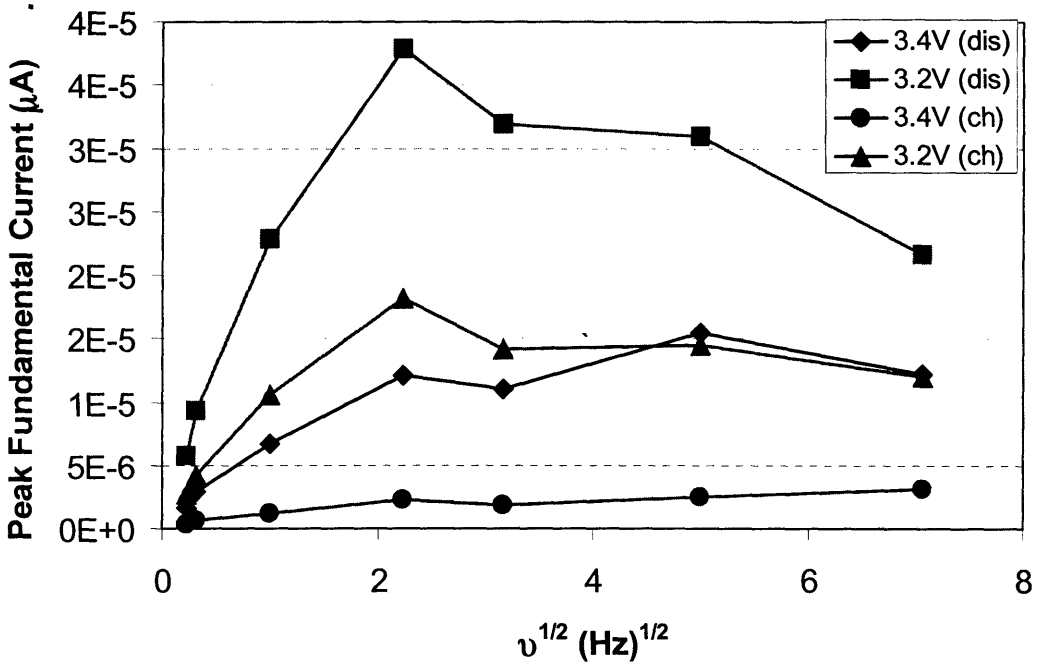

Figure 73: Peak fundamental current (background removed) as a function of frequency. The 3.4V and 3.2V plots are plotted for both the forward (discharge) and reverse (charge) sweep.

The behavior of the phase angle with frequency was explored through plots of the maximum cotφ with $\upsilon^{1/2}$, displayed in Figure 74.[11] As discussed in chapter 3, information of the transfer coefficient and k^o can be derived in theory with the phase angle information. However,

[11] Note that only for peak magnitude calculations was the background removed. For phase angle determination, the original phase angle measurements were used.

as can be observed, the expected linear behavior between the two parameters is questionable (the intercept should be unity at $\upsilon \rightarrow 0$. To explore the cotφ - $\upsilon^{1/2}$ relationship further, further samples were prepared and tested at higher frequency ranges. However, above frequencies of 1000 Hz, the behavior of the fundamental harmonic currents (|I|) changed so that positive peaks were not observed, but rather negative peaks where positive peaks would always be expected. This is shown in Figure 75(a) below. Additional increases in frequencies toward 500,000 Hz worsened both the peak resolution and the expected behavior.

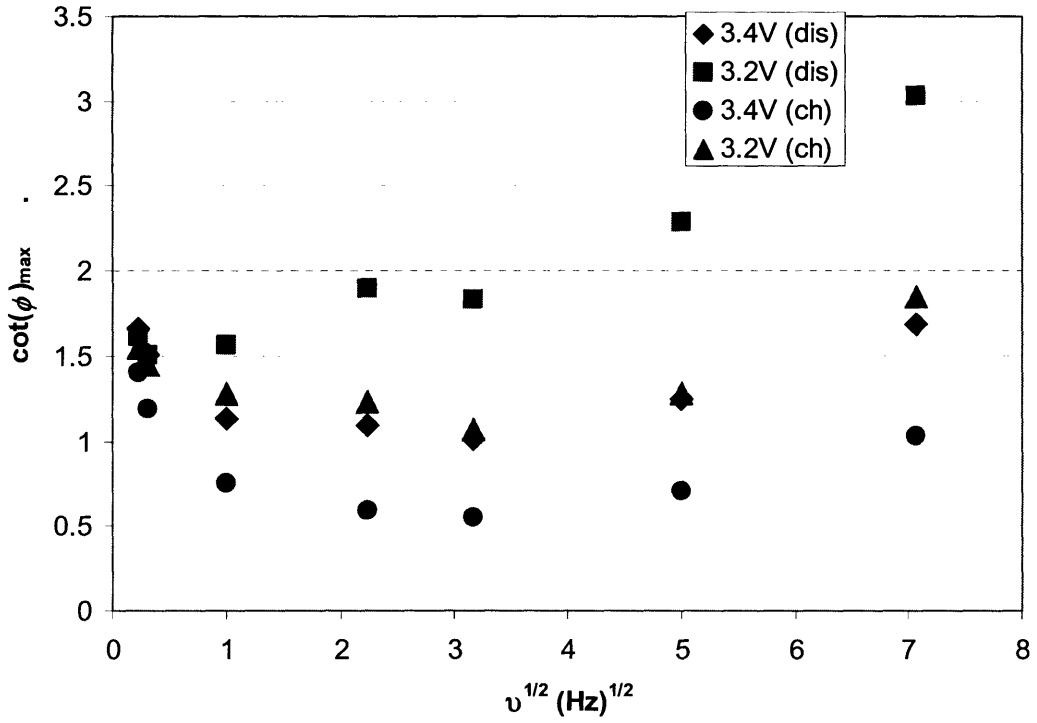

Figure 74: cot(φ) vs. $\upsilon^{1/2}$ for the V_2O_5.

At lower frequencies (< 10 Hz), it appears that solid diffusion effects are still present in the response as evident by the initial increase in I_{peak} with $\upsilon^{1/2}$. Above this range, reaction kinetics become accessed as evidenced by the *cot(φ)* versus $\upsilon^{1/2}$ curves and the relative independence between I_{peak} and $\upsilon^{1/2}$. At ranges $\geq$ 500 Hz, additional effects express themselves as a loss and actual reversal of the in-phase, fundamental harmonic current (i.e. a dip instead of a peak). This latter effect has not been previously reported or discussed in analytical models. In addition, there has been a resounding silence in literature with regard to ACV analysis of battery materials. It is

suspected that during mid-range frequencies, several processes may be accessed include the passive film interfacial resistance, charge-transfer, and even the substrate/film resistance.

At the highest frequencies (> 10,000 Hz), the presence of the peaks on the forward scan appears well distinguished. Upon the reverse scan, no peaks are present however and the response is flat as shown in Figure 75(b). It appears that the process of removing lithium from the cathode during the reverse scan is affected strongly by the application of very rapid AC perturbations. Alternatively, the k^o associated with the reverse scan may be low enough to suppress the presence of a measurable harmonic current.

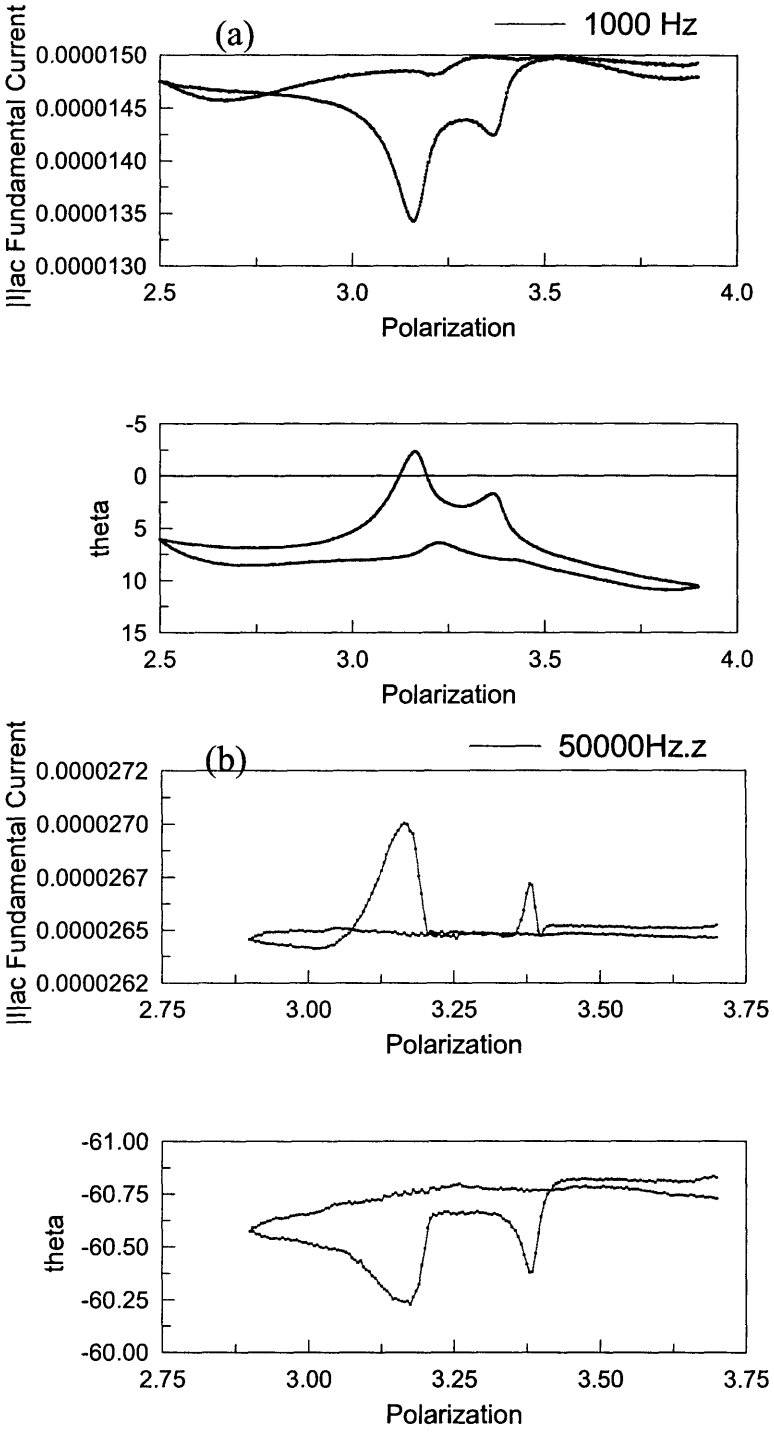

Figure 75: Fundamental harmonic ac cyclic voltammagram at high frequency showing (a) negative peaks during scans (1 kHz) and (b) presence of initial peaks during forward scans and absence of peaks during the reverse scan (50 kHz).

Two additional types of measurements were performed using (1) a very-thin film of 90 nm thickness and (2) second harmonic ac cyclic voltammagrams. The first was used to reduce the effects of solid state diffusion, which was believed to add complexity to the results of the AC voltammagram. The use of second harmonics was used to separate the faradaic impedance contributions from those of the solution resistance and double-layer capacitance. The latter was measured to be high in the system based on the current background. Unfortunately, neither approaches appeared to improve the results shown herein. The second harmonics ac voltammagram gave unusable results, although the fundamental harmonics ac voltammagram (produced in between scans) produced results similar to those shown here.

Attempts were made to calculate the transfer coefficient based on the cross-over potential, E_{co}, in an approach first set forward by Bond et al. (1976).[96] However, a crossover potential was present only for the peak located at ~ 3.4V (see Figure 72c). Values for the half-wave potential, $E_{1/2}$, and E_{co} were identified for several frequencies, as shown in Table 15. The transfer coefficient for the $\alpha \rightarrow \varepsilon$ reaction was consistently calculated as 0.90 ±0.05 for the different frequencies. This value suggests that there exists a large asymmetry with the energy barrier for the forward versus reverse reaction at 3.4V.

The ratios of the forward peak and reverse peak current were also considered, $|I_f| / |I_r|$ as shown in Figure 76. Interestingly, the peak separation is low enough to remain in the reversible case, but the values of $|I_f| / |I_r|$ are approximately 5 and 2 for the 3.4V peak and 3.2V peaks, respectively. This large difference in peak potential also supports the transfer coefficient deviating largely from 0.5, a value which represents a symmetric energy barrier for forward and reverse reactions.

Using the value for the transfer coefficient, together with the slope of the $cot(\varphi) - \upsilon^{1/2}$ relation (avoiding the lower frequency points), the heterogeneous rate constant was calculated, albeit only for the 3.4V peak for the same reason discussed above. The value for k^o was calculated to be ~ 1.9 x 10^{-6} S/cm. Note that $\widetilde{D}_{Li^+}$ the diffusion coefficients for the forward and reverse reactions was taken to be equal and estimated as ~ 10^{-13} cm^2/s. Also note that the k^o values could vary by an order of magnitude depending on the values selected for $\widetilde{D}_{Li^+}$. Rate constants for V_2O_5 were unavailable in literature, although the results are comparable with other lithium intercalation compounds. Deiss et al. (2001) reported k^o values of 5.5 x 10^{-8} cm/s for

$LiMn_2O_4$, while Krtil (2001) and Lindstrom (1997) et al. measured k^o values of $1x10^{-8} - 4x10^{-10}$ cm/s and 3.5×10^{-10} cm/s respectively.[135-137]

Table 15: Values for calculation of transfer coefficient,α

v (Hz)	E_{co} (V)	$E_{1/2}$ (V)	α
5	3.475	3.405	0.94
10	3.455	3.410	0.85
25	3.468	3.405	0.92
50	3.456	3.410	0.86

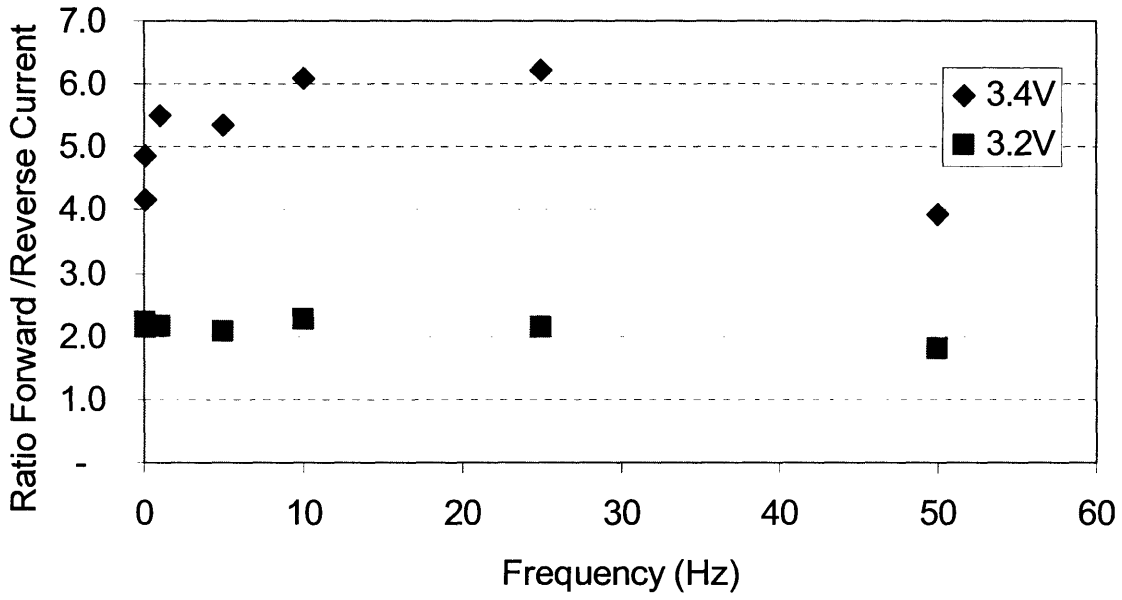

Figure 76: Ratio of Forward: Reverse Current Peak with Frequency

Slow Scan Rate Cyclic Voltammetry

Results:

A film of V_2O_5 sputtered on an aluminum substrate was studied by slow scan rate cyclic voltammetry (SSCV), a technique discussed earlier in chapter 3. [93, 138-140] A series of potential sweeps performed between 3.9 to 2.5 volts at rates between 0.025 to 10 mV/s. Three of the

slowest scans are shown in Figure 77 with peaks pairs I and II labeled. The subscript "a" and "b" denote the anodic and cathodic sweeps.

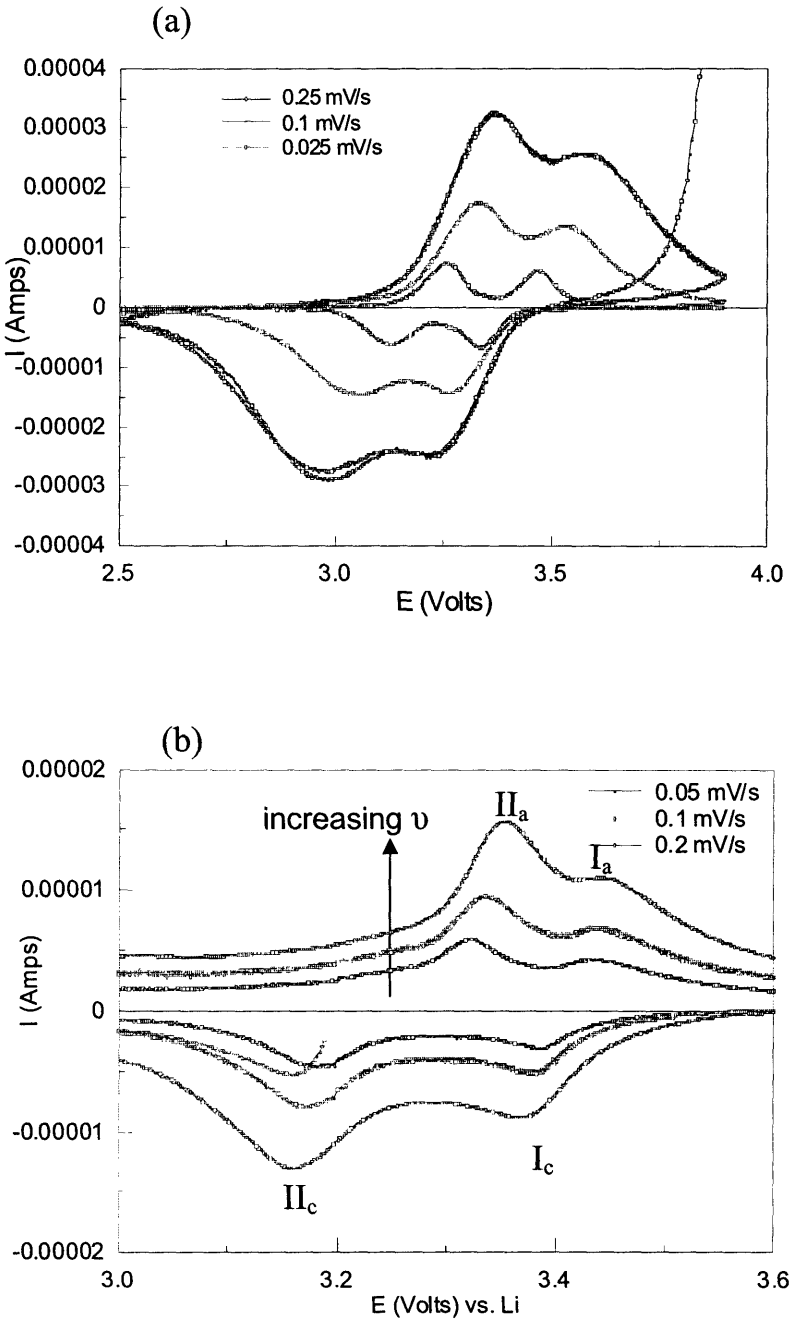

Figure 77: Slow scan rate cyclic voltammetry on two V2O5/Al films (a) showing peak separations with increasing scan rate and (b) showing the cathodic and anodic peaks labeled.

The peak positions and magnitudes were identified and mapped. In general, the 3.216V cathodic peak was the most resolvable peak; the magnitude is shown below in Figure 78 as a function of the square of the sweep rate, $v^{1/2}$. However, other peaks also showed a similar trend (not shown). At larger rates (>5 mV/s), the peaks become difficult to resolve and are thus not included. Figure 78 clearly shows the linear relationship that is evidence of a diffusion controlled system. A linear fit applied to Figure 78 and forced through the origin is shown to fit reasonably well. The exponential on v is measured as 0.543 which is very close to the $v^{1/2}$ relation describing the diffusion controlled case.

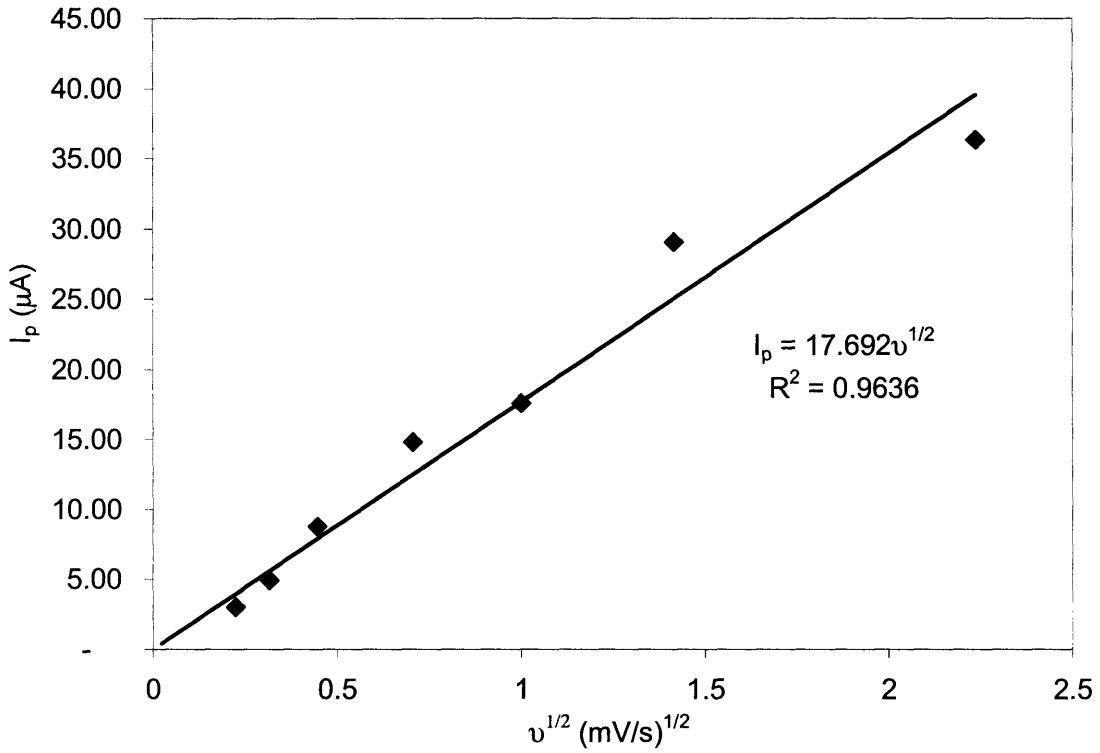

Figure 78: Results from a series of slow cyclic voltammagrams illustrating the cathodic peak height at 3.216V versus the sweep rate. V_2O_5/Al sample.

In general, the anodic and cathodic peaks are in a quasi-reversible state and do not show all the qualities typical of a reversible system, namely (1) independence of E_p with v, (2) separation of corresponding anodic and cathodic peaks (ΔE_p) by $59/n$ mV, and (3) $I_{p,\,anodic}/I_{p,\,cathodic} = unity$. Only for peak I is condition (2) met, and only at the lowest potential sweep rates

(0.05 and 0.1 mV/s), with ΔE_p values of 43 and 59 mV respectively. For a quasi-equilibrium process, the standard rate constant can be estimated based on the dimensionless parameters, α (transfer coefficient) and ψ, a kinetic rate parameter for CV. The latter parameter is defined as:

$$\psi = \frac{\left(\frac{D_o}{D_R}\right)^{\alpha/2} k^o}{[D_o \pi \upsilon (nF/RT)]^{1/2}} \qquad (27)$$

Values for ψ for as a function of ΔE_p are given by Nicholson (1965).[141] Here, the diffusion coefficients are taken to be equal and estimated as 10^{-13} cm^2/s. The transfer coefficient, α, is approximated as 0.5 (ignoring the ACV measurements). The heterogeneous rate constant is shown in Table 16 below for peaks I and II. Each peak value represents an average of several k^o calculated for different values of υ. Values for k^o calculated for films on ITO substrates (as opposed to Al foil) gave similar results. These are also included in Table 2. Note that the microstructures on the Al and ITO substrates are slightly different, due to differences between the sputtering conditions used for the separate experiments. These add to variations in the rate constants obtained for the two sets of films.

Table 16: Heterogeneous rate constant derived from SSCV curves.

	$10^7 * k^o$ (cm/s)
Peak I (Al)	*1.43*
Peak II (Al)	*0.14*
Peak I (ITO)	*0.90*
Peak II (ITO)	*1.03*

In general, the values for peak I and II vary between 10^{-7} and 10^{-8} cm/s. The differences between Peak I and Peak II are large and may be more a reflection of the inaccuracy of DC methods than large differences in k^o. However, one might expect the rate constant to vary with potential due to the differences in lithiation state and phases of the $Li_xV_2O_5$. Generally however, even the uncompensated resistance is known to strongly effect the ΔE-υ behavior of systems, such that the CV approach gives only general values of k^o.[92] These value for Peak I are

approximately an order of magnitude lower than the value obtained from AC voltammetry. The latter is generally presumed to be more accurate in quantitative determination.

A dimensionless number is useful to evaluate the degree of either diffusion or reaction limitation in the cathode. The Damköhler (or Biot) number describing mass transfer can be used to evaluate the relative importance of reaction and mass transport determining the electrode kinetics:[142]

$$Bi_{(MT)} = \frac{k}{(\widetilde{D}_{Li}/L)}$$

where k is the heterogeneous rate constant, $\widetilde{D}_{Li}$ the chemical diffusion coefficient, and L the diffusion length (taken here as the thickness of the cathode). The value of k refers to $k_f = k^o e^{-\alpha nf(E-E^{o'})}$ as opposed to k^o, and will be a function of electrode potential.

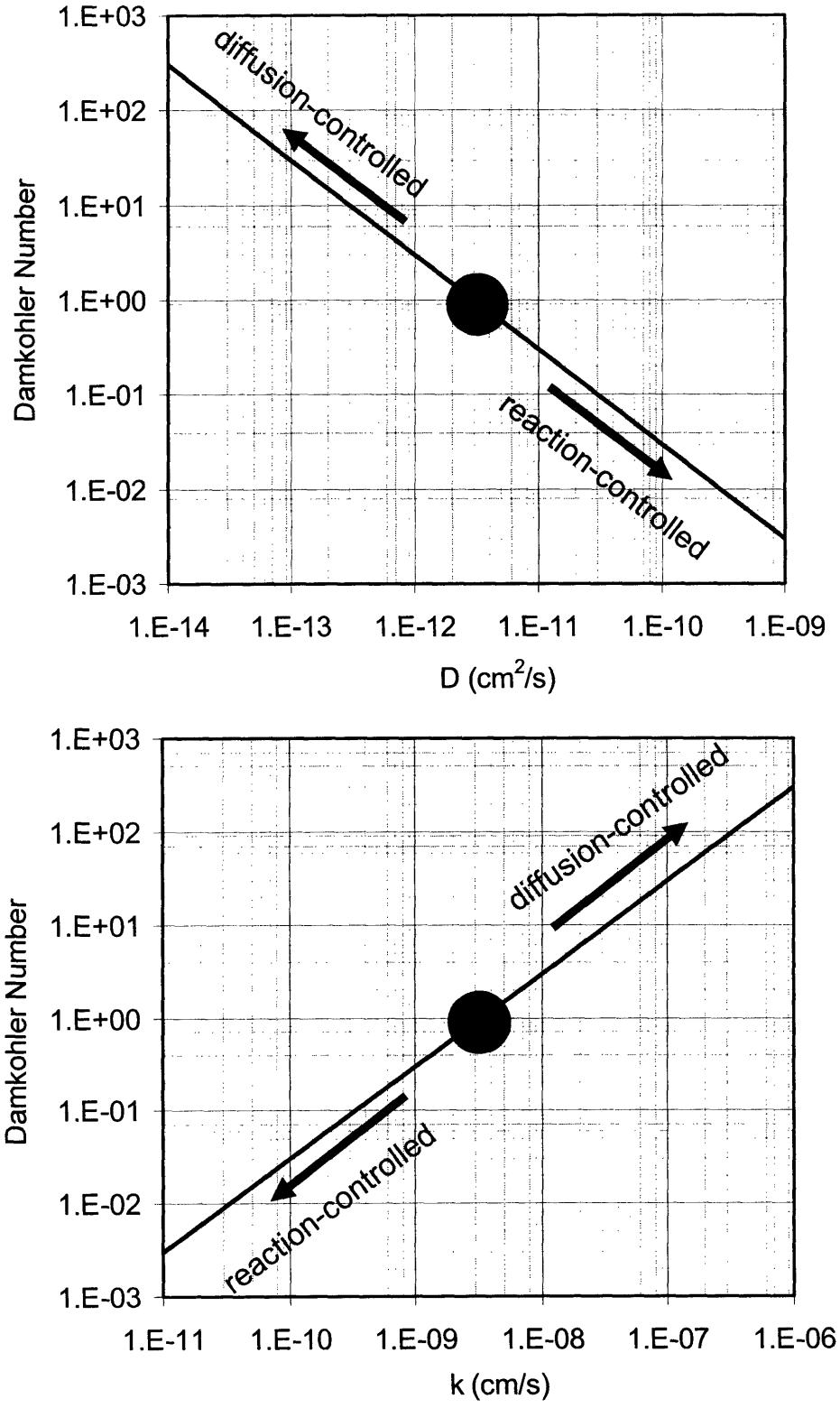

Figure 79: Plots of the Damköhler number as a function of (top) reaction rate constant [$D = 10^{-13}$ cm^2/s, L = 300 nm] and (bottom) chemical diffusion coefficient [$k = 10^{-7}$ cm/s, L = 300 nm].

The above figures show that reaction-limitations will dominate for k below 3 x 10^{-8} cm/s or for D_{Li+} greater than 3 x 10^{-13} cm^2/s. These limiting values overlap with the experimentally derived values for $\widetilde{D}_{Li}$ and k^o, suggesting that the V_2O_5 cathodes are close to operating in a mixed control regime. The thickness studies discussed in chapter 7 showed that within the current range tested, there is indeed a transition from one rate limiting process to another.

Summary

The work represented here is the first reported application of AC voltammetry to evaluate kinetic parameters in lithium battery materials. The heterogeneous rate constants and transfer coefficients can be calculated using both AC voltammetry and cyclic voltammetry. It was found that CV suffers from larger inaccuracies while ACV suffers from added complexity in the analysis due to complications related to the electrode (i.e. low electronic conductivity and solid state diffusion). Attempts to remove these complexities through evaluating higher harmonics and through the use of ultra thin cathodes were largely unsuccessful. However, analysis of the cross-over potential E_{co} yielded some useful information allowing the transfer coefficient to be evaluated. Using the relationship between the phase angle and the frequency for a limited range allowed the standard rate constant to also be evaluated. Both AC and DC approaches gave values within an order of magnitude of each other, with k^o values approaching 10^{-7} to 10^{-6} cm/s.

An exchange current density can be calculated based on the standard rate constant using the equation:

$$j_o = nFk^o C_o^{*(1-\alpha)} C_R^{*\alpha} \qquad (28)$$

where C_o^* and C_R^* represent the bulk concentration of the oxidized and reduced form of the species, respectively.[92] For simplicity, one can assume a 1M solution of lithium salt, equal concentrations of oxidant and reductant, and an activity coefficient of one half. Use of the conservative value for $k^o \sim 10^{-7}$ cm/s, the exchange current density would then be:

$$j_o = nFk^o C = 9.7\ \mu A/cm^2 \qquad (29)$$

Thus, the "idle speed" describing the transfer of charge across the interface is roughly $10\ \mu A/cm^2$, meaning that for rates above this value, a significant overpotential is required (i.e. activation overpotantial) to drive the reaction. The charge transfer resistance associated with this exchange current is ~ 2000 Ω, which suggests a significant overpotential at moderate rates (i.e. ~ 0.2V *IR* drop at a 0.1 mA/cm^2 current).

Despite these findings, the question remains whether the activation overpotential is the dominant characteristic at the highest rates (> 1 mA/cm^2). It was shown in the thickness studies

(chapter 6), that large improvements were made in the Ragone plot by reducing the cathode thickness. Since the activation overpotential related to the charge-transfer process is independent of thickness, the previous results would not hold if the rate constant were controlling. This result suggests that the higher standard rate constant obtained via ACV (10^{-6} cm/s) may be more accurate. In this latter case, a 1 mA/cm^2 current would be needed to begin seeing significant overpotential (0.2 V), and a *100 $\mu A/cm^2$* exchange current would hold.

Chapter 8: Contributions of Dissertation

General Conclusions

This body of work has identified several important factors that affect the electrochemical performance of vanadium pentoxide thin film cathodes. The approaches set forth herein can be expanded to include other material systems.

First, it was demonstrated that different microstructures can be accessed using sputtering techniques. The most important parameters that led to better quality films for use in electrochemical systems included (1) the use of RF sputtering versus DC sputtering, (2) room temperature sputtering versus heated sputtering, and (3) and slow over fast heating rates used for annealing. While other microstructures were obtainable including columnar growth and dendritic-like single crystallites, the best performance was obtained through smooth, nearly dense films. Variations in heating rates led to differences in microstructures, with smaller grain sizes obtained at a fast heating rate and larger grain size obtained at slower heating rates.

It was shown that microstructure can affect the capacity-rate behavior in nearly dense thin films, but not in typically thought of ways. Interestingly, the grain size was not observed to result in different performances for the ITO substrate films. No significant differences were observed in terms of preferred orientation, stress, or thickness in these films – only microstructure and morphology of the crystallites composing the films. It is suggested that grain boundary diffusion, which should be faster than bulk diffusion, did not result in improved performance for films with greater grain boundary volume. This was mainly because other limitations, such as electronic conductivity and reaction kinetics caused significant polarization at the highest current rates. The capacity rate performance largely overlapped due to these latter mechanisms becoming dominant. The results suggest that work focused on improving diffusion may lead to limited improvements due to the presence of other bottlenecks which need to be addressed first. The work also suggests that using grain boundary diffusion may also come at the expense of the film's electrical properties, as amorphous films were measured to be roughly an order of magnitude lower in electronic conduction. This led to lowered rate performance for amorphous films.

By comparison, films on Al substrates, with largely differing grain size distributions, also differed in the degree of preferred orientation. Films that were more aligned in the fast diffusion

direction resulted in improved performance. Unexpectedly, the diffusion coefficients were measured to be similar. However, the phase transformation process was observed to occur more rapidly for the well-oriented film versus the more randomly oriented film. In addition, the interfacial resistance was observed to be higher for the latter, suggesting that improved orientation can improve both the reaction/interfacial kinetics and solid state diffusion. GITT measurements were used to evaluate both the mass transfer kinetics. An additional parameter, $dE_o/d\sqrt{t}$, was proposed to be evaluated with GITT measurements in order to compare the kinetics of the single phase regime with the two phase regime. Using this parameter, it was found that the fine grained, less oriented structures performed more poorly during the phase transformation process compared to the coarse grained, more oriented film. Electrochemical measurements, coupled with TEM and SIMS measurements, also suggest that the phase boundary motion may not proceed as a uniform, planar front but may occur more randomly and inhomogeneously through the film.

Work evaluating the capacity-rate performance for different thickness films showed that capacity-rate performance is improved for thinner V_2O_5 films, as expected. A relation was developed showing that above ~ 500 nm, no advantage is gained in terms of obtained energy by moving to thicker films. This result is largely due to the inability to access the active material completely at moderate to high current rates.

Last, the first reported attempt to use AC cyclic voltammetry for evaluating cathode materials showed additional complexity not reported by ACV theory. It is proposed that the additional complications posed by intercalation compounds, namely solid diffusion, results in additional difficulty resolving the voltammagrams. The expected transition from low to moderate frequencies was observed, allowing for access to the charge-transfer kinetics of the system. However, high frequencies resulted in unusual and as yet unexplained behavior expressed through the voltammagrams. Analysis of second order harmonic currents and of ultra thin cathodes did not resolve these difficulties. Initial but limited results, however, seem to suggest that ACV may be able to provide some quantitative information on kinetic parameters. Slow cyclic voltammetry (DC) was used as an alternative method to evaluate k^o and i_o. Values were obtained for the transfer coefficient, k^o, and i_o.

Suggested Directions

Future work on thin film cathodes should focus on two areas: improving electronic conduction in V_2O_5 and a better understanding of the phase transformation process. The former can involve doping with electronically conducting elements to improve the capacity-rate performance. The calculations performed in chapter 7 show that with $\sigma_e \sim 10^{-6}$ S/cm, the polarization occurring at currents > 1 mA/cm^2 will be severe and cause the obtainable capacity to plummet. Methods of doping are relatively straightforward, and may have the added advantage of allowing for further experimental testing of grain boundary diffusion by reducing competing effects from low electronic conductivity.

Grain size engineering may have limited effects in polycrystalline films simply because the advantages found in reducing particle size for composite samples (i.e. diffusion length ~ $R_{particle}$) are not found in thin films (i.e. diffusion length ~ L_{film}). It is proposed that polycrystalline thin films may be an ideal system with which to understand the phase transformation mechanisms involved with lithiation. It is further proposed that TEM analysis may allow for direct or indirect identification of phase boundaries during different stages of lithiation. This experimental work could add to mathematical models that are only beginning to include the phase transformation process (see for instance, Srinivasan and Newman, 2004).[85] Finally, if large grained samples (> 1 μm) are prepared via sintering of powders, 3-D mapping of the lithium concentration may be possible using SIMS. This work can provide insight into the phase transformation and diffusion process that have not been observed thus far.

Appendix:

AC Voltammetry Setup

The Zplot software was set to DC sweep, constant AC potential mode. Generally, AC perturbations less than 50 mV are necessary in order to ensure that linear response assumptions are valid. Zplot under the normal source settings records only the impedance components of the data as opposed to the complex current. This can be altered by changing the "Source" settings in the instrument setup menu. If V2/V1 is used as the source of the potential/current reading, the impedance will be recorded. Alternatively, if V1 is used as the source, only the AC current signal is measured and recorded. Note that Zview will still label the data axes as impedance despite the data reflecting the complex current.

The DC sweep must be slow enough that the time constants between the diffusion and charge-transfer processes are kept at bay from each other. A number of DC sweep rates were used, ranging from 1 mV/s to as low as 0.025 mV/s. Note that a stepped potential method must be used because the potentiostat is not able to maintain a linear sweep at the lowest sweep rates. Perhaps the most important yet difficult setup is the integration time for the AC signal. Normally, the integration time for the AC signal can be set so that the signal is recorded until the error is less than a specific value (e.g. 10% or 1%). Alternatively, the integration time can be stopped once a number of cycles are recorded (e.g. 1000 cycles) or a specific time has elapsed (e.g. 120 seconds). If medium ranges of frequencies are used (e.g. 0.1 – 100 Hz), the number of cycles that elapse may not be fast enough to keep up with the DC sweep. Ideally, one would desire that the instrument integrates enough AC cycles at a specific DC potential before sweeping further. If either the DC sweep is too fast or the AC frequency too low, this condition may not hold. The results in this case would not be comparable within a sweep through a potential window. Thus for a 10 Hz AC signal, a 1 mV/s DC sweep rate would only result in 10 cycles/mV being recorded, which may be too few to obtain an acceptable error. Added to this concern, the rate of data acquisition should be set no faster than the time needed to integrate enough data for an accurate reading. Thus, in the example above, if the data acquisition is set to 2 data points/mV, the results would have a large error given the sweep rate *and* the frequency values.

Earlier Thickness Study

An earlier thickness study focused on films prepared via DC reactive sputtering on Al foil. The resulting microstructure, as discussed in Chapter 4, consisted of platelets. Testing was performed using a Maccor electrochemical test system. A plot of the capacity-rate performance is shown below in the log-log format used throughout the thesis. Unfortunately, earlier studies did not test the full range to view the steep drop-off for the thinner films. Nor was the Maccor test system capable of going to very low current rates (< 10 $\mu A/cm^2$). Regardless of these differences, the data shows very poor rate performance for these films, with the capacity having a steep drop off for all films before 100 $\mu A/cm^2$ is reached.

Except for the thickest film (1005 nm), the other films show convergence over the current rates which was not observed for the V_2O_5/ITO, RF sputtered films discussed in Chapter 7. This suggests that diffusion was not the limiting factor in these systems. This is because the platelet creates large porosity in the film, so that the liquid electrolyte is able to permeate to near the back of the film. Thus, other limitations, such as electronic and interfacial kinetics, are the dominant. These films were not studied further though, as the quality of DC sputtered films was significantly lower than the RF sputtered films (see Chapter 4). The microstructure was found to

be fragile and susceptible to decrepitation and breaking-off because of the platelet structure.

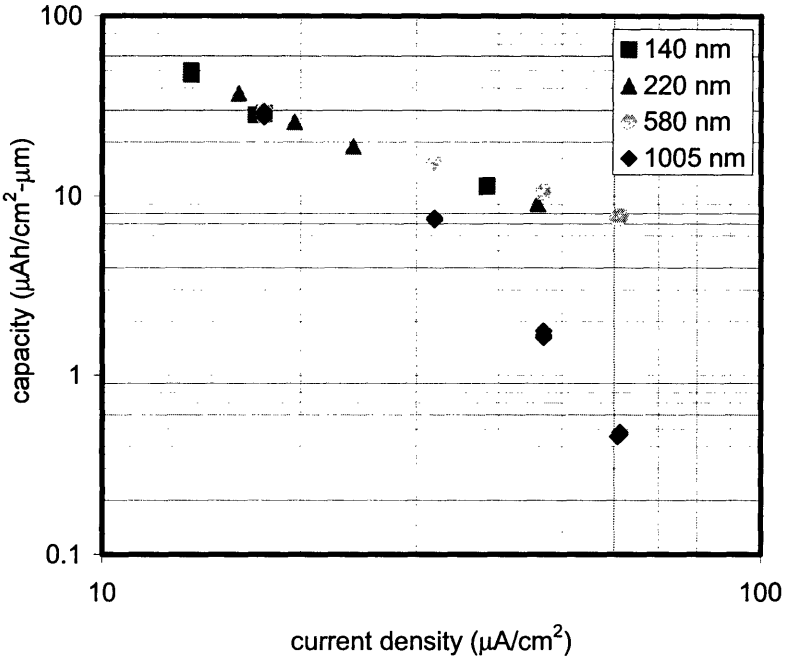

Figure 80: Capacity-rate test for different film thicknesses. Platelet structure.

Surface Area Calculations

An assessment of the effective surface area of a thin film, powder, and fiber structure was performed using a simple spreadsheet model. The parameters input and resulting metrics were obtained and are shown below.

	COMPOSITE		
INPUTS	Gravimetric Current Density		mA/g
	Theoretical capacity		mAh/g
	Cathode Density		g/cc
	Carbon Density		g/cc
	Polymer Density		g/cc
	Cathode mass		mg
	Packing density		
	Active % (mass)		
	Carbon % (mass)		
	Geometric area		cm2
	Average Particle Diam		um
OUTPUTS	Current Used	2.00E+01	mA
	Volume of single powder	6.54E-17	cm3
	Active mass	4.25E-02	g
	Thickness of electrode	1.13E+02	um
	Number of powders	1.94E+14	
	Surface area of active	1.53E+04	cm2
	Effective Surface area	3.59E+05	cm2/g
METRICS	Geometric Current Density		mA/cm2
	Crate		
	Effective Current Density		mA/cm2
	Gravimetric Current Density		mA/g

	THIN FILM		
INPUTS	Geometric area		cm2
	Thickness		nm
OUTPUTS	Film Mass	1.80E-05	g
METRICS	Geometric Current Density		mA/cm2
	Crate		
	Effective Current Density		mA/cm2
	Gravimetric Current Density		mA/g

	Fibers		
INPUTS	Gravimetric Current Density	7.61E+05	mA/g
	Theoretical Capacity	147	mAh/g
	Density of active mass	3.34	g/cm3
	Geometric area	1	cm2
	Avg fiber spacing	0.5	*um*
	Avg fiber length	5	*um*
	Avg fiber diameter	0.25	um
OUTPUTS	Current Used	2.50E+02	mA
	Volume of fibers	9.82E-05	cm3
	Est. Mass of Fibers	3.28E-04	ug
	Est. Mass loading	3.28E-04	g/cm2
	Number of fibers	4.00E+08	
	Surface area of active	1.59E+01	cm2
	Effective Surface area	4.85E+04	cm2/g
METRICS	Geometric Current Density		mA/cm2
	Crate		
	Effective Current Density		mA/cm2
	Gravimetric Current Density		mA/g

References

[1] J. P. Thomas and M. A. Qidwai, *JOM-J. Miner. Met. Mater. Soc.*, **57**, 18 (2005).

[2] S. H. Lee, P. Liu, C. E. Tracy, and D. K. Benson, *Electrochemical and Solid-State Letters*, **2**, 425 (1999).

[3] D. Singh, R. Houriet, R. Giovannini, H. Hofmann, V. Cracium, and R. K. Signh, *Journal of Power Sources*, **97-98**, 826 (2001).

[4] K. Kanehori, K. Matsumoto, K. Miyauchi, and T. Kudo, *Solid State Ionics*, **9-10**, 1445 (1983).

[5] A. K. Shukla, N. R. Avery, and B. C. Muddle, *Current Science*, **77**, 1141 (1999).

[6] K. Brandt, *Solid State Ionics*, **69**, 173 (1994).

[7] G. B. Appetecchi, F. Croce, G. Dautzenberg, S. Panero, and B. Scrosati; J. B. Bates, vi+231, *Proceedings of the Symposium on Thin Film Solid Ionic Devices and Materials*, Chicago, IL, USA., (1996)

[8] J. B. Bates, N. J. Dudney, B. Neudecker, A. Ueda, and C. D. Evans, *Solid State Ionics, Diffus., React.*, **135**, 33 (2000).

[9] C. Julien, M. A. Camacho Lopez, L. Escobar Alarcon, and E. Haro Poniatowski, *Mater. Chem. Phys.*, **68**, 210 (2001).

[10] M. Z. A. Munshi and B. B. Owens, *Solid State Ionics, Diffus., React.*, **38**, 103 (1990).

[11] G. G. Botte, V. R. Subramanian, and R. E. White, *Electrochim. Acta*, **45**, 2595 (2000).

[12] J. B. Goodenough, *Solid State Ionics*, **69**, 184 (1994).

[13] M. V. Mirkin, F. R. F. Fan, and A. J. Bard, *Science*, **257**, 364 (1992).

[14] J. Bates, G. Gruzalski, N. Dudney, C. Luck, and X. Yu, *Solid State Ionics*, **70-71**, 619 (1994).

[15] N. J. Dudney and Y. I. Jang, *J. Power Sources*, **119-121**, 300 (2003).

[16] E. Antolini, *Solid State Ionics*, **170**, 159 (2004).

[17] M. Deepa, A. K. Srivastava, S. Singh, and S. A. Agnihotry, *J. Mater. Res.*, **19**, 2576 (2004).

[18] H. Miyazaki, H. Sakamura, M. Kamei, and I. Yasui, *Solid State Ionics*, **122**, 223 (1999).

[19] J. B. Bates, N. J. Dudney, B. J. Neudecker, F. X. Hart, H. P. Jun, and S. A. Hackney, *J. Electrochem. Soc.*, **147**, 59 (2000).

[20] P. J. Bouwman, B. A. Boukamp, H. J. M. Bouwmeester, and P. H. L. Notten, *Solid State Ionics*, **152**, 181 (2002).

[21] J. A. Thornton, *J. Vac. Sci. Technol., A*, **4**, 3059 (1986).

[22] C. R. Aita, *J. Vac. Sci. Technol., A*, **11**, 1540 (1993).

[23] B. A. Movchan and A. V. Demchishin, *Phys. Met. Metallogr.*, **28**, 83 (1969).

[24] P. J. Bouwman, B. A. Boukamp, H. J. M. Bouwmeester, and P. H. L. Notten, *J. Electrochem. Soc.*, **149**, A699 (2002).

[25] M. E. Garcia and S. H. Garofalini, *J. Electrochem. Soc.*, **146**, 840 (1999).

[26] W. Q. Li and S. H. Garofalini, *J. Electrochem. Soc.*, **152**, A364 (2005).

[27] S. H. Garofalini, *J. Power Sources*, **110**, 412 (2002).

[28] J. M. Cocciantelli, M. Menetrier, C. Delmas, J. P. Doumerc, M. Pouchard, M. Broussely, and J. Labat, *Solid State Ionics*, **78**, 143 (1995).

[29] J. F. Whitacre, W. C. West, E. Brandon, and B. V. Ratnakumar, *J. Electrochem. Soc.*, **148**, A1078 (2001).

[30] P. Heitjans and S. Indris, *J Phys-Condens Mat*, **15**, R1257 (2003).

[31] J. M. Cocciantelli, M. Menetrier, C. Delmas, J. P. Doumerc, M. Pouchard, M. Broussely, and J. Labat, *Solid State Ionics*, **78**, 143 (1995).

[32] P. Heitjans and S. Indris, *J. of Mater. Sci.* , **39**, 5091 (2004).

[33] M. Ulrich, A. Bunde, S. Indris, and P. Heitjans, *Phys. Chem. Chem. Phys.*, **6**, 3680 (2004).

[34] K. F. Hsu, S. Y. Tsay, and B. J. Hwang, *J. Mater. Chem.*, **14**, 2690 (2004).

[35] M. Nakayama, K. Watanabe, H. Ikuta, Y. Uchimoto, and M. Wakihara, *Solid State Ionics*, **164**, 35 (2003).

[36] J. S. Sakamoto, C. K. Huang, S. Surampudi, M. Smart, and J. Wolfenstine, *Mater. Lett.*, **33**, 327 (1998).

[37] M. Kalbac, M. Zukalova, and L. Kavan, *J. Solid State Electrochem.*, **8**, 2 (2003).

[38] M. Fakumua, *Appl. Opt.*, **22**, 265 (1963).

[39] O. B. Ajayi, *Thin Solid Films*, **82**, 151 (1981).

[40] S. D. Hansen and C. R. Aita, *J. Vac. Sci. Technol., A*, **3**, 660 (1985).

[41] D. H. Hensler, A. R. Ross, and E. N. Fuls, *J. Electrochem. Soc.*, **116**, 887 (1969).

[42] R. J. Colton, A. M. Guzman, and J. W. Rabalais, *J. Appl. Phys.*, **49**, 409 (1978).

[43] M. K. A. Levasseur, P. Hagenmuller, G. Couturier, Y. Danto, *Solid State Ionics*, **9-10**, 1445 (1983).

[44] R. Creus, J. Sarradin, R. Astier, A. Pradel, and M. Ribes, *Mater. Sci. Eng.*, **B3**, 19 (1989).

[45] A. Levasseur, M. Kbala, P. Hagenmuller, G. Couturier, and Y. Danto, *Solid State Ionics*, **9-10**, 1445 (1983).

[46] S. Jones and J. Akridge, *Solid State Ionics*, **53-56**, 6238 (1992).

[47] J. B. Bates, N. J. Dudney, D. C. Lubben, G. R. Gruzalski, B. S. Kwak, X. H. Yu, and R. A. Zuhr, *J. Power Sources*, **54**, 58 (1995).

[48] N. J. Dudney, J.B. Bates, R. Zuhr, and C. Luck, *Solid State Ionics*, **53-56**, 655 (1992).

[49] S. Jones and J. Akridge, *J. Power Sources*, **43-44**, 505 (1993).

[50] S. Jones and J. Akridge, *J. Power Sources*, **54**, 63 (1995).

[51] N. J. Dudney and Y. I. Jang, *J. Power Sources*, **119**, 300 (2003).

[52] B. J. Neudecker, N. J. Dudney, and J. B. Bates, *J. Electrochem. Soc.*, **147**, 517 (2000).

[53] Y. I. Jang, B. J. Neudecker, and N. J. Dudney, *Electrochem. Solid-State Lett.*, **4**, A74 (2001).

[54] Y. I. Jang, N. J. Dudney, D. A. Blom, and L. F. Allard, *J. Electrochem. Soc.*, **149**, A1442 (2002).

[55] Y. I. Jang, N. J. Dudney, D. A. Blom, and L. F. Allard, *J. Power Sources*, **119**, 295 (2003).

[56] A. Pique, K. E. Swider Lyons, D. W. Weir, C. T. Love, and R. Modi, *Proceedings of the SPIE The International Society for Optical Engineering*, **4274**, 316 (2001).

[57] P. Baudry, M. Aegerter, D. Deroo, and B. Valla, *J. Electrochem. Soc.*, **138**, 460 (1991).

[58] J-S. Bae and S.-I. Pyun, *Solid State Ionics*, **90**, 251 (1996).

[59] C. Julien, A. Gorenstein, A. Khelfa, J. Guesdon, and I. Ivanov, *Mater. Res. Soc. Symp. Proc.*, **369**, 639 (1995).

[60] J. M. Mcgraw, C. S. Bahn, P. A. Parilla, J. D. Perkins, D. W. Readey, and D. S. Ginley, *Electrochim. Acta*, **45**, 187 (1999).

[61] T. Oshio, Y. Sakai, T. Moriya, and S. Ehara, *Ultra-microscopy*, **42-44**, 744 (1992).

[62] R. L. Smith, W. Lu, and G. S. Rohrer, *Surface Science*, **322**, 293 (1995).

[63] R. L. Smith, G. S. Rohrer, K. S. Lee, D.-K. Seo, and M.-H. Whangbo, *Surface Science*, **367**, 87 (1996).

[64] J. W. Bullard and R. L. Smith; 756, EE7.10, *MRS Proceedings*, (2002)

[65] B. J. Neudecker, R.A. Zuhr, and J. B. Bates, *J. Power Sources*, **81-82**, 27 (1999).

[66] K. Ozawa, *Solid State Ionics*, **69**, 212 (1994).

[67] R. W. Cahn and P. Haasen, *Physical Metallurgy*, North-Holland, (1983).

[68] C. D. Adams, D. J. Srolovitz, and M. Atzmon, *J. Appl. Phys.*, **74**, 1707 (1993).

[69] O. Meakin, P. Ramanlal, L. M. Sander, and R. C. Ball, *Phys. Rev. A*, **34**, 5091 (1986).

[70] K.-H. Milller, *J. Appl. Phys.*, **58**, 2573 (1985).

[71] S. Ling and M. P. Anderson, *J. Electron. Mater.*, **17**, 459 (1988).

[72] D. J. Srolovitz, *J. Vac. Sci. Technol., A*, **4**, 2925 (1986).

[73] D. J. Srolovitz, A. Mazor, and B. G. Bukiet, *J. Vac. Sci. Technol., A*, **6**, 2371 (1988).

[74] F. Ying, R. W. Smith, and D. J. Srolovitz, *Appl. Phys. Lett.*, **69**, 3007 (1996).

[75] J. A. Thornton, *J. Vac. Sci. Technol.*, **11**, 666 (1974).

[76] I. J. Ong and J. Newman, *J. Electrochem. Soc.*, **146**, 4360 (1999).

[77] F. Lantelme, H. Groult, and N. Kumagai, *Electrochim. Acta*, **45**, 3171 (2000).

[78] M. W. Verbrugge, B. J. Koch, and E. W. Schneider, *J. Appl. Electrochem.*, **30**, (2000).

[79] M. Doyle and J. Newman, *J. Appl. Electrochem.*, **27**, 846 (1997).

[80] S. Rodrigues, N. Munichandraiah, and A. K. Shukla, *J. Appl. Electrochem.*, **30**, 571 (2000).

[81] J. Farcy, R. Messina, and J. Perichon, *J. Electrochem. Soc.*, **137**, 133761341. (1990).

[82] W. Weppner and R. A. Huggins, *J. Electrochem. Soc.*, **124**, 1569 (1977).

[83] F. Lantelme, A. Mantoux, H. Groult, and D. Lincot, *J. Electrochem. Soc.*, **150**, A1202 (2003).

[84] B. C. Han, A. Van Der Ven, D. Morgan, and G. Ceder, *Electrochim. Acta*, **49**, 4691 (2004).

[85] V. Srinivasan and J. Newman, *J. Electrochem. Soc.*, **151**, A1517 (2004).

[86] Y. Mishin, C. Herzig, J. Bernardini, and W. Gust, *International Materials Reviews*, **42**, 155 (1997).

[87] Y. Mishin, *Defect Diffus Forum*, **143**, 1357 (1997).

[88] J. C. Fisher, *J Applied Physics*, **22**, 74 (1951).

[89] L. G. Harrison, *Trans. Faraday Soc.*, **57**, 1191 (1961).

[90] I. Kaur and W. Gust, *Fundamentals of Grain and Interphase Boundary Diffusion*, Ziegler Press, (1989).

[91] J. O. Besenhard, 636, (1999)

[92] A. J. Bard and L. R. Faulkner, *Electrochemical Methods: Fundamentals and Applications*, John Wiley & Sons, Inc., (1980).

[93] M. D. Levi and D. Aurbach, *J. Electroanal. Chem.*, **421**, 79 (1997).

[94] L. S. Darken, *Trans. Am. Inst. Min. Engrs.*, **175**, 184 (1948).

[95] L. S. Darken, *Trans. Am. Inst. Min. Engrs.*, **180**, 430 (1949).

[96] A. M. Bond, R. J. O'halloran, I. Ruzic, and D. E. Smith, *Anal. Chem.*, **48**, 872 (1976).

[97] W. L. Underkofler and I. Shain, *Anal. Chem.*, **37**, 218 (1965).

[98] C. Satto, P. Sciau, E. Dooryhee, J. Galy, and P. Millet, *Journal of Solid State Chemistry*, **146**, 103 (1999).

[99] V. Eyert and K. H. Hock, *Phys. Rev. B*, **57**, 12727 (1998).

[100] A. Dietrich, C. R. A. Catlow, and B. Maigret, *Molecular Simulation*, **11**, 251 (1993).

[101] J. Galy, *Journal of Solid State Chemistry*, **100**, 229 (1992).

[102] P. Strobel, F. Lecras, and M. Anne, *Journal of Solid State Chemistry*, **124**, 83 (1996).

[103] S. Crouchbaker, C. K. Huang, and R. A. Huggins, *J. Electrochem. Soc.*, **134**, C403 (1987).

[104] J. S. Braithwaite, C. R. A. Catlow, J. D. Gale, and J. H. Harding, *Chem. Mat.*, **11**, 1990 (1999).

[105] C. Delmas, H. Cognacauradou, J. M. Cocciantelli, M. Menetrier, and J. P. Doumerc, *Solid State Ionics*, **69**, 257 (1994).

[106] P. Rozier, J. M. Savariault, J. Galy, C. Marichal, J. Hirschinger, and P. Granger, *European Journal of Solid State and Inorganic Chemistry*, **33**, 1 (1996).

[107] P. Hagenmuller, J. Galy, M. Pouchard, and A. Casalot, *Materials Research Bulletin*, **1**, 45 (1966).

[108] S. Passerini, D. B. Le, W. H. Smyrl, M. Berrettoni, R. Tossici, R. Marassi, and M. Giorgetti, *Solid State Ionics*, **104**, 195 (1997).

[109] E. Cazzanelli, G. Mariotto, S. Passerini, W. H. Smyrl, and A. Gorenstein, *Sol. Energy Mater. Sol. Cells*, **56**, 249 (1999).

[110] R. A. Huggins and W. D. Nix, *Ionics*, **6**, 57 (2000).

[111] D. W. Murphy, P. A. Christian, F. J. Disalvo, and J. V. Waszczak, *Inorg Chem*, **18**, 2800 (1979).

[112] P. Arora, M. Doyle, A. S. Gozdz, R. E. White, and J. Newman, *J. Power Sources*, **88**, 219 (2000).

[113] S. E. Offerman, N. H. Van Dijk, J. Sietsma, E. M. Lauridsen, L. Margulies, S. Grigull, H. F. Poulsen, and S. Van Der Zwaag, *Acta Mater.*, **52**, 4757 (2004).

[114] J. W. Christian, *The theory of transformations in metals and alloys*, Pergamon Press, (1981).

[115] *Powder Diffaction Standards File No. 41-1426.*,

[116] W. Weppner and R. A. Huggins, *Annu. Rev. Mater. Sci.*, **8**, 269 (1978).

[117] H. Wang, Y.-I. Jang, B. Huang, D. R. Sadoway, and Y.-M. Chiang, *J. Power Sources*, **81-82**, 594 (1999).

[118] A. Atkinson, *Surfaces and Interfaces of Ceramic Materials*, 273 (1989).

[119] Y. Iriyama, T. Abe, M. Inaba, and Z. Ogumi, *Solid State Ionics*, **135**, 95 (2000).

[120] J. M. Cocciantelli, J. P. Doumerc, M. Pouchard, M. Broussely, and J. Labat, *J. Power Sources*, **34**, 103 (1991).

[121] A. Benninghoven, F. G. Rüdenauer, and H. W. Werner, *Secondary Ion Mass Spectroscopy: Basic Concepts, Instrumental Aspects, Applications, and Trends*, Wiley, (1987).

[122] M. Shaanan and R. Kalish, *Nuclear Instruments & Methods in Physics Research Section B-Beam Interactions with Materials and Atoms*, **171**, 332 (2000).

[123] P. N. K. Deenapanray and M. Petravic, *J. Appl. Phys.*, **87**, 2178 (2000).

[124] H. Kim and C. M. Gilmore, *J. Appl. Phys.*, **86**, 6451 (1999).

[125] C. J. Patrissi and C. R. Martin, *J. Electrochem. Soc.*, **148**, A1247 (2001).

[126] Y. J. Park, K. S. Ryu, N.-G. Park, Y.-S. Hong, and S. H. Chang, *J. Electrochem. Soc.*, **149**, A597 (2002).

[127] S. Suzuki, M. Hibino, and M. Miyayama, *J. Power Sources*, **124**, 513 (2003).

[128] B. B. Lakshmi, C. J. Patrissi, and C. R. Martin, *Chem. Mat.*, **9**, 2544 (1997).

[129] C. J. Patrissi and C. R. Martin, *J. Electrochem. Soc.*, **146**, 3176 (1999).

[130] C. R. Sides, N. C. Li, C. J. Patrissi, B. Scrosati, and C. R. Martin, *MRS Bull.*, **27**, 604 (2002).

[131] C. J. Patrissi and C. R. Martin, *J. Electrochem. Soc.*, **148**, A1247 (2001).

[132] J. Maier, *Zeitschrift Fur Physikalische Chemie-International Journal of Research in Physical Chemistry & Chemical Physics*, **217**, 415 (2003).

[133] J. Jamnik and J. Maier, *Phys. Chem. Chem. Phys.*, **5**, 5215 (2003).

[134] J. Maier, *Solid State Ionics*, **154**, 291 (2002).

[135] E. Deiss, D. Haringer, P. Novak, and O. Haas, *Electrochim. Acta*, **46**, 4185 (2001).

[136] P. Krtil and D. Fattakhova, *J. Electrochem. Soc.*, **148**, A1045 (2001).

[137] H. Lindstrom, S. Sodergren, A. Solbrand, H. Rensmo, J. Hjelm, A. Hagfeldt, and S. E. Lindquist, *Journal of Physical Chemistry B*, **101**, 7717 (1997).

[138] M. Mohamedi, D. Takahashi, T. Itoh, M. Umeda, and I. Uchida, *J. Electrochem. Soc.*, **149**, A19 (2002).

[139] M. D. Levi, Z. Lu, and D. Aurbach, *J. Power Sources*, **97-8**, 482 (2001).

[140] S. W. Song, K. A. Striebel, R. P. Reade, G. A. Roberts, and E. J. Cairns, *J. Electrochem. Soc.*, **150**, A121 (2003).

[141] R. S. Nicholson, *Anal. Chem.*, **37**, 1351 (1965).

[142] D. R. Poirier and G. H. Geiger, *Transport phenomena in materials processing*, The Minerals, Metals & Materials Society, (1994).

MIT Libraries
Document Services

Room 14-0551
77 Massachusetts Avenue
Cambridge, MA 02139
Ph: 617.253.5668 Fax: 617.253.1690
Email: docs@mit.edu
http://libraries.mit.edu/docs

DISCLAIMER OF QUALITY

Due to the condition of the original material, there are unavoidable flaws in this reproduction. We have made every effort possible to provide you with the best copy available. If you are dissatisfied with this product and find it unusable, please contact Document Services as soon as possible.

Thank you.

Some pages in the original document contain pictures or graphics that will not scan or reproduce well.